

# **Spectropolarimetric analysis of circumstellar mass flows**

by

**Kenneth Wood**

Thesis  
submitted to the  
University of Glasgow  
for the degree  
of Ph.D.

Department of Physics and Astronomy,  
The University,  
Glasgow G12 8QQ.

©Kenneth Wood  
September 1993.

ProQuest Number: 13834104

All rights reserved

INFORMATION TO ALL USERS

The quality of this reproduction is dependent upon the quality of the copy submitted.

In the unlikely event that the author did not send a complete manuscript and there are missing pages, these will be noted. Also, if material had to be removed, a note will indicate the deletion.



ProQuest 13834104

Published by ProQuest LLC (2019). Copyright of the Dissertation is held by the Author.

All rights reserved.

This work is protected against unauthorized copying under Title 17, United States Code  
Microform Edition © ProQuest LLC.

ProQuest LLC.  
789 East Eisenhower Parkway  
P.O. Box 1346  
Ann Arbor, MI 48106 – 1346

Thesis  
9631  
copy 1

GLASGOW  
UNIVERSITY  
LIBRARY

## Summary

Polarimetry is not a difficult subject. Unfortunately, as it is a second order effect (typical stellar polarisations are of the order of a few percent), in many undergraduate courses on stellar atmospheres and the interstellar medium it is either ignored entirely or mentioned as an aside if there is time at the end of the course. Through this lack of teaching no standard introductory texts on the subject have been adopted and many student's experience of polarimetry is the intense and rather obscure mathematical formulation of the Stokes parameters presented in Chandrasekhar's book on radiative transfer. As a result most theoreticians and observers embark upon research careers with the knowledge that there exist four Stokes parameters, but unaware of their physical significance or diagnostic potential. For these reasons I have devoted the first chapter of this thesis to giving a brief introduction to the subject of polarimetry and its astronomical applications. The parameters required to study polarised radiation – the Stokes parameters – are presented mathematically and their physical interpretations in terms of sums and differences of intensity components of the radiation field are outlined. Following on from a summary of sources of polarised radiation in astronomy the theoretical analysis predicting the “broad-band” polarisation from the optically thin Thomson scattering extended envelopes surrounding hot single stars is presented.

Chapters 2, 3, 4 and 5 extend this theoretical framework to treat the problem of line polarisation through scattering of unpolarised stellar lines in moving atmospheres. Due to the complexity of polarised radiative transfer this problem has not been treated in a systematic fashion before and the few theoretical investigations to date were built around existing radiative transfer codes which did not allow the basic physical processes contributing to the line polarisation to be isolated. While the theory presented in these chapters is much simpler than a full blown radiative transfer approach it clearly demonstrates the role of scattering and Doppler redistribution, due to the scatterer's motion, in the production of spectropolarimetric line profiles. It is further shown that adopting this approach allows determination of the inclination, velocity and density structure of circumstellar discs from analysis of the scattered spectropolarimetric line profiles – information which cannot be determined from spectrometry alone. At the end of Chapter 5 an outline is given as to the future work required to develop a comprehensive theoretical understanding of stellar line polarisation, noting at each stage the effects on the resulting line profiles of the various amendments to the theory.

Temporal variations in the continuum polarisation of Be stars have been observed to occur over a wide range of timescales and have been attributed to variations in the shape or rate of stellar mass loss which changes the number of scattering electrons in the stellar envelope. With this interpretation of the polarimetric variations Chapter 6 illustrates a method for determining these episodic mass loss functions from analysis of polarimetric and absorption line strength data

during the outbursts. The formulation of the equations in this chapter as an inverse problem was the initial problem suggested to me by my supervisor, John Brown, and the background reading I did on circumstellar polarisation while working on this problem led me to investigate the line polarisation variations presented in the previous chapters.

The stellar wind speeds considered in the above chapters were such that any relativistic effects could be ignored. However, Chapter 7 considers the scattering of radiation off relativistic electrons yielding a very simple result for the degree of scattered polarisation involving the aberrational angle. This is part of an on-going investigation into polarisation from scattering in relativistic jets, which I am conducting in collaboration with John Simmons, of which the initial results are presented.

The research presented in the thesis was conducted by myself or in collaboration with other members of the Glasgow Astronomy Group. The mass loss inversion, Chapter 6, and part of Chapter 2 have been published in *Astronomy & Astrophysics* and their references are,

Brown J.C., Wood K., 1992, *Astron. Astrophys.*, **265**, 663

Wood K., Brown J.C., Fox G.K., 1993, *Astron. Astrophys.*, **271**, 492

## Acknowledgements

This thesis was conducted under the supervision of Professor John Brown in the Department of Physics and Astronomy at the University of Glasgow and funded by the United Kingdom Science and Engineering Research Council (SERC).

The work I have conducted would not have been possible without the advice and support of John Brown. His encouragement to contact and visit departments conducting research relevant to my own has been of great benefit and I would like to thank him for all the travel opportunities he gave me.

Throughout my Ph.D. research I have constantly sought the advice of all members of the Astronomy group and I would like to thank them all for their patience, in particular John Simmons who suggested and guided me through the work in Chapter 7 and Geoff Fox, now at the University of Wisconsin, with whom I had many discussions regarding line polarisation.

Over the three years of the Ph.D. I made several research and conference visits to the USA and Canada. These would not have been possible without the encouragement from John Brown and financial support of the SERC and the Physics and Astronomy Department at Glasgow. I also appreciate the warm welcome extended to me by members of the Astronomy Departments in Madison and Montreal during my visits there.

## Contents

<b>Summary</b> .....	i
<b>Acknowledgements</b> .....	iii
<b>Chapter 1 Astronomical polarisation</b> .....	1
1.1 Introduction .....	1
1.2 The Stokes parameters of polarised radiation .....	2
1.3 Production of polarised radiation in astronomy .....	5
1.3.1 Scattering .....	5
1.3.2 Synchrotron radiation .....	7
1.3.4 Interstellar polarisation .....	7
1.4 Polarisation from optically thin circumstellar envelopes .....	9
1.4.1 General formalism .....	10
1.4.2 Unpolarised point source, axisymmetric envelope .....	13
1.4.3 Depolarisation factor for a finite spherical source .....	15
1.4.4 Occultation effects .....	15
1.4.5 Other continuum opacity sources in an optically thin envelope .....	16
1.4.6 How valid is the single scattering theory ? .....	18
1.5 Conclusions .....	20
<b>Chapter 2 Spectropolarimetric line profiles from optically thin discs</b> .....	21
2.1 Introduction .....	21
2.2 Observations .....	21
2.3 Theory .....	25
2.3.1 Polarisation in rotationally broadened spectral lines .....	25
2.3.2 Optical depth effects in a moving circumstellar envelope .....	27
2.3.3 Line scattering in an expanding envelope .....	28
2.4 Effects of electron bulk velocity on scattered line profiles .....	29
2.5 Scattering of monochromatic radiation .....	31
2.5.1 Pure disc rotation .....	32
2.5.2 Pure disc expansion .....	36
2.5.3 Rotation and expansion .....	42
2.6 Non-monochromatic source .....	45
2.6.1 Pure disc rotation .....	46
2.6.2 Pure disc expansion .....	48
2.6.3 Disc expansion and rotation .....	49
2.7 General determination of disc inclination .....	54

<b>Chapter 3</b>	<b>Inversion of Thomson scattered spectropolarimetric line profiles</b>	<b>— 56</b>
3.1	Introduction	56
3.2	Formulation of the integral equation	57
3.3	Determination of disc inclination	59
3.3.1	Rotating disc	59
3.3.2	Expanding disc	60
3.4	Solution of the integral equations	61
3.4.1	Rotating disc	61
3.4.2	Expanding disc	62
3.5	Interpretation of the solutions	62
3.6	Conclusions	63
<b>Chapter 4</b>	<b>Effect of electron thermal motions on scattered line profiles</b>	<b>—— 64</b>
4.1	Introduction	64
4.2	Theory	64
4.3	Continuum polarisation	68
4.4	Monochromatic point source	68
4.5	Gaussian line source	70
4.6	Effect of electron bulk and thermal motions	72
4.6	Scattering of monochromatic radiation	73
4.7.1	Isothermal rotating disc	73
4.7.2	Isothermal expanding disc	75
4.7.3	Rotating and expanding isothermal disc	76
4.8	Determination of disc inclination	76
<b>Chapter 5</b>	<b>Spectropolarimetric line profiles from circumstellar envelopes</b>	<b>—— 78</b>
5.1	Three dimensional axisymmetric circumstellar envelopes	78
5.2	Scattering of stellar line radiation	79
5.2.1	Pure envelope rotation	80
5.2.2	Pure envelope expansion	81
5.2.2	Envelope rotation and expansion	82
5.3	Electron bulk and thermal motions in a three dimensional envelope	82
5.4	Wavelength integrated Stokes fluxes	89
5.5	Future work	89
5.5.1	The general single scattering equation for scattering monochromatic radiation	89
5.5.2	Line opacity and the extension to optically thick circumstellar envelopes	90
5.5.3	Temporal variations of spectropolarimetric line profiles	91
5.5.4	Application to non stellar objects	92
5.5.5	Forthcoming observing campaigns	92

<b>Chapter 6</b>	<b>Derivation of episodic mass loss functions for hot stars</b>	<b>94</b>
6.1	Introduction	94
6.2	Analytic formulation and solution	95
6.2.1	The forward problem	95
6.2.2	Inverse Fourier solution	98
6.3	Numerical results	99
6.3.1	Discretisation procedure	99
6.3.2	Illustrative results	100
6.4	Other analytic solutions	106
6.4.1	Laplace solution	106
6.4.2	Integral moment solution	106
6.5	The effect of noise in the data	107
6.6	An alternative inversion strategy	107
<b>Chapter 7</b>	<b>Polarisation from relativistic electron scattering</b>	<b>109</b>
7.1	Introduction	109
7.2	Four-vector calculus	110
7.2.1	Definition of a four-vector	110
7.2.2	Some properties of four-vectors	110
7.2.3	Polarisation four-vectors	111
7.3	Compton scattering theory	112
7.4	Unpolarised point source illuminating a rectilinear jet	113
7.5	Application to relativistic jets	116
<b>References</b>		<b>118</b>
<b>Appendix</b>		<b>120</b>
A.1	The specific intensity	120
A.2	The flux	120
A.3	Opacity – absorption and scattering coefficients	120
A.4	Optical depth	122
A.5	The emission coefficient	123
A.6	The equation of radiative transfer	123

## 1. Astronomical polarisation

### Summary

In this chapter a brief introduction is given to the study of light and the property known as its polarisation. Much has been written about the dual nature of light (as a wave or particle) and either formulation can be used to describe polarisation. However, for the bulk of this thesis, which ignores relativistic effects, the wave representation is more physically intuitive and is what is outlined below. When relativistic effects become important, for example in the problem of scattering off relativistic electrons, a more convenient mathematical representation for light is in terms of photons and their associated polarisation and momentum 4-vectors. This problem is studied in Chapter 7 and further discussion is left until then.

### 1.1 Introduction

By the eighteenth century the phenomenon of light had been studied by many experimenters resulting in the formulation of the laws of geometric optics which successfully described the observed reflection and refraction of a light beam – Snell’s law. However, when Young investigated the diffraction of light by two narrow slits he discovered that a pattern similar to that produced by the diffraction of water waves was formed which could not be explained by the current theories. This discovery led him to propose that light was composed of orthogonal vibrations (perpendicular to the direction of propagation) of *something*. What this *something* was remained a mystery until the publication of Maxwell’s electromagnetic theory which demonstrated that light was a transverse electromagnetic wave and that visible light makes up only a small part of the entire electromagnetic spectrum. Much of twentieth century astronomy has been devoted to the subjects of spectroscopy, which studies the variations with wavelength of the intensity of electromagnetic radiation, and photometry which determines the magnitude (brightness) of astronomical objects. For these purposes measurements are made of the radiation flux from which the *specific intensity* of radiation may be inferred. The specific intensity is a quantity which describes everything about the radiation (its energy density, wavelength and direction of propagation) *except* its polarisation state.

This proposed wave nature allows a mathematical description of radiation in terms of two orthogonal components of the electric or magnetic fields, each with an amplitude and a phase, which are transverse to the direction of propagation. The term *polarisation* refers to any constant or time dependent variations of the amplitudes or phases. In general then, through time the tip of the resultant electric or magnetic vector, projected onto the plane which is perpendicular to the direction of propagation of the wave, will trace out a polarisation ellipse. To fully describe the

polarisation state of radiation requires a description of this polarisation ellipse involving amplitudes along any two orthogonal axes, the orientation of the maximum amplitude with respect to these axes and a phase difference.

It is evident from the above that a complete description of a radiation field requires independent measurements which will yield four quantities – two amplitudes an orientation angle and a phase difference. A mathematical description which encompasses these four quantities in parameters of the same dimensions is therefore required to facilitate further theoretical and experimental analysis of the radiation field. The most convenient representation was achieved by Sir George Stokes who, in 1852, proposed a set of four parameters of the same dimensions which would completely specify the polarisation state of the radiation. Stokes' analysis, which was completed after Young's experiments, but four years before Maxwell published his electromagnetic theory of radiation, lay largely unused in astronomy for the best part of a century until Chandrasekhar resurrected it for his papers on radiative transfer in the 1940s. Although the terminology of the original paper was altered, Stokes' fundamental analysis remained the same – his four parameters (originally  $A, B, C$  and  $D$ ) were replaced by the now almost universally accepted  $I, Q, U$  and  $V$ . The mathematical and physical descriptions of these four parameters in terms of orthogonal vibrations of the electromagnetic vector are the subject of the next section.

## 1.2 The Stokes' Parameters of polarised radiation

Maxwell's electromagnetic theory allows the mathematical formulation of radiation in terms of two orthogonal components of the electric (or the associated magnetic) vector, thus,

$$\mathbf{E} = \hat{x} E_x \cos(2\pi\nu t - \delta_x - kz) + \hat{y} E_y \cos(2\pi\nu t - \delta_y - kz), \quad (1.1)$$

where, at position  $z$  and time  $t$ , the components of the electric vector,  $\mathbf{E}$ , along directions  $\hat{x}$  and  $\hat{y}$  have amplitudes  $E_x$  and  $E_y$  respectively,  $\nu$  is the frequency,  $\delta_x$  and  $\delta_y$  are angular phases and  $k = 2\pi/\lambda$  is the wave number.

The electric vector is thus described by a wave, travelling in the  $\hat{z}$  direction, which is the resultant of the two plane wave components in Eq. 1.1. Polarisation effects arise through differences in the amplitudes or phases of the individual components of the electric vector. When these differences arise, through time the tip of the electric vector will trace out a polarisation ellipse as described in the previous section and illustrated in Fig. 1.1, the sense of rotation being determined by the sign of the difference in phase,  $\delta_y - \delta_x$ , between the two components. In general the radiation field will be *elliptically* polarised with the special cases of *linear* polarisation when the phase difference is zero and left or right *circular* polarisation when the amplitudes are equal and the phase difference is  $\pm\pi/2$  respectively. Unpolarised (or natural) radiation occurs when the phases of the individual components have no fixed temporal differences between them and the amplitudes in any two orthogonal directions are equal. A mixture of such radiation and of polarised radiation

results in *partial* polarisation.

The four *Stokes Parameters* then determine the intensity of the radiation field and its polarisation state in terms of the polarisation ellipse, thus (e.g. Chandrasekhar, 1960 p27),

$$\begin{aligned}
 I &= E_y^2 + E_x^2 = I_y + I_x, \\
 Q &= E_y^2 - E_x^2 = I_y - I_x, \\
 U &= 2 E_y E_x \cos(\delta_y - \delta_x) = (I_y - I_x) \tan 2\psi, \\
 V &= 2 E_y E_x \sin(\delta_y - \delta_x) = (I_y - I_x) \sec 2\beta \sec 2\psi.
 \end{aligned}
 \tag{1.2}$$

The Stokes parameters are measurements of intensity variations and the proportionality constant relating the intensity and amplitude of the electric vector has been omitted. In Eq. 1.2  $I_y$  and  $I_x$  are the intensities of the components of the electric vector ( $I = \sqrt{\epsilon_0/\mu_0}E^2$ , where  $\epsilon_0$  and  $\mu_0$  are the permittivity and permeability of free space - e.g. Jackson, 1960),  $\psi$  is the angle that the major axis of the polarisation ellipse makes with the  $\hat{y}$  direction and  $\beta$  is an angle whose tangent is the ratio of the principal axes of the ellipse. With this definition the *eccentricity* of the ellipse is  $\sqrt{1 - \tan^2 \beta}$ .

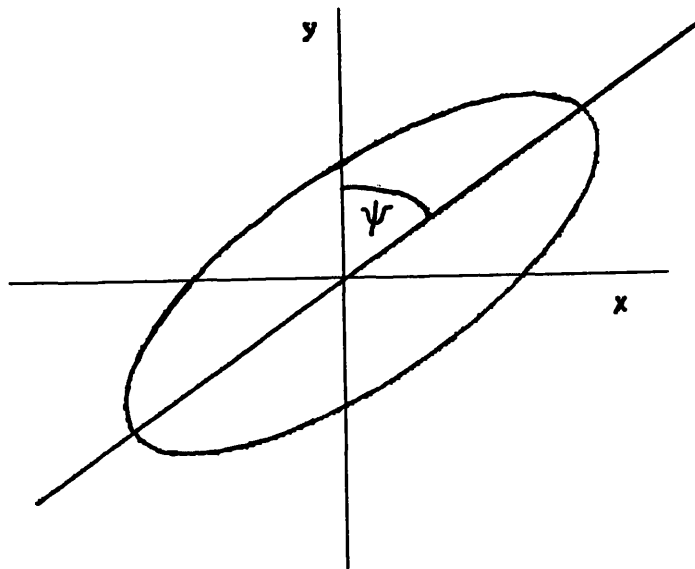


**Fig. 1.1** The polarisation ellipse traced out by the projection of the tip of the electric vector onto a plane perpendicular to the direction of travel of the electromagnetic wave.  $\psi$  is the angle which the major axis of the polarisation ellipse makes with the  $\hat{y}$  direction.

Physically these parameters represent the following;  $I$  is the total intensity of the radiation,  $Q$  is the difference in intensity between the components of the electric vector in the  $y$  and  $x$  directions,  $U$  is the difference in intensity between components of the electric vector along orthogonal axes rotated through 45 degrees from the  $y$  and  $x$  axes and  $V$  is the difference in intensity between

the left and right circularly polarised components of the radiation field. Schematically the Stokes parameters may be represented in the following way,

$$\begin{aligned}
 I &= \updownarrow + \leftrightarrow \\
 Q &= \updownarrow - \leftrightarrow \\
 U &= \nearrow - \searrow \\
 V &= \odot - \ominus
 \end{aligned}
 \tag{1.3}$$

where the double-headed arrows represent intensities in the aforementioned directions and the circular symbols represent the intensities of left and right circularly polarised radiation.

By combining measurements of the above intensity variations the four parameters specifying the polarisation ellipse may be determined, thus,

$$E_y = \frac{1}{\sqrt{2}}\sqrt{I+Q}, \quad E_x = \frac{1}{\sqrt{2}}\sqrt{I-Q}, \quad \tan 2\psi = \frac{U}{Q}, \quad \sin 2\beta = \frac{V}{\sqrt{Q^2+U^2+V^2}}, \tag{1.4}$$

where the proportionality constant has again been omitted.

In any radiation field the amplitudes and phases of the components of the electric vector are subject to continuous variations. However, in an elliptically polarised beam, these variations are such that the *ratio* of the amplitudes and the phase *difference* are absolute constants. What is therefore observed are the time-averaged intensities of the components of the electric vector. The Stokes parameters of such a radiation field are then given by combining the mean time averages of the intensities illustrated in Eq. 1.3. Furthermore, it may be shown that the Stokes parameters of a mixture of independent radiation fields is simply given by the sum of the individual Stokes parameters of the separate fields, viz,

$$\begin{aligned}
 I &= \sum_i I_i, \\
 Q &= \sum_i Q_i, \\
 U &= \sum_i U_i, \\
 V &= \sum_i V_i.
 \end{aligned}
 \tag{1.5}$$

This result has an obvious application when studying the net polarisation of an unresolved source (see Section 1.4).

This linear additivity of the Stokes parameters requires that the  $i$  individual parameters be referred to the same set of axes. Measurements of the Stokes parameters in different rectangular coordinate systems may be transformed to any rectangular coordinate system by a simple rotation formula. The Stokes parameters measured as  $(I, Q, U, V)$  in one rectangular coordinate system are

related to those in a system rotated clockwise through the angle  $\varphi$  by,

$$\begin{aligned} I' &= I, \\ Q' &= Q \cos 2\varphi + U \sin 2\varphi, \\ U' &= -Q \sin 2\varphi + U \cos 2\varphi, \\ V' &= V. \end{aligned} \tag{1.6}$$

In astronomical literature reference is often made to the *normalised Stokes*  $q$ ,  $u$ , and  $v$  parameters which are formed by dividing the parameters defined above by the total intensity,  $I$ , of the radiation field. The *degrees* of linear and circular polarisation,  $P$  and  $P_{\text{circ}}$ , and the polarisation *position angle*,  $\psi$ , are frequently presented instead of the Stokes parameters and are given by,

$$P = \frac{\sqrt{Q^2 + U^2}}{I}, \quad P_{\text{circ}} = \frac{V}{I}, \quad \psi = \frac{1}{2} \tan^{-1} \frac{U}{Q}. \tag{1.7}$$

This description allows a pictorial representation of linear polarisation in terms of a polarisation *quasi-vector* with magnitude  $P$  and direction given by  $\psi$ . Such polarisation vectors are frequently plotted on high spatial resolution maps and represent the direction of the maximum component of the electric vector. These dimensionless vectors are not subject to the usual rules of vector addition, but their dimensional components, the un-normalised Stokes parameters, may be combined following the rules of Eqn. 1.5.

Throughout this thesis the term “polarisation vector” refers to this quasi-vector defined above.

### 1.3 Production of polarised radiation in astronomy

In astronomy polarised radiation arises through several mechanisms and analysis of the polarisation can yield information on the source of the polarisation unobtainable from spectroscopy and photometry alone. The information to be gained depends on the polarising mechanism and the ability to determine which mechanism is responsible for producing the polarisation in the system under observation. Details of the main polarising mechanisms at work in astronomical systems and the physical information obtainable from analysis of the polarimetric variations with time and wavelength are given below.

#### 1.3.1 Scattering

Scattering results in polarisation due to anisotropies in the angular redistribution of the scattered components of the electric vector. In describing the polarisation of scattered radiation it is convenient to define a scattering plane – the plane which contains the source of radiation, the scatterer and the observer. The intensity and polarisation state of the scattered radiation are then determined by (Section A.3) the scattering opacity or cross section and the *redistribution function* which

determines the frequency and angular distribution of the scattered intensity components parallel and perpendicular to the scattering plane. Depending on the physical properties of the scattering particle, such as its size, shape, refractive index, etc, this redistribution function can take quite complex forms – cf Van de Hulst (1950).

The discovery that when unpolarised radiation is scattered the intensities of scattered radiation parallel and perpendicular to the scattering plane are in the ratio  $\cos^2 \Theta : 1$  ( $\Theta$  being the angle between incident and scattered directions) was noted by Malus in 1808. This particular form of the angular redistribution function has since come to be known as the *Rayleigh phase function* after Lord Rayleigh who formulated the phase function for scattering off particles whose size was small compared to the wavelength of incident radiation. Rayleigh undertook this analysis in 1871 while investigating the polarisation and blue colour of the sunlit sky – the angular phase function determining the polarisation while the blue colour was attributed to the preferential scattering of short wavelength radiation described by the scattered intensity being inversely proportional to the fourth power of the incident wavelength. The Rayleigh angular phase function also applies to Thomson scattering off free electrons.

Thomson scattering is important in the envelopes of hot stars where, due to high ionisation levels, the number density of free electrons can be very high. Analysis of the continuum polarisation arising from scattering in such envelopes yields constraints on the envelope geometry, (Brown and McLean, 1977), and this thesis will show how high resolution observations of the polarisation variations with time and wavelength will allow the observer to determine stellar mass loss rate variations and the velocity and density distributions in circumstellar envelopes. Since Thomson scattering is the main polarising mechanism to be investigated in this thesis a detailed analysis of the polarisation produced by single scattering of stellar radiation in axisymmetric circumstellar envelopes of single stars is given at the end of this chapter.

Resonance or fluorescence line radiation arises when an atom is raised to an excited state by an external radiation field or particle beam. If the exciting field or particles are anisotropic this imposes an asymmetry on the system and in the subsequent de-excitation the atom emits line radiation such that the parallel and perpendicular components of the emitted electric vector depend on the initial,  $j$ , and final,  $j + \Delta j$ , angular momentum states of the atom and also the angle between the incident exciting beam and the emitted radiation (Hamilton, 1947), thus giving rise to linear polarisation in the line. For  $j = 0$ ,  $\Delta j = 1$  the line radiation is emitted in accordance with the Rayleigh angular phase function. Polarisation of the Hydrogen- $\alpha$  line in solar flares (Henoux, et al, 1990) has been attributed to excitation of the Hydrogen atoms by proton or electron beams or flows (Fletcher, 1993), the levels of polarisation attained yielding information on the energy of the exciting particles and hence a handle on the source of energy in solar flares.

### 1.3.2 Synchrotron radiation

Electromagnetic theory predicts the emission of radiation from accelerating charged particles. Synchrotron radiation is one such example of this arising through the accelerations experienced by relativistic electrons as they spiral around a magnetic field. Detailed analysis (e.g. Rybicki and Lightman, 1979) shows that the radiation produced by the electrons is linearly polarised with the maximum component of the electric vector being perpendicular to the magnetic field. In general the electron distribution is not mono-energetic resulting in a frequency dependence of the emitted radiation. When the number of electrons at a given energy can be expressed as a power law,  $N(E) = N_0 E^{-\alpha}$ , the frequency dependence of the resultant synchrotron intensity spectrum also follows a power law such that  $I(\nu) = I_0 \nu^{-\beta}$ , where  $\beta = (\alpha - 1)/2$ . By considering the intensities of the emitted electric vector parallel and perpendicular to the magnetic field, the degree of linear polarisation turns out to be,

$$P = \frac{\alpha + 1}{\alpha + \frac{7}{3}}, \quad (1.8)$$

which is independent of frequency (when the electron energy distribution is a power law). Typical values for the power law index can yield values of  $P$  up to 70%. However, such high values are not realised in practice due to subsequent depolarisation of the radiation by other mechanisms prior to observation (see below) including variation in the magnetic field direction along the line of sight. The signature of synchrotron radiation from a power law distribution of electrons is therefore a power law intensity spectrum accompanied by a flat polarisation spectrum. Analysis of synchrotron spectra can yield the underlying electron energy distribution and, if the source can be resolved, the direction of polarisation determines the alignment of the local magnetic field which cannot be inferred from measurements of the spectra alone.

### 1.3.4 Interstellar polarisation

Observations of astronomical objects are all subject to interstellar polarisation which arises due to selective attenuation of one component of the radiation field by dust grains in the interstellar medium. These dust grains are believed to be elongated in one direction with this long axis aligned – through the Davis–Greenstein mechanism – perpendicular to the interstellar magnetic field. Unpolarised radiation which traverses a region containing aligned grains becomes polarised, in a direction parallel to the component of the magnetic field perpendicular to the line of sight, because the component of the electric vector parallel to the grain axis is extinguished in preference to other components. This mechanism accounts for the polarisation observed in many stars and may be used to map the interstellar magnetic field (Matheson & Ford, 1970). The wavelength dependence of this polarisation was found, by Serkowski (1973), to follow an empirical law, viz,

$$\frac{P(\lambda)}{P_{\max}} = \exp[-K \ln^2(\lambda/\lambda_{\max})], \quad (1.9)$$

where  $P_{\max}$  is the magnitude of the polarisation at  $\lambda_{\max}$  and  $K$  is a constant determined by fitting the above law to many observations. The currently accepted value is, Whittet et al. (1991),

$K = 0.01 \pm 0.05 + (1.66 \pm 0.09)\lambda_{\max}$ . Recent results of the ASTRO-1 space mission, which explored polarisation in the ultraviolet, have shown that this law fails at very short wavelengths (Clayton et al, 1992) demonstrating the need for a fuller *physical* understanding of interstellar polarisation.

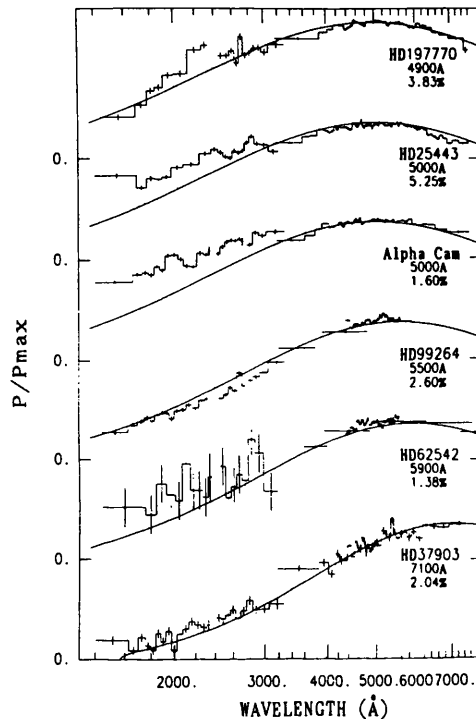


Fig. 1.2 WUPPE data from Clayton et al 1992 illustrating the failure of the Serkowski law in predicting the wavelength dependence of the interstellar UV continuum polarisation.

A further effect which arises when radiation traverses the interstellar medium is Faraday rotation, which rotates the major axis of the polarisation ellipse and is significant at radio wavelengths. This is a plasma effect which occurs due to the presence of the interstellar magnetic field and the fact that the radiation field can be written as the linear superposition of two oppositely polarised modes of circular polarisation (Chandrasekhar, 1960, p31). The refractive index for the two modes is different in the region containing the magnetic field so one travels faster than the other and an additional phase difference is introduced between the modes. As stated earlier this results in a rotation of the polarisation ellipse and the magnitude of this effect is determined by the *rotation measure* which is proportional to the line integral along the line of sight from the source to the observer of the interstellar electron number density times the component of the magnetic field parallel to the line of sight. Faraday rotation is proportional to the square of the wavelength observed (hence the importance at long wavelengths – e.g. the radio region) so, in principle, measurements of Faraday rotation at different wavelengths can yield information on the interstellar magnetic field and particle number density.

When investigating any polarisation which is *intrinsic* to the object under observation the observations must be corrected to account for the effects of interstellar polarisation and, at radio wavelengths, Faraday rotation.

#### 1.4 Polarisation from optically thin circumstellar envelopes

An accurate determination of the levels of polarisation expected from the propagation of radiation through a stellar atmosphere requires a full radiative transfer treatment incorporating the effects of scattering, absorption, emission (and re-emission) of the radiation field throughout the region in question. In general such treatments do not have analytic solutions for the intensity and polarisation state of the emergent radiation field, but under certain simplifying assumptions as to the geometry and physical make-up of the interaction region solutions can be found.

Chandrasekhar presented the problem of radiative transfer in a plane parallel electron scattering atmosphere, the solution of which predicts local polarisation levels of up to 12% due to electron scattering at the stellar limb. However, since most stars are unresolvable, the net polarisation observed is much less than this theoretical value due to cancellation of the local polarisation vectors when summed over the entire star. This cancellation effect is most easily visualised when considering the polarisation arising from scattering of radiation from a point source at the centre of a spherical envelope. At any point in the envelope the local polarisation vector is perpendicular to the radial line from the source. The components of this vector, the Stokes parameters, will cancel with the components of the scattered polarisation vector from a point which is exactly one quadrant away. Summing the components of the local scattered polarisation vectors over any annulus (and hence the entire region) will thus result in zero net polarisation. Any residual polarisation from a pure electron scattering atmosphere must therefore be due to the region being non-spherical in some way (e.g. geometry, density, opacity distribution, temperature, etc).

As so often occurs in theoretical modelling, the general formulation of a problem is often analytically intractable and the solution must be computed numerically. Once numerical results have been found the insight from these may help in establishing reasonable simplifications to the original formulation so as to isolate the effects of different physical processes and present the problem in a more analytic form. This sequence of events has occurred in the study of polarisation from stellar atmospheres. Numerical radiative transfer solutions to the stellar scattering problem from, among others, Collins (1968) and Cassinelli (1974) predicted the degree of polarisation to be expected from non-spherical circumstellar envelopes which included opacity sources as well as electron scattering. The chief problem with such approaches is that the basic physical considerations and parameter dependence tend to be lost in the numerical details, thus inhibiting further diagnostic use of any polarimetric observations to determine physical properties of the region. A major advance in the theoretical modelling of polarisation from electron scattering extended circumstellar envelopes occurred in 1977 when Brown & McLean presented their optically thin single scattering theory. In their analysis polarisation arose through single Thomson scattering of radiation from a point stellar source in any optically thin, axisymmetric circumstellar envelope. The resultant degree of polarisation was found to depend linearly on three envelope parameters,

namely its average optical depth, shape factor and  $\sin^2$  of the axial inclination,  $i$ , to the line of sight, while the polarisation direction was parallel to the rotational axis of the envelope. These results explained and generalised trends only hinted at by previous numerical results. Subsequent analysis has extended this theory to incorporate the effects of a finite source of radiation (Cassinelli et al, 1987, Brown et al, 1989) and occultation of the scattering material by the finite source (Fox, 1991).

Brown & McLean's original paper determined the net polarisation by summing over the entire scattering region intensity differences of the radiation scattered at each point. In what follows I shall present the analysis in a slightly different way, by considering the equation of radiative transfer under the assumption that optically thin electron scattering is the only opacity source – the final results determining the degree of polarisation are, of course, the same.

#### 1.4.1 General formalism

In the single scattering approximation the time independent equation of radiative transfer for initially unpolarised light, Thomson scattered in an optically thin region, without absorption or local emission, may be written as (A.24),

$$\hat{\mathbf{k}} \cdot \nabla \mathbf{I}_\nu = \rho \mathbf{j}_\nu, \quad (1.10)$$

where  $\hat{\mathbf{k}}$  is the unit vector from the scattering element to the observer and  $\mathbf{I}_\nu$  is the scattered Stokes vector whose intensity-like elements are the un-normalised Stokes parameters.  $\rho$  is the mass density of scatterers and  $\mathbf{j}_\nu$  is the Stokes emission coefficient due to single scattering of the incident radiation which is given by (A.23),

$$\mathbf{j}_\nu = \frac{1}{4\pi} \int_{\nu_*} \int_{\Omega_*} \kappa_{\nu_*} \mathbf{R}_{\nu_*}(\nu_*, \hat{\mathbf{k}}_*; \nu, \hat{\mathbf{k}}) \mathbf{I}_{\nu_*} d\Omega_* d\nu_*. \quad (1.11)$$

$\kappa_{\nu_*}$  is the scatterer opacity per unit mass,  $\mathbf{I}_{\nu_*}$  is the incident Stokes vector at frequency  $\nu_*$ ,  $\Omega_*$  is the solid angle subtended at the scatterer by the source of radiation and  $\mathbf{R}_{\nu_*}(\nu_*, \hat{\mathbf{k}}_*; \nu, \hat{\mathbf{k}})$  is the redistribution function which gives the probability of a photon of frequency  $\nu_*$ , incident in solid angle  $d\Omega_*$ , about direction  $\hat{\mathbf{k}}_*$ , being scattered with frequency  $\nu$  into solid angle  $d\Omega$ , about direction  $\hat{\mathbf{k}}$ .

For Thomson scattering the redistribution function may be written as a frequency term multiplied by an angular scattering matrix. For scattering radiation of energy  $\ll m_e c^2$  off *stationary* electrons the incident and scattered frequencies are equal, so the frequency part of the redistribution function is,

$$R(\nu_*, \nu) = \delta(\nu_* - \nu). \quad (1.12)$$

The angular part is given by the Rayleigh phase function viz,

$$R(\hat{\mathbf{k}}_*, \hat{\mathbf{k}}) = \frac{3}{4} \begin{pmatrix} 1 + \cos^2 \Theta & \sin^2 \Theta & 0 & 0 \\ \sin^2 \Theta & 1 + \cos^2 \Theta & 0 & 0 \\ 0 & 0 & 2 \cos \Theta & 0 \\ 0 & 0 & 0 & 2 \cos \Theta \end{pmatrix}, \quad (1.13)$$

where  $\Theta$  is the scattering angle given by  $\cos \Theta = \hat{\mathbf{k}}_s \cdot \hat{\mathbf{k}}$ . Equation 1.10 now has the solution,

$$\mathbf{I}_\nu = \int_{l_1}^{l_2} \rho \mathbf{j}_\nu dl . \quad (1.14)$$

That is, the observed Stokes vector is the line integral of  $\rho \mathbf{j}_\nu$  along a line of sight,  $\hat{\mathbf{k}}$ , through the scattering region, see Fig. 1.3 This assumes there is no further scattering or absorption between the edge of the scattering region and the observer.

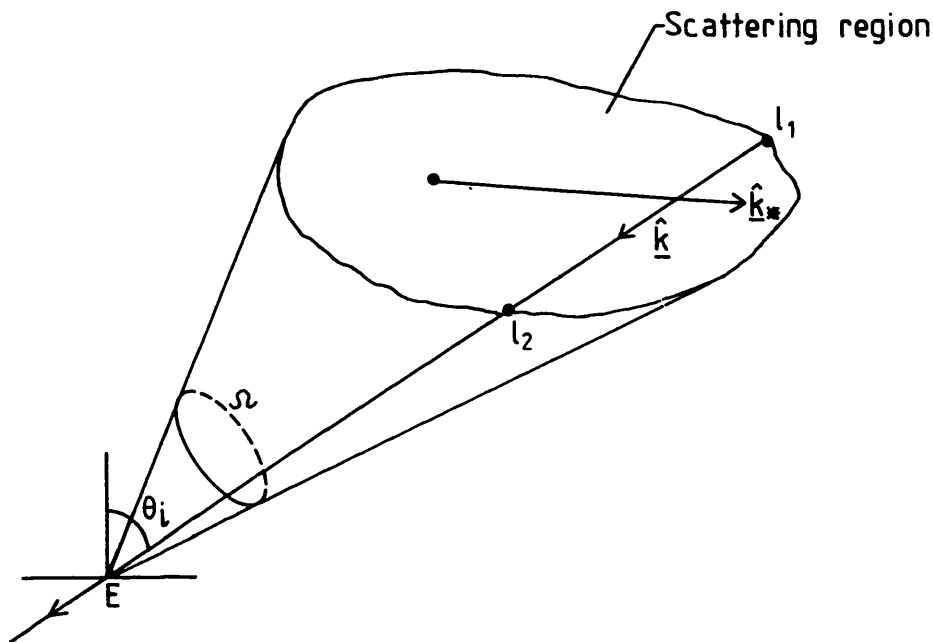


Fig. 1.3 Intensity scattered from direction  $\hat{\mathbf{k}}_s$  into the line of sight direction  $\hat{\mathbf{k}}$ . The specific intensity at earth,  $E$ , is obtained by integrating  $\rho \mathbf{j}_\nu$  through the scattering region from  $l_1$  to  $l_2$ .  $\theta_i$  is the angle between the line of sight and the normal to the surface at  $E$  and  $\Omega$  is the solid angle subtended by the entire scattering region at the earth.

The observed Stokes vector flux,  $\mathbf{F}_\nu$ , is given by (A.2),

$$\mathbf{F}_\nu = \int_{\Omega} \mathbf{I}_\nu \cos \theta_i d\Omega , \quad (1.15)$$

where  $\theta_i$  is the angle between the incident radiation and the normal to the surface  $dA$  and  $\Omega$  is the solid angle subtended by the entire scattering region - see Fig. 1.3. The components of the Stokes vector flux are the related fluxes of the Stokes parameters, thus,

$$\mathbf{F}_\nu = \begin{pmatrix} F_\nu^I \\ F_\nu^Q \\ F_\nu^U \\ F_\nu^V \end{pmatrix} . \quad (1.16)$$

This gives,

$$\mathbf{F}_\nu = \int_{\Omega} \int_{l_1}^{l_2} \rho \mathbf{j}_\nu \cos \theta_i dl d\Omega . \quad (1.17)$$

Since  $dV = l^2 dl d\Omega$ , the flux can be written as a volume integral over the scattering region thus,

$$\mathbf{F}_\nu = \int_V \rho \mathbf{j}_\nu \cos \theta_i \frac{dV}{l^2} . \quad (1.18)$$

In the limit where the distances within the scattering region are very much less than the source-observer distance,  $D$ , then  $l \approx D$  and  $\cos \theta_i$  is constant. Furthermore, if the area  $dA$  is perpendicular to the incident radiation (e.g. when a telescope is pointed directly at a source) then  $\cos \theta_i = 1$ , giving,

$$\mathbf{F}_\nu = \frac{1}{D^2} \int_{V_*} \rho \mathbf{j}_\nu dV . \quad (1.19)$$

Equation 1.9 yields the Stokes fluxes in the scatterer's local coordinate system, i.e. with respect to the scattering plane. When calculating the Stokes fluxes from the entire scattering region it is necessary to refer the Stokes fluxes due to each scatterer to the same set of axes. This is achieved by multiplying the angular redistribution matrix by the matrix  $\mathbf{L}$  (cf Eq. 1.6) which rotates the local axes through the angle  $\psi$  which is the angle between the normal to the scattering plane (the plane containing  $\hat{\mathbf{k}}_*$  and  $\hat{\mathbf{k}}$ ), and the chosen Stokes Q-axis for the entire region, thus,

$$\mathbf{L} = \begin{pmatrix} 1 & 0 & 0 & 0 \\ 0 & \cos 2\psi & \sin 2\psi & 0 \\ 0 & -\sin 2\psi & \cos 2\psi & 0 \\ 0 & 0 & 0 & 1 \end{pmatrix} . \quad (1.20)$$

For initially unpolarised light,

$$\mathbf{I}_{\nu*} = \begin{pmatrix} I_{\nu*} \\ 0 \\ 0 \\ 0 \end{pmatrix} , \quad (1.21)$$

which, using  $\rho \kappa_\nu = n \sigma_T$  (A.13), with  $n$  the electron number density and  $\sigma_T$  the Thomson scattering cross section, leads to the equation,

$$\mathbf{F}_\nu = \frac{3 \sigma_T}{16 \pi D^2} \int_V \int_{\Omega_*} n I_{\nu*} \mathbf{P} d\Omega_* dV , \quad (1.22)$$

where,

$$\mathbf{P} = \begin{pmatrix} 1 + \cos^2 \Theta \\ \sin^2 \Theta \cos 2\psi \\ -\sin^2 \Theta \sin 2\psi \\ 0 \end{pmatrix} . \quad (1.23)$$

Equation 1.22 is the general equation for determining the Stokes fluxes due to Thomson scattering of initially unpolarised radiation in an optically thin region. The inner integral is over all incident light rays,  $d\Omega_* = \sin \eta d\eta d\xi$ , the outer integral is over all scattering particles,  $dV = r^2 \sin \theta dr d\theta d\phi$  and the scattering geometry presented in Fig. 1.4 enables the angles  $\Theta$  and  $\psi$  to be expressed in terms of  $i$ ,  $\eta$ ,  $\xi$ ,  $\theta$  and  $\phi$ .

The normalised Stokes parameters are now defined in terms of the Stokes fluxes above, thus,

$$q(\nu) = \frac{F_\nu^Q}{F_\nu^D + F_\nu^I} , \quad u(\nu) = \frac{F_\nu^U}{F_\nu^D + F_\nu^S} . \quad (1.24)$$

In the present case of single Thomson scattering in an optically thin region, the scattered flux,  $F_\nu^I$ , is much less than the direct flux  $F_\nu^D$  unless the light source is highly anisotropic (Almalki, 1992), giving,

$$q(\nu) \approx \frac{F_\nu^Q}{F_\nu^D}, \quad u(\nu) \approx \frac{F_\nu^U}{F_\nu^D}, \quad (1.25)$$

where the direct flux from the source is,

$$F_\nu^D = \int_{\Omega} I_\nu d\Omega = \frac{\pi R^2}{D^2} I_\nu. \quad (1.26)$$

The degree of linear polarisation,  $P_\nu$ , and position angle,  $\Psi_\nu$ , for the entire region are given by,

$$P = \sqrt{q^2 + u^2}, \quad \Psi = \frac{1}{2} \tan^{-1} \left( \frac{u_\nu}{q_\nu} \right). \quad (1.27)$$

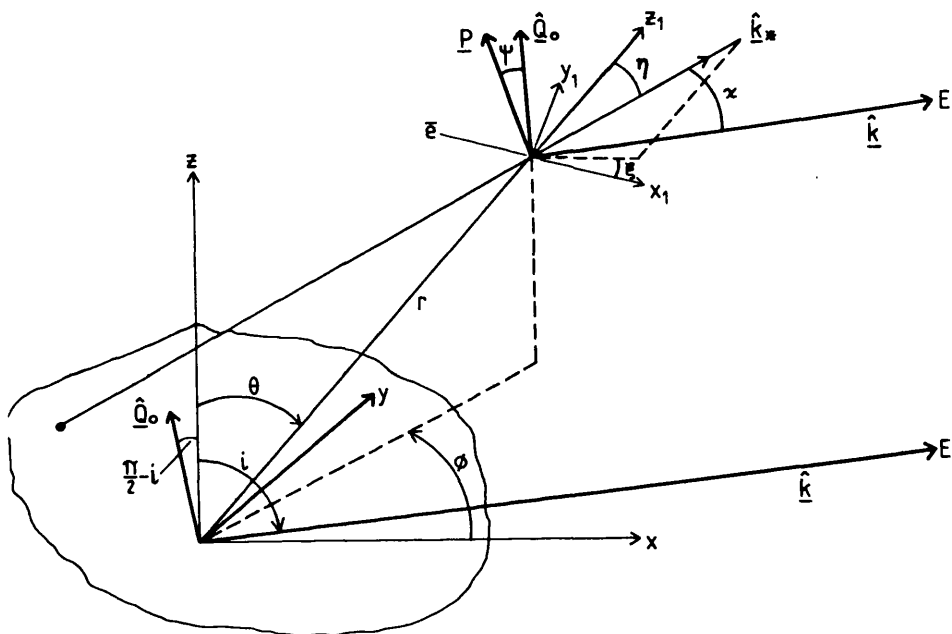


**Fig. 1.4** A source of radiation is centred at the origin of the cartesian co-ordinate system  $(x, y, z)$ . An observer at inclination  $i$  to the rotational ( $z$ ) axis of the star is positioned at infinity along  $\hat{\mathbf{k}}$  in the  $x$ - $z$  plane. An electron at position  $(r, \theta, \phi)$  scatters radiation incident in solid angle  $d\Omega_* = \sin \eta d\eta d\xi$  through the angle  $\Theta$  towards the observer, with  $\cos \Theta = \hat{\mathbf{k}}_x \cdot \hat{\mathbf{k}}$ . The Stokes  $Q$ -axis for the entire system is shown, being the projection on the sky of the stellar rotation axis,  $\hat{\mathbf{Q}}_0 = (-\cos i, 0, \sin i)$ . The direction of vibration of the local polarisation vector,  $\mathbf{P}$ , at  $(r, \theta, \phi)$  is perpendicular to the plane defined by  $\hat{\mathbf{k}}_x$  and  $\hat{\mathbf{k}}$ , with the polarisation position angle,  $\psi$ , the angle between  $\mathbf{P}$  and  $\hat{\mathbf{Q}}_0$ .

Now that the general single scattering formalism has been set up a summary of the various approximations invoked, beginning with those of Brown & McLean, and the subsequent improvements shall be presented.

#### 1.4.2 Unpolarised point source, axisymmetric envelope

Brown & McLean's assumption of an unpolarised point source of radiation and no frequency

redistribution of the scattered radiation (Eq. 1.12) reduces Eq. 1.11 to,

$$\mathbf{j}_\nu = \frac{1}{4\pi} \frac{\pi R^2}{r^2} \kappa_\nu \mathbf{P} I_\nu, \quad (1.28)$$

which is valid for  $R \ll r$ . The scattering geometry for a point source is obtained from Fig. 1.4 by setting  $\eta = 0$  allowing  $\mathbf{P}$  to be expressed in terms of the angles  $\theta, \phi, i$ . With these assumptions Eq. 1.22 becomes,

$$\begin{aligned} \begin{pmatrix} F_\nu^I \\ F_\nu^Q \\ F_\nu^U \end{pmatrix} &= \frac{3\sigma_T R^2}{32 D^2} \int_R^\infty \int_0^\pi \int_0^{2\pi} n(r, \theta, \phi) I_\nu, \\ &\times \begin{pmatrix} (3 - \cos^2 i) - (1 - 3 \cos^2 i) \cos^2 \theta + \sin^2 i \sin^2 \theta \cos 2\phi + \sin 2i \sin 2\theta \cos \phi \\ \sin^2 i (1 - 3 \cos^2 \theta) - (1 + \cos^2 i) \sin^2 \theta \cos 2\phi + \sin 2i \sin 2\theta \cos \phi \\ 2 \cos i \sin^2 \theta \sin 2\phi - 2 \sin i \sin 2\theta \sin \phi \end{pmatrix} \sin \theta dr d\theta d\phi, \end{aligned} \quad (1.29)$$

where the limits on the  $r$ -integral are from the stellar surface,  $r = R$ , to the outer edge of the scattering envelope, which has been written here as  $\infty$ . The further assumption of axisymmetry then yields,

$$\begin{pmatrix} F_\nu^I \\ F_\nu^Q \\ F_\nu^U \end{pmatrix} = \frac{3\pi\sigma_T R^2}{16 D^2} \int_R^\infty \int_0^\pi n(r, \theta) I_\nu \begin{pmatrix} (3 - \cos^2 i) - (1 - 3 \cos^2 i) \cos^2 \theta \\ \sin^2 i (1 - 3 \cos^2 \theta) \\ 0 \end{pmatrix} \sin \theta dr d\theta, \quad (1.30)$$

Since  $F_\nu^U = 0$  the degree of linear polarisation is simply  $P = Q = F_\nu^Q / F_\nu^D$  (for  $F_\nu^I \ll F_\nu^D$ ) which, in the notation of Brown & McLean, with  $\mu = \cos \theta$  may be written as,

$$P = 2\bar{\tau}(1 - 3\gamma) \sin^2 i, \quad (1.31)$$

where  $\bar{\tau}$  is an average envelope optical depth,

$$\bar{\tau} = \frac{3}{32} \sigma_T \int_r \int_{-1}^1 n(r, \mu) d\mu dr, \quad (1.32)$$

and the shape factor,  $\gamma$ , is,

$$\gamma = \frac{\int_{-1}^1 n(r, \mu) \mu^2 d\mu dr}{\int_{-1}^1 n(r, \mu) d\mu dr}. \quad (1.33)$$

The extreme limits of  $\gamma$  are 0 for a plane disc and 1 for a "polar line", while  $\gamma = 1/3$  corresponds to a spherical electron distribution resulting in zero net polarisation, in accordance with the description given above for scattering in a spherical envelope. As was stated earlier the net polarisation arising from the above circumstances depends only on three parameters, which means that a measurement of the polarisation cannot tie down the physical make-up of the scattering region since there are infinitely many combinations of  $i, \bar{\tau}$  and  $\gamma$  which could give rise to the observed  $P$ . However, the above considerations allow certain geometric models to be discounted. For example, noting that

for  $0 \leq \gamma \leq 1/3$  and  $0 \leq \sin^2 i \leq 1$  then  $P \leq 2\bar{\tau}$ , so constraints can be placed on the average optical depth and hence, if the average electron density can be estimated (e.g. by measurements of Stark broadened spectral lines, Griem, 1960), a typical length scale for the scattering region can be inferred.

Brown & McLean's single scattering analysis leads to an upper limit on the absolute value of the net polarisation to be expected from electron scattering envelopes since other considerations, presented below, in most cases serve to reduce the scattered polarised flux and hence the net polarisation (though the relative variation with  $i$ , etc. is comparatively unchanged)

#### 1.4.3 Depolarisation factor for a finite spherical source

Due to the  $1/r^2$  fall off of stellar flux prior to scattering, most of the polarised flux will arise from a scattering region close to the source and for this reason the effect of a finite sized source has been investigated by several authors. Cassinelli et al. (1987) found that, for an unpolarised spherical source, the integral over all incident rays,  $d\Omega_*$ , in the Stokes  $Q$  and  $U$  fluxes, in Eq. 1.22 reduced to the specific intensity multiplied by a simple geometric factor,  $D(r)$ , thus,

$$D(r) = \sqrt{1 - \frac{R^2}{r^2}} \quad (1.34)$$

while Brown et al. (1989) found that for the scattered Stokes  $I$  flux the geometric correction factor was,

$$C(r) = \frac{8 - D(r)[1 + D(r)][1 - 3 \cos^2 \Theta]}{3[1 + D(r)][1 + \cos^2 \Theta]} \quad (1.35)$$

$C(r)$  and  $D(r)$  are known as the *intensity correction* and *depolarisation* factors which may be inserted directly into the integrals in Eq. 1.29 ( $C(r)$  in the  $F_\nu^I$  integral and  $D(r)$  in the  $F_\nu^Q$  and  $F_\nu^U$  integrals) to determine the net polarisation from an envelope illuminated by a central spherical source. These factors serve to increase the scattered  $I$  flux and decrease the  $Q$  and  $U$  fluxes, thus leading to a reduction in the net polarisation from that determined by Eq. 1.31 above. Brown et al. (1989) extended their analysis to account for the effects of limb darkening in a spherical source and they also calculated the analogous correction and depolarisation factors for scattering of radiation from accretion discs in narrow co-axial jets.

#### 1.4.4 Occultation effects

Due to the finite size of the radiation source part of the scattering envelope is occulted and photons scattered in this volume are unable to reach the observer. In a series of papers (Brown & Fox, 1989, Fox & Brown, 1991, Fox, 1991) this effect was investigated and incorporated into the single scattering formalism by replacing the volume integral in Eq. 1.22 by an integral over the entire scattering volume *minus* the volume occulted by the source. The main scattering geometry which shall be investigated in this thesis is that of a planar disc for which the relevant limits of integration shall now be quoted.

For the case of a planar disc the analysis presented by Fox & Brown (1991), with  $x = r/R$ , gives the integral operator as,

$$\int_A = \int_1^{\alpha_D} \int_0^{2\pi} - \int_1^{\delta} \int_{\frac{\pi}{2} + \phi(x)}^{\frac{3\pi}{2} - \phi(x)}, \quad (1.36)$$

where,

$$\begin{aligned} \delta &= \sec i & \text{for } \alpha_D > \sec i, \\ \delta &= \alpha_D & \text{for } \alpha_D < \sec i, \end{aligned} \quad (1.37)$$

with the radius of the disc being  $\alpha_D$  (in units of stellar radii) and

$$\phi(x) = \sin^{-1} \left\{ \frac{(1 - x^{-2})^{\frac{1}{2}}}{\sin i} \right\}. \quad (1.38)$$

When occultation is included in the analysis various effects occur. For the case of scattering in a planar disc Fox & Brown (1991) found, that for low inclinations, occultation serves to enhance the polarisation, while for high values of inclination it has the effect of reducing the polarisation. The explanation of this is that for low inclinations the net polarisation from the entire disc will be near zero with the polarisation vector parallel to the projection on the sky of the stellar rotation axis, while the occulted part of the disc is polarised perpendicular to this direction. When the latter is subtracted from the polarisation of the disc as a whole the observable polarisation is enhanced. At high inclinations the polarisation vector of the occulted region will be parallel to that of the entire disc, so subtracting this reduces the net polarisation. Similar effects occur when scattering in spherical envelopes with axisymmetric, non-spherical density distributions. Also the net polarisation depends upon inclination in a more complicated way than the  $\sin^2 i$  dependence of Brown & McLean.

#### 1.4.5 Other continuum opacity sources in an optically thin envelope

The presence of opacity sources other than electron scattering will modify the wavelength dependence of the incident (and scattered) radiation in the circumstellar envelope. In the case of Hydrogen, its continuum absorptive opacity is proportional to  $\lambda^3$  with discontinuities across series limits (e.g. Mihalas, 1978). Following on from a radiative transfer treatment of Haisch & Cassinelli (1976) the effect of this opacity source in an optically thin disc was investigated by McLean (1979). He modified the Brown & McLean treatment by including the factor  $\exp[-\tau_a(\lambda)] \approx 1 - \tau_a(\lambda)$  which allows for attenuation of the stellar flux prior to scattering, where  $\tau_a(\lambda)$  is the optical depth for absorption. For optically thin absorption this results in a wavelength dependence of the scattered continuum polarisation, such that the polarisation decreases longward of any series limits with a sudden increase on crossing the next limit - Fig. 1.5. This scenario has been proposed for the Balmer jump in polarisation which is evident in the observations of Be stars by Bjorkman (1992), but the theory fails to predict the wavelength dependence for the continuum polarisation

measured in the ultraviolet – Fig. 1.6. This discrepancy between theory and observation was one of the surprising results of the recent UV polarimetry space mission and preliminary modelling efforts (Bjorkman, 1993) suggest that the solution to the problem may be found by considering the deformation of the central star by rapid rotation. The equatorial bulging induced by rapid rotation results in the equator being cooler than the polar regions such that any Thomson scattering electrons in an equatorial disc will scatter this cooler radiation. An external observer will then see this cooler polarised flux diluted by the hotter direct flux from all (including the polar regions) of the star and hence the net polarisation will be less than that expected from a spherical, isothermal source.

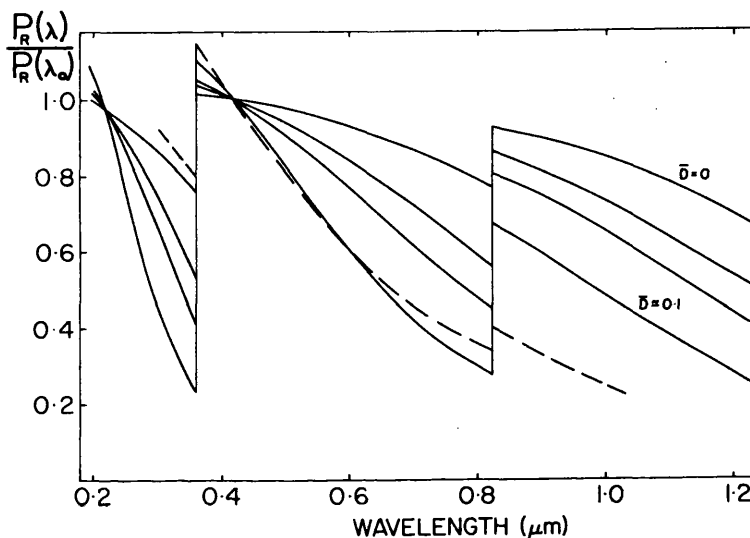
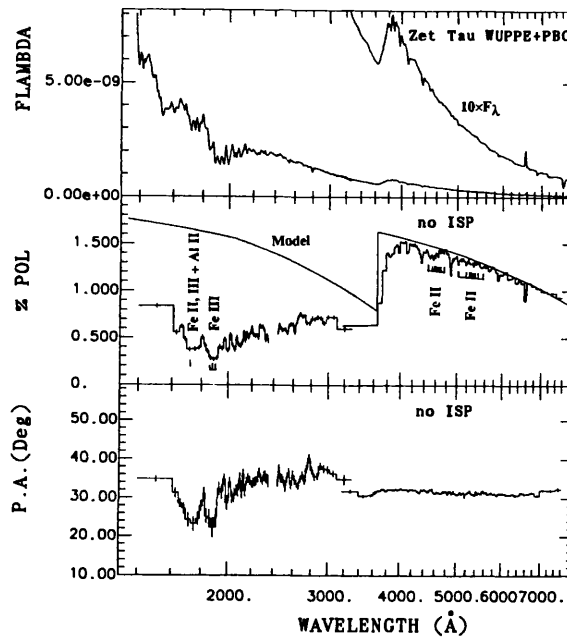


Fig. 1.5 McLean's (1979) variation of the relative wavelength dependence of the continuum polarisation arising from scattering of stellar radiation in an axisymmetric disc with Hydrogen continuum opacity and also the diluting effect of direct envelope emission ( $\bar{D}$  being the ratio of unpolarised envelope emission to direct stellar flux). The dashed curve is the results of a radiative transfer model by Haisch & Cassinelli (1970).

McLean's 1979 paper also investigated the addition of optically thin, unpolarised emission from the envelope itself and illustrated how the continuum polarisation would be modified depending on how strong this diffuse emission was compared to the direct stellar flux. This paper is an example of how the effects of different physical processes may be incorporated in a quantitative semi-analytic analysis, without having to revert to numerically intensive radiative transfer codes. These numerical codes, however, are required to check the validity of such simplistic approaches and also to investigate effects which cannot be explained by analytic approximations. As will be discussed in the next section, the single scattering theory, incorporating the above modifications, turns out to give the correct variations with wavelength of the polarisation produced in optically thin envelopes, but overestimates the degree of polarisation when the envelope optical depth becomes large.



**Fig. 1.6** WUPPE results from Bjorkman et al (1992) showing the observed continuum polarisation of the Be star  $\zeta$  Tau and also the predicted polarisation arising from Thomson scattering of stellar radiation in an envelope which is a source of Hydrogen continuum opacity – note the failure of the model at UV wavelengths.

#### 1.4.6 How valid is the single scattering theory ?

Since the publication of the Brown & McLean theory several authors have investigated, through radiative transfer codes and Monte Carlo simulations, the regimes in which the single scattering approximations are valid. The main shortcoming of the single scattering theory is that it predicts a net polarisation which rises linearly with the envelope optical depth. This cannot be correct for large optical depths since multiple scattering will serve to randomise the scattered polarisation vectors and lead to a reduction in the polarisation.

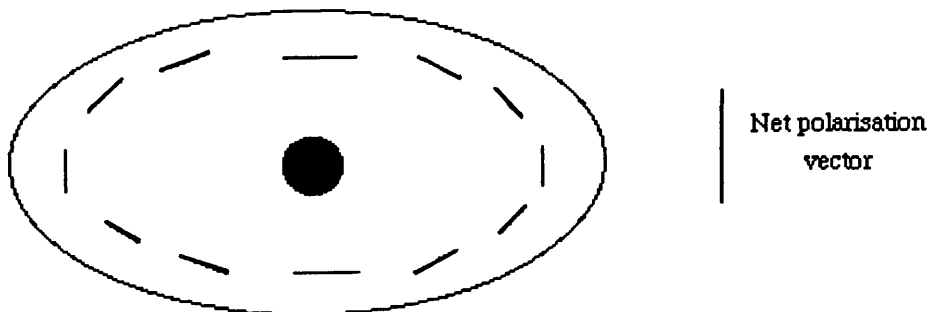


**Fig. 1.7** Polarisation vectors arising from Thomson scattering radiation from a point source in an axisymmetric envelope. The net polarisation vector from the entire envelope is parallel to the projection of the rotational symmetry axis on the plane of the sky.

Monte Carlo simulations of multiple scattering by Daniel (1980) showed that the Brown & McLean analysis was very good for envelopes with an equatorial electron scattering optical depth  $\leq 0.1$ , corresponding to  $\bar{\tau} \leq 0.03$ . Below this value the polarisation rises with  $\bar{\tau}$  since the probability of

multiple scattering is small so the polarisation vectors of the emergent radiation are perpendicular to the radial line from the central source giving a net polarisation parallel to the symmetry axis of the envelope – Fig. 1.7. As the optical depth increases and multiple scattering begins to dominate, the emergent polarisation vectors become more and more randomly oriented since the radiation has encountered many different scattering planes along its path. The resultant polarisation from these randomly oriented polarisation vectors is less than the single scattering case. As a function of optical depth the polarisation, Fig. 1.8, rises to a maximum value after which it decreases, reaching zero at infinite optical depth where the radiation field has *thermalised* and is hence unpolarised.

The inclusion of other opacity sources along with envelope emission by McLean (1979) was shown to compare well with the radiative transfer code of Haisch & Cassinelli (1976). Other such numerical methods investigating the continuum polarisation have been presented by Poeckert & Marlborough (1978), who also investigated line polarisation, Whitney & Code (1989) and Shepherd (1993). In all these cases the single scattering approximation appears to be valid *so long as the envelope is optically thin*. There is some doubt, depending on the author, his/her code and the geometry investigated, as to the optical depth at which single scattering can no longer be applied, but it seems that the approximation is excellent for equatorial optical depths  $\leq 0.1$  and can be used as an upper estimate for depths up to about 1.

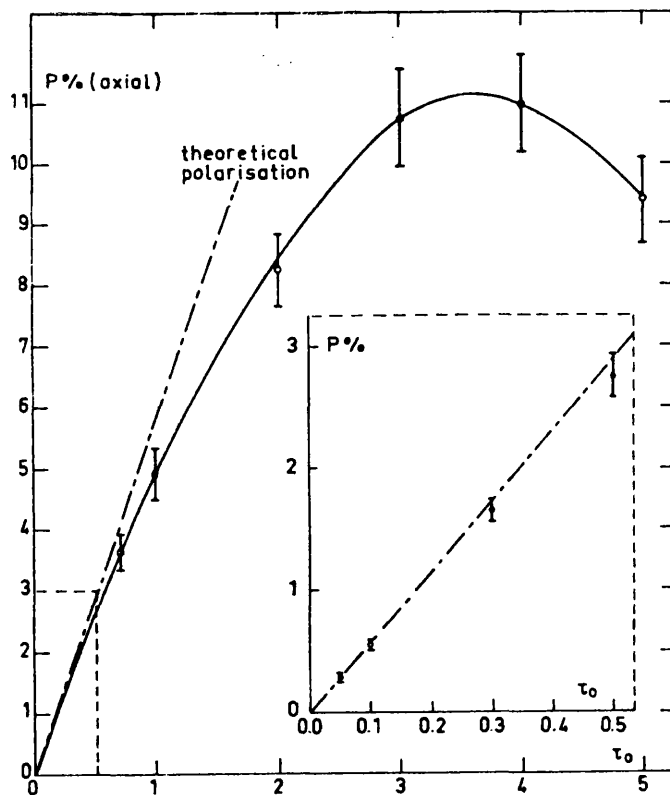


Fig. 1.8 Polarisation as a function of equatorial optical depth for Thomson scattering of stellar radiation in an ellipsoidal envelope – from Daniel (1980). The dashed curve is the result of the Brown & McLean single scattering theory for the geometrical model considered (oblate ellipsoid).

## 1.5 Conclusions

This chapter has introduced the subject of polarised radiation and its role as a diagnostic in astronomy. A detailed treatment of the production of broad band polarisation through Thomson scattering in optically thin circumstellar envelopes of single stars and the regimes in which the approximation is valid has been presented. The above theory predicts the variations of "broad-band" polarisation, but has not been applied in a systematic way as a possible explanation of the observed "narrow-band" wavelength dependent variations of polarisation and position angle across spectral lines. In the following chapters the role of scattering and frequency redistribution, due to the Doppler motions of the scattering electrons, in the production of spectropolarimetric line profiles shall be investigated.

This thesis only considers polarisation arising from single stellar systems and no mention is made of polarisation produced in binary star systems which was studied theoretically by Brown, et al, (1978) and Rudy & Kemp (1978). These papers showed how the inclinations of binary star orbits may be inferred from analysis of the temporal changes of the Stokes  $q$  and  $u$  parameters during an orbital period. Recently the theory presented in these papers has been used extensively by Moffat, et al, (1990).

## 2. Spectropolarimetric line profiles from optically thin Thomson scattering circumstellar discs

### Summary

The beginning of this chapter presents a summary of polarimetric line profile observations and the theoretical explanations which, to date, have been proposed to explain the data. Following on from this summary analysis is presented which describes the formation of spectropolarimetric line profiles due to the Doppler redistribution of stellar radiation Thomson scattered off electrons moving with a bulk velocity in a planar disc. The spectral shape of such spectropolarimetric line profiles contains information on the disc inclination, velocity and density distribution. It is shown that, under certain parametrisations of these distributions, analysis of spectropolarimetric line data yields the disc inclination and most of the other parameters of the system.

### 2.1 Introduction

The previous chapter presented theoretical explanations of observed intrinsic polarisation from single stars in terms of Thomson scattering of stellar radiation in an optically thin circumstellar envelope. These observations and theory applied to "broad band" continuum polarisation variations with wavelength and did not consider high wavelength resolution variations which may occur across spectral lines. As was stated in Sect. 1.3 resonance lines exhibit intrinsic polarisation, but wavelength dependent variations in the polarisation and position angle observed across non-resonance lines (Sect. 2.2) requires a more detailed theory than that presented in Chapter 1 since the Brown & McLean single scattering theory does not allow for such "narrow band" variations. Several authors have investigated these high resolution variations observationally and theoretically and their main findings are presented below.

### 2.2 Observations

While the measurement of continuum stellar polarisation has been widely exploited following Chandrasekhar's predictions in 1946 few attempts were made, until fairly recently, to undertake a systematic observational study of polarisation variations within spectral lines. The apparent inactivity in this field may be attributed to the small polarisation fluctuations predicted (see next sections) and the inability of polarimeters to achieve sufficient accuracy to detect these fluctuations. The first such observational work in this field appears to be that of Ohman (1934) who detected polarisation in the optical  $H_\gamma$  absorption line of  $\beta$  Lyrae.

The advent of more sensitive photoelectric devices in the 1970s heralded a flurry of spectropolarimetric activity initiated by the observations of Clarke & McLean (1973). They measured

around half a dozen early-type stars finding significant polarimetric variations between the continuum and  $H_\beta$ . Poeckert (1975) conducted a survey of the linear polarisation in the  $H_\alpha$  line of 12 Be stars with  $2\text{\AA}$  resolution across the line, providing the impetus behind the theoretical model of the Be star  $\gamma$  Cassiopeiae (see Sect. 2.3). To date, the best data of this type is that of McLean et al (1979) who presented  $H_\alpha$  spectropolarimetric line profiles ( $.5\text{\AA}$  resolution) measured with the now defunct DIGICON polarimeter. More recently Schulte-Ladbeck et al (1991) observed similar polarimetric variations across the He  $4686\text{\AA}$  line in some Wolf-Rayet stars.

The limitations placed on polarimetric spectral resolution by current technologies and also the apparent lack of a simple theoretical explanation of this observed line polarisation seems to have limited the amount of observing time dedicated to such projects. However, the success of the WUPPE mission which detected line polarisation variations in the UV (though only at low spectral resolution) and the advent of high resolution CCD spectropolarimeters has rekindled many researchers interests in this subject – from an observational and theoretical viewpoint.

The following figures give some examples of the high resolution spectropolarimetric data mentioned above.

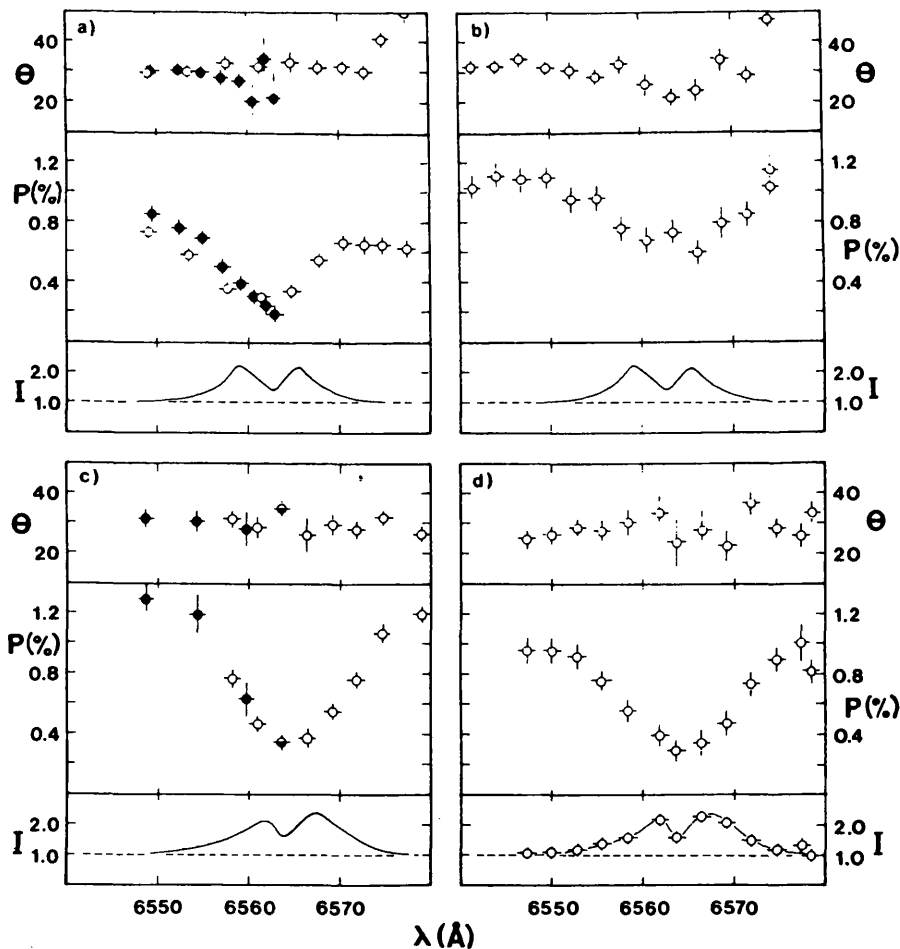


Fig. 2.1 Position angle, percent polarisation and  $H_\alpha$  line profile for  $\zeta$  Tau on four different days. From Poeckert, 1975.

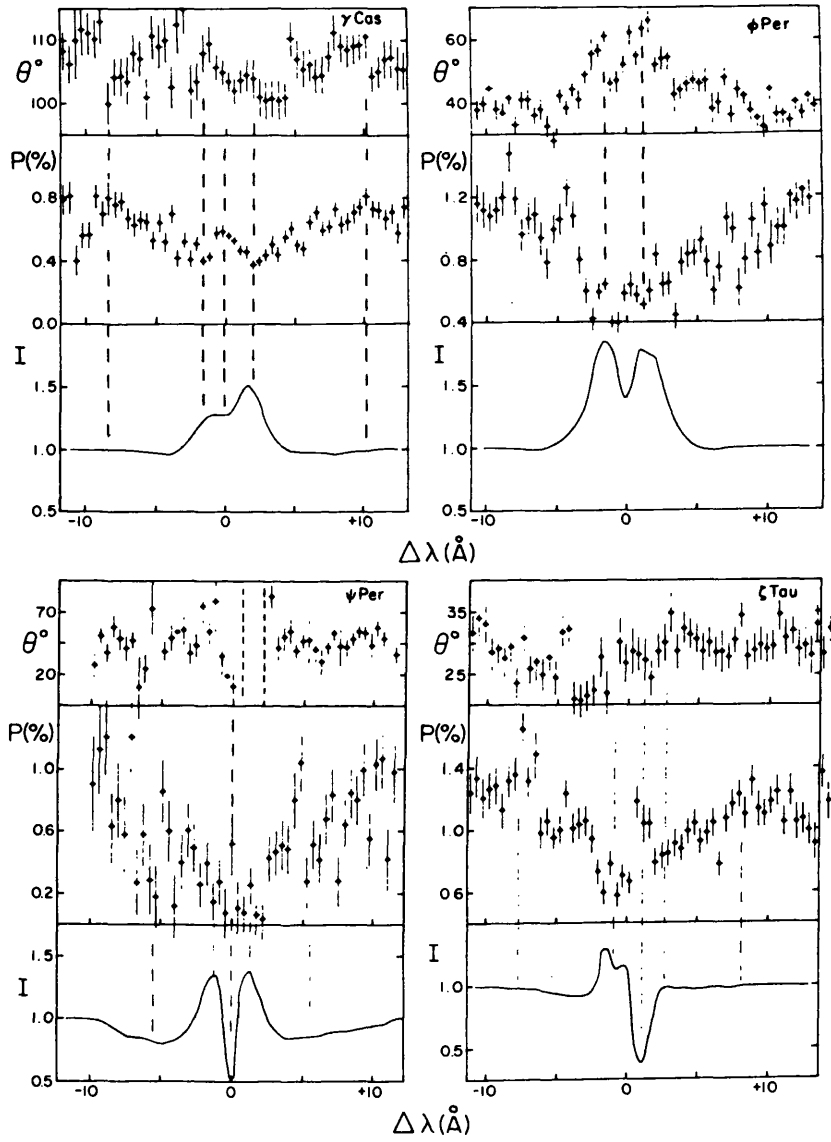
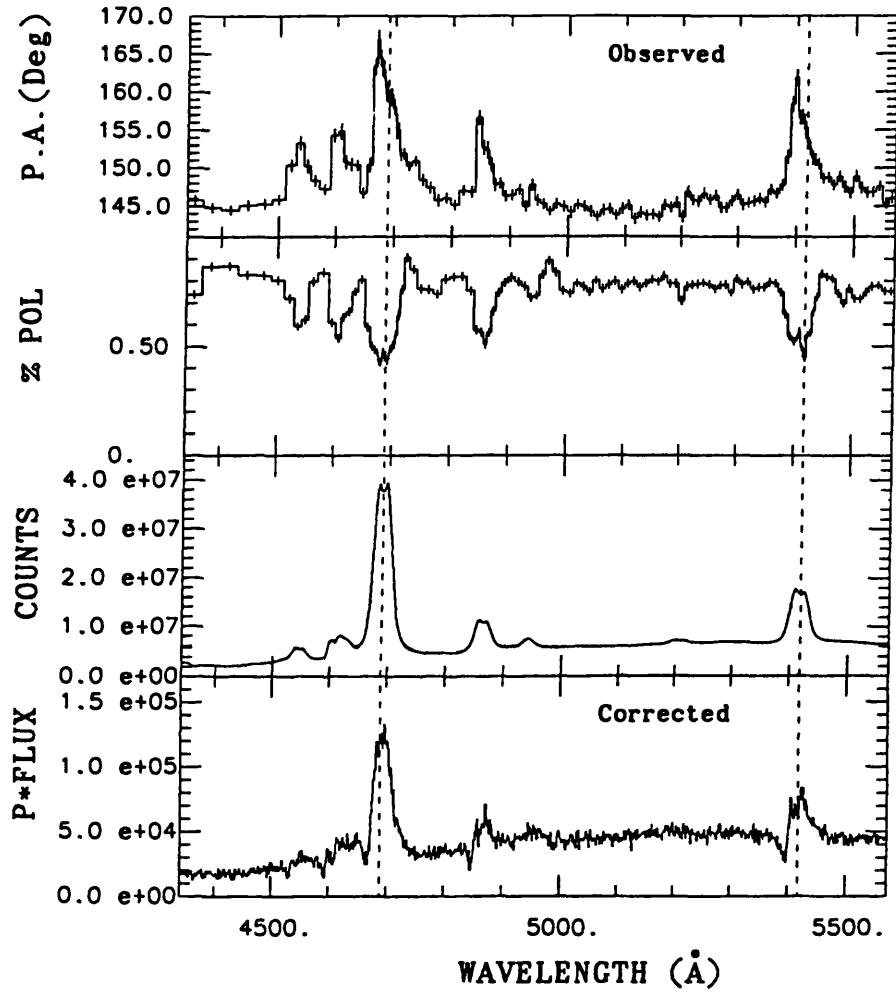


Fig. 2.2 Position angle, percent polarisation and  $H_\beta$  line profile for  $\gamma$  Cas,  $\phi$  Per,  $\psi$  Per and  $\zeta$  Tau obtained with the DIGICON spectropolarimeter by McLean et al, 1979.



**Fig. 2.3** Position angle, percent polarisation and direct flux for the Wolf Rayet star EZ Canis Majoris taken at the Anglo-Australian Telescope by Schulte-Ladbeck et al, 1991.

## 2.3 Theory

This section presents an overview of the theoretical interpretations of spectropolarimetric line data.

### 2.3.1 Polarisation in rotationally broadened spectral lines

Chandrasekhar's (1946) solution of the equation of radiative transfer in a plane parallel electron scattering atmosphere predicted local variations in the degree of polarisation of up to 11% at the stellar limb. In the theory of line formation in moving stellar atmospheres different regions of the stellar atmosphere contribute to different parts of the resulting line profile through the Doppler effect – e.g. the classical P–Cygni profiles are explained by line emission from a radially expanding atmosphere. Ohman (1946) noted that polarimetric line profiles could be formed in a similar fashion due to Doppler effects isolating locally polarised regions of the stellar atmosphere which contribute to different parts of the observed line, thus yielding polarisation variations throughout the Doppler broadened line profile. He illustrated that the integrated polarised flux across a rotationally broadened absorption line from a rotating spherical star is zero, but the Doppler sampling of different regions of the atmosphere breaks the spherical symmetry of the system yielding wavelength dependent polarisation variations within the emergent line profile.

Figure 2.4 illustrates how such a polarimetric profile may arise from a spherical rotating stellar atmosphere in which line emission is occurring. The line strength observed at different wavelengths is proportional to the “size” of the region contributing to the emission at that wavelength due to the Doppler sampling described above. Region 1 contributes to the emission at line centre since these parts of the star have little or no radial velocity with respect to the observer, while the extreme edges of the star (regions 2) have the largest radial velocity due to stellar rotation and so this emission is Doppler shifted into the line wings. Region 1 is larger than region 2 resulting in a larger contribution to the flux at line centre than in the wings, hence the observed emission line profile. Qualitatively following Chandrasekhar's work, the emergent radiation at the stellar limb will be polarised with the local polarisation vector being perpendicular to a radial line from the star centre – as described in Sect 1.4 – thus summing these polarisation vectors over regions 2 will yield a net polarisation vector parallel to the stellar rotation axis while the net polarisation vector from region 1 will be perpendicular to this axis. Adopting the usual convention that directions parallel to the stellar rotation axis represent positive polarisation then the wavelength dependence of the polarisation in the line will be such that it is negative at line centre and positive in the wings as illustrated.

Collins & Cranmer (1992) presented a quantitative analysis of this effect for UV absorption lines, predicting variations in the level of polarisation up to about .5% across the broadened line – Fig. 2.5. For this case of a pure absorption line the spectral shape of the polarisation is the negative to that of the pure emission line – i.e. positive polarisation at line centre and negative in

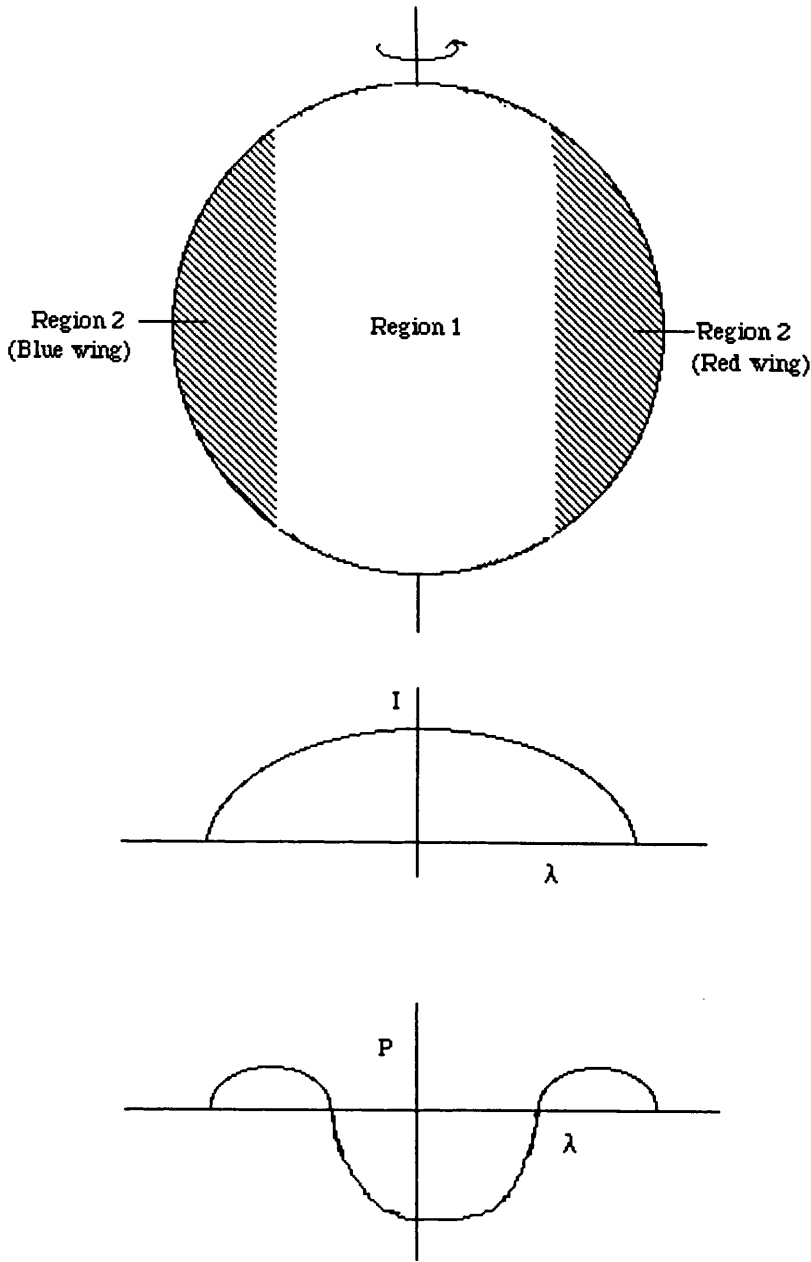


**Fig. 2.4** The production of a spectropolarimetric line profile through scattering in a rotating stellar atmosphere.

the wings. This arises due to absorption of the negative polarised flux from region 1 in Fig. 2.4 leaving a net positive polarisation at line centre while the positive polarised flux is absorbed from region 2 yielding a net negative polarisation in the line wings.

It is to be noted that this Doppler sampling effect will not give rise to polarisation in lines formed in a spherically expanding star since the regions on the projected stellar disc which contribute to each wavelength in the Doppler broadened line are concentric rings and thus there will be total cancellation of the polarisation vectors around each ring yielding zero polarisation at each

wavelength in the broadened line. However, the combination of rotation and expansion within the spherical envelope *will* break the spherical symmetry of the system yielding a more complex polarimetric line profile incorporating position angle changes also due to the non-spherical shape of the isovelocity regions in the envelope.

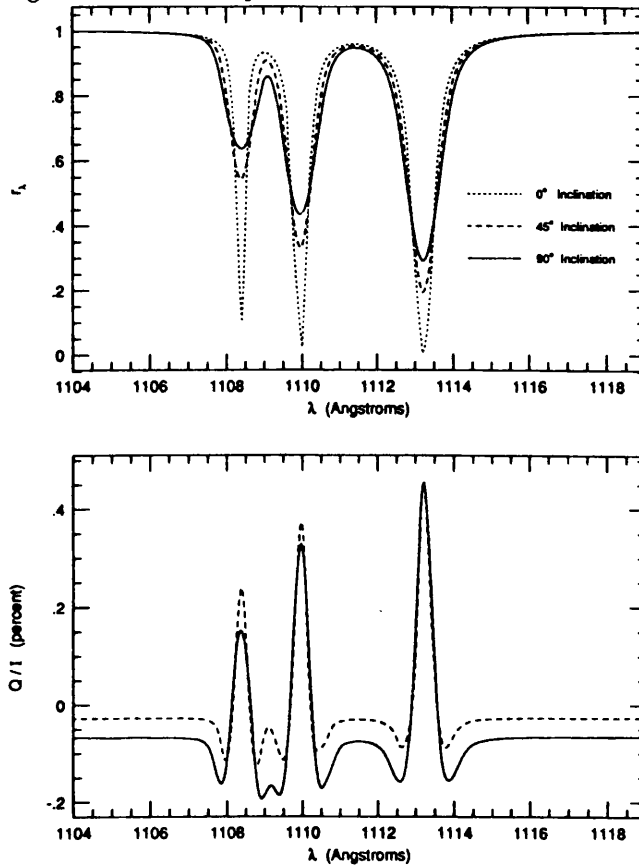


Fig. 2.5 Collins & Cranmer's spectropolarimetric absorption line profiles formed in a rotating star at various inclinations to the line of sight.

### 2.3.2 Optical depth effects in a moving circumstellar envelope

Numerical modelling efforts by Poekert & Marlborough (1978) to explain the observed  $H_\alpha$  spectropolarimetric line profile in the Be star  $\gamma$  Cassiopeiae led them to propose that the polarisation variations across the line were due to Thomson scattering of continuum stellar radiation in a moving flattened circumstellar envelope containing  $H_\alpha$  line opacity. The Doppler motion of the absorbers, through the bulk motion of the envelope, has a wavelength-shifting effect on the line opacity thus allowing an observer to "see" deeper into the approaching (or receding) regions of the envelope at a given wavelength - i.e. the physical depth at which the envelope optical depth is unity (say) varies with observed wavelength and also (through the Doppler effect) the radial speed of the envelope region. This results in different spatial integrations over the scattered continuum radiation from the central star at each wavelength and thus a wavelength dependence of the polarisation (and possibly position angle) across the line. These effects were also predicted in a qualitative manner by McLean (1979). The results of Poekert & Marlborough's model calculations are shown in Fig. 2.6.

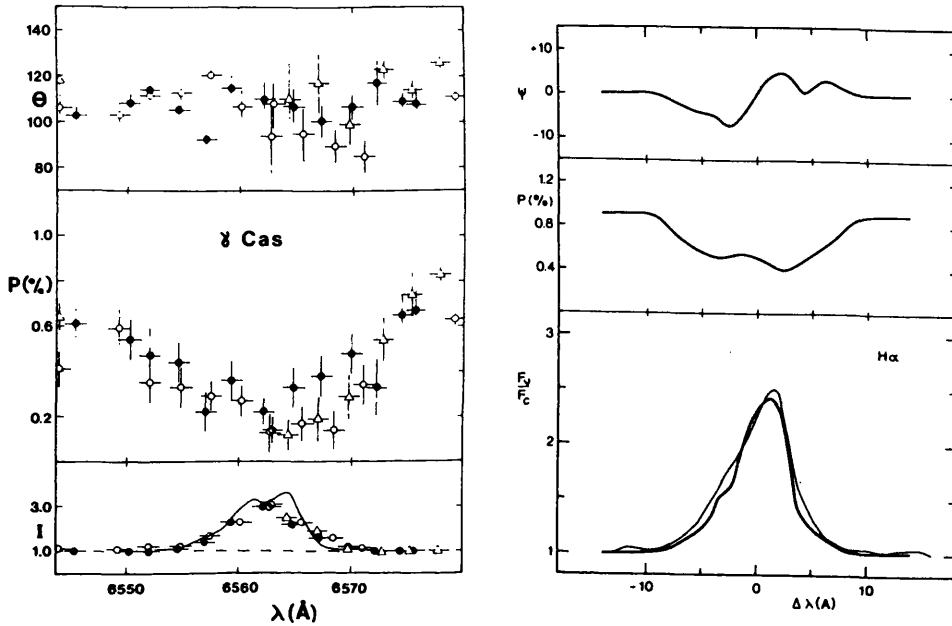


Fig. 2.6 Poekert & Marlborough's  $\gamma$  Cassiopeiae data and model results.

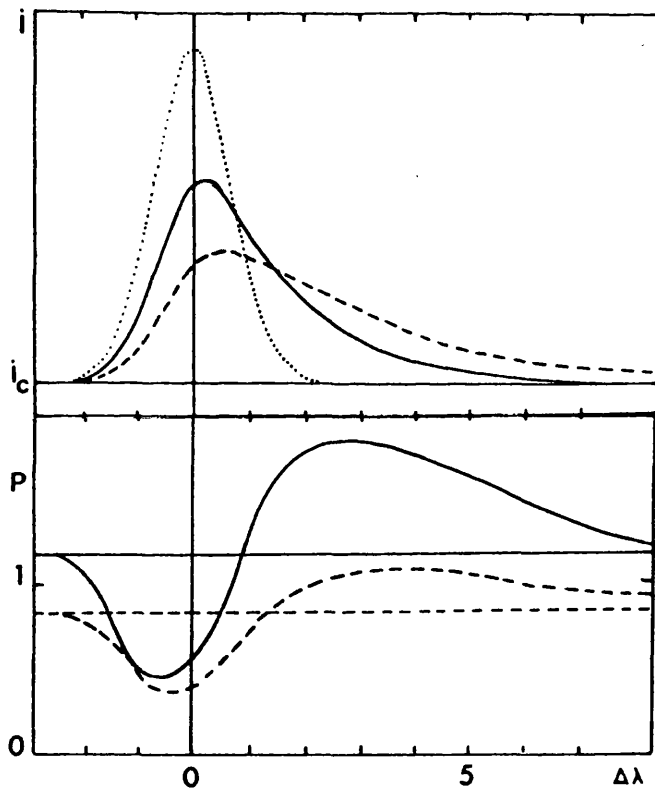


Fig. 2.7 Lefevre's spectropolarimetric line profiles arising from scattering stellar line radiation in an expanding atmosphere. The curves are for different envelope optical depths in electron scattering.

### 2.2.3 Line scattering in an expanding envelope

Monte Carlo calculations by Van Blerkom and Van Blerkom (1978) and Romanik and Leung (1981) showed that the scattering of light in an expanding dust shell has the effect of redshifting the entire

intensity profile of spectral features. Lefevre (1992) also applied a Monte Carlo simulation to dust and Rayleigh scattering in a spherical expanding envelope and obtained similar redshifts. Lefevre's introduction of source anisotropy in the form of a photospheric hot spot broke the spherical symmetry of the model and his simulation was extended to include spectropolarimetric line profiles – Fig. 2.7.

The remainder of this chapter considers the problem of Thomson scattering of a stellar line in a moving envelope. It is simpler than the earlier work cited above in treating only single scattering but much more general in so far as this simplification brings out clearly how different regions of a moving circumstellar disc contribute to the features in scattered spectropolarimetric line profiles.

#### 2.4 Effects of electron bulk velocity on scattered line profiles

In Chapter 1 when calculating the polarisation arising from Thomson scattering in circumstellar envelopes the scattering electrons were assumed to be stationary and hence there was no frequency redistribution of the scattered radiation. When applying the single scattering theory to the scattering of continuum radiation, as will be shown in Chapter 4, this turns out to be a reasonable assumption since the Doppler redistribution due to electron motion in stellar envelopes is small compared to the scale on which the continuum varies with wavelength, such that there is little effect on the shape of scattered broad-band features. However, when dealing with the scattering of line radiation this Doppler redistribution must be included since the width of spectral lines is often comparable to or less than the wavelength shifts resulting from the Doppler motions of the scattering electrons.

The bulk velocity of the electrons results in a frequency redistribution of scattered radiation through the effect of *two* Doppler shifts which arise due to the electron's radial velocity with respect to the source, for incident photons, and with respect to the observer for scattered photons. These two effects manifest themselves in the following way. Radiation emitted by the source at frequency  $\nu_*$  is seen and subsequently scattered by the electron at frequency  $\nu_e$  which is given by  $\nu_e = \gamma(1 - \beta \cdot \hat{\mathbf{k}}_*)\nu_*$  in the electron's rest frame. Due to the electron's motion with respect to the observer this scattered frequency appears to the observer as  $\nu = \nu_e/\gamma(1 - \beta \cdot \hat{\mathbf{k}})$ , where it is assumed that the primary source is fixed relative to the observer. The frequency which the observer sees is then related to the original emitted frequency,  $\nu_*$ , by,

$$\nu = \left( \frac{1 - \beta \cdot \hat{\mathbf{k}}_*}{1 - \beta \cdot \hat{\mathbf{k}}} \right) \nu_* , \quad (2.1)$$

where  $\hat{\mathbf{k}}_*$  and  $\hat{\mathbf{k}}$  are as shown in Fig. 1.1,  $\beta c$  is the electron velocity ( $c$  being the speed of light) and  $\gamma = \sqrt{1 - \beta^2}$ . The frequency part of the redistribution function is still given by Eq. 1.12, but the scattered frequency appearing in the delta function is now given by Eq. 2.1. The scattered Stokes fluxes are then determined by Eq. 1.22 noting the relation between the incident and observed frequencies. The above equations apply to both bulk and random (Maxwellian) velocities

– cf Chapter 4. As far as the electron bulk velocity is concerned, if this varies throughout the circumstellar envelope then scattering from different regions will result in differing Doppler redistributions in accordance with Eq. 2.1, such that the frequency dependence of the scattered fluxes could, potentially, take quite complex forms. The total scattered Stokes fluxes are determined at a given wavelength shift by summing the locally scattered fluxes, weighted by the scatterer density, at each point on the *isowavelength-shift surfaces* or *contours*. Along these surfaces the observed relative wavelength shift, with respect to the wavelength emitted by the source, is constant. From Eq. 2.1 the isowavelength-shift surfaces are given by the condition,

$$\frac{\lambda - \lambda_\star}{\lambda_\star} = \left( \frac{1 - \beta \cdot \hat{\mathbf{k}}_\star}{1 - \beta \cdot \hat{\mathbf{k}}} \right) - 1. \quad (2.2)$$

Now that a frequency redistribution has been introduced care must be taken when calculating the normalised Stokes parameters, Eqs. 1.24 and 1.25, since the scattered  $I$  flux may not be small compared to  $F_\nu^D$  at all frequencies. For the scattering of continuum radiation, as stated in Chapter 1, Eq. 1.25 is always valid for envelopes of small scattering optical depth, but for the scattering of pure line radiation (in the absence of any continuum) this is invalid outside the line core, where scattered radiation is the only flux. However, when a continuum is present, as is usually the case, the approximation is again valid except for very strong lines whose specific intensity at line centre is comparable with or many times the continuum level. In this case any frequency redistribution of the scattered flux may result in photons from close to line centre being scattered into the local continuum, such that even after being reduced by the scattering optical depth their scattered flux is comparable to the direct continuum flux at that frequency.

The effect of a finite source exhibiting limb darkening or any source anisotropy, such as a hot spot or rotational distortion, may be incorporated in the integral over all incident light rays,  $d\Omega_\star$ , in Eq. 1.22. In general a finite source serves only to reduce the magnitude of the Stokes fluxes  $F_\nu^Q$  and  $F_\nu^U$  (Brown et al. 1989). This will reduce the magnitude of the polarisation, but will not affect the variations in position angle (nor the relative changes in polarisation) with wavelength (provided Doppler shifts arising from *stellar* rotation, which would vary across the stellar disc, are neglected) since this involves the ratio of the Stokes  $Q$  and  $U$  parameters. For ease of calculation this finite source correction is neglected in this analysis. However, in Section 2.6 the effects of occultation of the scattering material by the star *are* included since they have a crucial symmetry-breaking effect, as will be shown.

The Stokes fluxes arising from scattering of radiation from a point source in a planar disc are obtained from Eq. 1.29 with  $\theta = \pi/2$  thus,

$$\begin{Bmatrix} F_\nu^I(\nu) \\ F_\nu^Q(\nu) \\ F_\nu^U(\nu) \end{Bmatrix} = \frac{3\sigma_T R^2}{32D^2} \int I_{\nu_\star}(\nu_\star) \frac{\Sigma(r)}{r} \begin{Bmatrix} 2(1 + \sin^2 i \cos^2 \phi) \\ \sin^2 i - (1 + \cos^2 i) \cos 2\phi \\ 2 \cos i \sin 2\phi \end{Bmatrix} dr d\phi, \quad (2.3)$$

where  $\Sigma(r)$  is the electron surface number density on the disc and  $\nu_*$  is given by Eq. 2.1.

In general the specific intensity from the source will consist of a line profile, which varies rapidly with wavelength, superposed on a continuum which may be considered to be independent of wavelength in the vicinity of the line. This may be represented as,

$$I_{\nu_*}(\nu_*) = I^C + I_{\nu_*}^L(\nu_*), \quad (2.4)$$

where  $I^C$  is the continuum specific intensity, assumed flat, and  $I_{\nu_*}^L(\nu_*)$  is the line profile. When this form is inserted into Eq. 2.3 the equation splits into two parts – a constant continuum (as derived in Chapter 1) plus a wavelength dependent spectropolarimetric line profile. In the subsequent analysis it is assumed that the continuum terms (being wavelength independent) and any interstellar component can be removed from any data and the remaining scattered spectropolarimetric line profile shall be analysed.

For scattering in a planar disc at inclination  $i$  to the observer Eq. 2.1 becomes,

$$\nu = \left( \frac{1 - \beta_r(r)}{1 - \beta_r(r) \sin i \cos \phi + \beta_\phi(r) \sin i \sin \phi} \right) \nu_*, \quad (2.5)$$

where  $\beta_r(r)c$  and  $\beta_\phi(r)c$  are the expansion and rotation velocities which are assumed only to be a function of the radial distance,  $r$ , in the disc. Assuming a form for the frequency dependence of the initial radiation and for the velocity field of the disc, the resultant Stokes fluxes may then be calculated from Eq. 2.3.

## 2.5 Scattering of monochromatic radiation

The simplest form for the incident radiation field, which also illustrates clearly how the velocity field of the disc determines the scattered line profile, is that of a monochromatic line, centred at frequency  $\nu_0$ , given by,

$$I_{\nu_*}(\nu_*) = I_0 \delta(\nu_* - \nu_0). \quad (2.6)$$

This form also considerably simplifies Eq. 2.3 due to the following property of the delta function,

$$\delta[f(z)] = \frac{\delta(z - z_0)}{|f'(z_0)|}, \quad (2.7)$$

which is summed over all values of  $z_0$  satisfying  $f(z_0) = 0$ . Inserting Eq. 2.5 into Eq. 2.6 and noting Eq. 2.7, then yields,

$$I_{\nu_*}(\nu_*) = I_0 \delta(\nu_* - \nu_0) = I_0 \frac{\delta(\phi - \phi_0)}{|f'(\phi_0)|}, \quad (2.8)$$

where, with  $x = r/R$  the dimensionless radial distance, the  $f$  function is,

$$\nu_* - \nu_0 = f(\nu, \nu_0, x, \phi, i) = \left( \frac{1 - \beta_r(x) \sin i \cos \phi + \beta_\phi(x) \sin i \sin \phi}{1 - \beta_r(x)} \right) \nu - \nu_0. \quad (2.9)$$

Setting  $f(\phi_0) = 0$  then gives,

$$\phi_0 = \cos^{-1} \left( \frac{\beta_r(x) - \alpha[1 - \beta_r(x)]}{\sqrt{\beta_r(x)^2 + \beta_\phi(x)^2} \sin i} \right) - \tan^{-1} \left( \frac{\beta_\phi(x)}{\beta_r(x)} \right), \quad (2.10)$$

where the dimensionless wavelength shift from line centre,  $\lambda_0$ , is given by,

$$\alpha = \frac{\lambda - \lambda_0}{\lambda_0}. \quad (2.11)$$

Equation 2.3 now becomes,

$$\begin{aligned} \left\{ \begin{array}{l} \nu F_\nu^I(\alpha) \\ \nu F_\nu^Q(\alpha) \\ \nu F_\nu^U(\alpha) \end{array} \right\} &= \sigma_0 F_0 \int \left| \frac{1 - \beta_r(x)}{\beta_r(x) \sin i \sin \phi_0 + \beta_\phi(x) \sin i \cos \phi_0} \right| \frac{\Sigma(x)}{x} \\ &\times \left\{ \begin{array}{l} 2(1 + \sin^2 i \cos^2 \phi_0) \\ \sin^2 i - (1 + \cos^2 i) \cos 2\phi_0 \\ 2 \cos i \sin 2\phi_0 \end{array} \right\} dx, \end{aligned} \quad (2.12)$$

where,

$$\sigma_0 = \frac{3}{32} \sigma_T, \quad F_0 = \frac{R^2}{D^2} I_0. \quad (2.13)$$

The Stokes fluxes are given by the summation of the results of the integral on the right hand side of Eq. 2.12 calculated at all values of  $\phi_0$  given by Eq. 2.10 with the range of  $\alpha$  determined from the maximum and minimum values allowed by Eq. 2.10. Outwith this  $\alpha$ -range there is no scattered flux since there are no scattering electrons with a large enough velocity to give the required Doppler shifts. The limits of integration are the minimum and maximum  $x$  values allowed by Eq. 2.10, with  $x \geq 1$  (stellar surface) in any case. Performing the two-dimensional integral over the disc area is equivalent to integrating along the isowavelength-shift contours since, for a given  $\alpha$ , each value of  $x$  "picks out" a  $\phi_0$  due to the delta function. Integrating over  $x$ , and hence  $\phi$ , for a given  $\alpha$  is then equivalent to summing the scattered Stokes fluxes, weighted by the electron number density, along that isowavelength-shift contour as described above.

Equation 2.12 is an integral equation which may be inverted to yield information on the velocity field and density structure of the disc in terms of the scattered Stokes fluxes, further discussion of which is left until Chapter 3. For now the resultant scattered spectropolarimetric line profiles arising from particular forms of the disc velocity and density structures and the information available from analysis of such data are investigated.

### 2.5.1 Pure disc rotation

For pure disc rotation  $\beta_r(x) = 0$  and Eq. 2.10 reduces to,

$$\phi_0 = \sin^{-1} \left( \frac{\alpha}{\beta_\phi(x) \sin i} \right), \quad \pi - \sin^{-1} \left( \frac{\alpha}{\beta_\phi(x) \sin i} \right). \quad (2.14)$$

Substituting these forms for  $\phi_0$  into the integrals on the right hand side of Eq. 2.12 and summing over the individual results, as demanded by Eq. 2.7, yields,

$$\begin{Bmatrix} \nu F_\nu^I(\alpha) \\ \nu F_\nu^Q(\alpha) \\ \nu F_\nu^U(\alpha) \end{Bmatrix} = 4\sigma_0 F_0 \begin{Bmatrix} I_1(\alpha) + \sin^2 i I_2(\alpha) \\ I_1(\alpha) - (1 + \cos^2 i) I_2(\alpha) \\ 0 \end{Bmatrix}, \quad (2.15)$$

where the integral functions  $I_1(\alpha)$  and  $I_2(\alpha)$  are given by,

$$\begin{Bmatrix} I_1(\alpha) \\ I_2(\alpha) \end{Bmatrix} = \int \frac{\Sigma(x)}{x \beta_\phi(x) \sin i} \begin{Bmatrix} \left[ 1 - \left( \frac{\alpha}{\beta_\phi(x) \sin i} \right)^2 \right]^{-\frac{1}{2}} \\ \left[ 1 - \left( \frac{\alpha}{\beta_\phi(x) \sin i} \right)^2 \right]^{\frac{1}{2}} \end{Bmatrix} dx, \quad (2.16)$$

where the limits on the  $x$ -integral are the maximum and minimum positive  $x$  values allowed by  $\beta(x) = \alpha / \sin i$ .

The general inversion procedure to determine  $\beta_\phi(x)$  and  $\Sigma(x)$  will be discussed in Chapter 3. For now attention will be focussed on the spectropolarimetric profiles arising when the disc velocity and density profiles can be parameterised by the simple power law distributions,

$$\beta_\phi(x) = \beta_0 x^{-p} \quad \Sigma(x) = \Sigma_0 x^{-q}, \quad (2.17)$$

where  $\beta_0$  and  $\Sigma_0$  are the velocity and density values at the star-disc boundary. This parameterisation includes Keplerian rotation ( $p = 1/2$ ) and viscous discs ( $p = 1$ ), while  $q$  can be determined from the continuity equation for a steady slowly expanding planar disc ( $q = 1$ ). Assuming this parameterisation the integral functions become,

$$\begin{Bmatrix} I_1(\alpha) \\ I_2(\alpha) \end{Bmatrix} = \frac{\Sigma_0}{\beta_0 \sin i} \int_1^{\left(\frac{\beta_0 \sin i}{\alpha}\right)^{\frac{1}{p}}} x^{p-q-1} \begin{Bmatrix} \left[ 1 - \left( \frac{\alpha}{\beta_0 \sin i} \right)^2 x^{2p} \right]^{-\frac{1}{2}} \\ \left[ 1 - \left( \frac{\alpha}{\beta_0 \sin i} \right)^2 x^{2p} \right]^{\frac{1}{2}} \end{Bmatrix} dx. \quad (2.18)$$

On making the substitution  $y = (\alpha / \beta_0 \sin i)^2 x^{2p}$  these integrals reduce to,

$$\begin{Bmatrix} I_1(\alpha) \\ I_2(\alpha) \end{Bmatrix} = \frac{\Sigma_0}{2p\beta_0 \sin i} \left( \frac{\alpha}{\beta_0 \sin i} \right)^{\frac{q-p}{p}} \begin{Bmatrix} B\left(\frac{p-q}{2p}, \frac{1}{2}\right) - B_{\left(\frac{\alpha}{\beta_0 \sin i}\right)^2} \left(\frac{p-q}{2p}, \frac{1}{2}\right) \\ B\left(\frac{p-q}{2p}, \frac{3}{2}\right) - B_{\left(\frac{\alpha}{\beta_0 \sin i}\right)^2} \left(\frac{p-q}{2p}, \frac{3}{2}\right) \end{Bmatrix}, \quad (2.19)$$

where the complete and incomplete Beta functions are defined as,

$$B(a, b) = \int_0^1 t^{a-1} (1-t)^{b-1} dt, \quad B_c(a, b) = \int_0^c t^{a-1} (1-t)^{b-1} dt. \quad (2.20)$$

From the above it is clear that the spectral *shape* of the spectropolarimetric line profile is determined by the ratio of the indices  $p$  and  $q$ , while its *width* is determined by  $\alpha = \beta_0 \sin i$ , since there are no electrons moving fast enough to give the Doppler shift required to scatter the incident

radiation beyond this  $\alpha$  value. If this parametrisation of the disc velocity and density is valid then it should be possible to determine most of the physical parameters pertaining to the disc from analysis of spectropolarimetric line data which has been processed to remove the continuum flux and interstellar polarisation, in the following way.

When  $\alpha$  is small (i.e. close to the centre of the scattered line, but outwith the stellar line) the integrals in Eq. 2.18 are asymptotically equal so that the ratio of the scattered  $Q$  and  $I$  fluxes there will yield the disc inclination from the solution of

$$\frac{F_{\nu}^Q(\alpha \approx 0)}{F_{\nu}^I(\alpha \approx 0)} = \frac{-\cos^2 i}{1 + \sin^2 i} \quad (2.21)$$

The negative sign appears on the right hand side of this equation because the scattered  $Q$  flux is negative along isowavelength-shift contours of small wavelength shift, as will be explained below. The fact that  $i$  can be determined results from the fact that use of a scattered spectral line profile, as opposed to broad-band measurements – cf Brown & McLean (1977), allows different parts of the disc to be picked out. Setting  $\alpha \approx 0$  picks out the isowavelength-shift contour elements at  $\phi = 0, \pi$  where the scattering angles are  $\pi/2 + i$  and  $\pi/2 - i$ , giving different values of the scattered total to polarised fluxes – Section 2.7 and Chapter 3 describe a more robust method for determining  $i$  from spectropolarimetric line data.

The parameter  $\beta_0$  is then obtained from the maximum wavelength shift of the scattered flux profiles ( $\alpha_{\max} = \beta_0 \sin i$ ) using the inclination value determined from Eq. 2.21.

The final parameter which may be obtained from this analysis is the  $q/p$  index ratio, which governs the spectral shape of the scattered flux profiles, and is determined from a best fit to either the scattered  $F_{\nu}^I(\alpha)$  or  $F_{\nu}^Q(\alpha)$  flux data (or in principle by the ratios of these fluxes at two  $\alpha$  values).

This illustrates the power of spectropolarimetric line profile analysis in determining disc parameters, in particular the determination of disc inclinations which cannot be derived from continuum spectropolarimetry since it is not possible to separate out the scattered  $I$  flux from the direct flux (Brown & McLean, 1977). Note, however, that if *stellar* rotation – neglected in this analysis – is important it may not be possible to separate the scattered and direct fluxes since any monochromatic stellar line could be broadened by up to  $\beta_0 \sin i$ . In such cases it should be possible to determine the parameters  $\beta_0 \sin i$  and  $q/p$  from analysis of the scattered  $Q$  flux.

### Illustrative example

For illustrative purposes the resultant scattered Stokes fluxes for the case of  $p = 1/2$  (Keplerian rotation),  $q = 1$  are presented in Fig. 2.8. These profiles are explained with reference to Fig. 2.9 which shows isowavelength-shift contours for a disc rotating with the above velocity profile,

at an inclination of  $60^\circ$  and also the projection upon the sky of the direction of vibration of the local polarisation vector for different disc regions. The positive  $Q$  axis for the entire system is also shown, being the projection on the sky of the disc rotational axis. This choice of axis results in an inclination dependence on the scattering angle such that  $\cos \Theta = \sin i \cos \phi$  where  $\phi$  is the azimuthal angle on the disc. This shows that the observed wavelength will be red-shifted, with respect to the wavelength emitted by the source, for  $0 < \phi < \pi$  (the right half of the disc) and blue-shifted for  $\pi < \phi < 2\pi$  (the left half of the disc). At the centre of the scattered line ( $\alpha = 0$  contour), where  $\phi = 0$  or  $180^\circ$ , the scattering phase function for the  $I$  flux is at its maximum value, due to the  $1 + \cos^2 \Theta$  dependence of the Rayleigh angular phase function. Moving away from line centre the phase function along the contours decreases, reaching its minimum value at  $\phi = 90^\circ$ . For the particular velocity and density distributions chosen the  $I$  flux is maximum at line centre and decreases to zero at  $|\alpha| = \beta_0 \sin i$ , beyond which value there is no scattered flux. Due to the symmetry between the front and rear halves of the disc the  $U$  component of the scattered flux cancels on summation over each contour, hence the position angle is constant across the line. At line centre the  $Q$  flux is negative, as is evident from the scattered polarisation direction along this contour. Moving away from line centre, more positive  $Q$  contributions from the density weighted contours raise the  $Q$  flux to a maximum positive value, beyond which the shape of the contours yield more negative contributions, thus reducing the  $Q$  flux to zero at  $|\alpha| = \beta_0 \sin i$ .

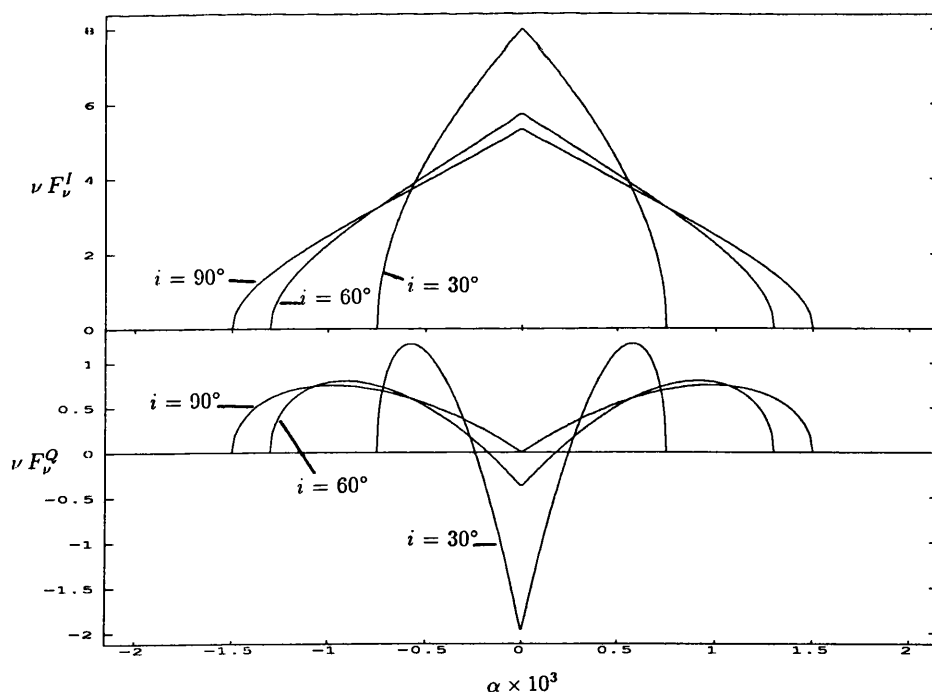


**Fig. 2.8** The resulting Stokes fluxes after scattering monochromatic stellar line radiation in a Keplerian rotating disc whose velocity at the stellar surface is  $450 \text{ km.s}^{-1}$ .

It should be noted that these profiles will not take the same spectral shape for all velocity and density distributions since the scattered fluxes at each  $\alpha$  are proportional to the “length” of the  $\alpha$ -contour weighted by the density value at each point along it. However, as was described in the

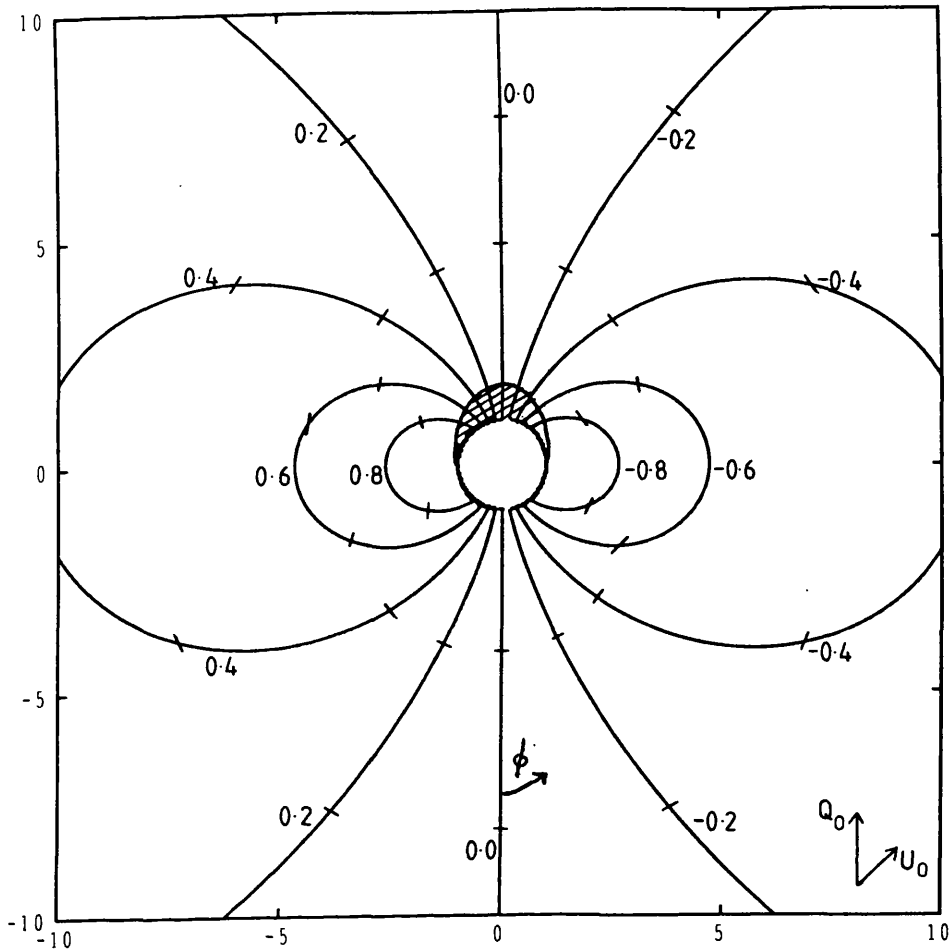


**Fig. 2.9** Isowavelength-shift contours,  $(\lambda - \lambda_*)/\lambda_* \times 10^3 = \text{Constant}$ , on a Keplerian rotating disc viewed by an observer inclined at  $60^\circ$  to the rotation ( $z$ ) axis and positioned at infinity in the plane containing  $\phi = 0$ . The hatched region is the area of the disc occulted by the star (see Section 2.6). The axes are labelled in units of stellar radii. The short bars are the projections upon the sky of the direction of vibration of the local polarisation vector for different disc regions. The positive Stokes  $Q$  and  $U$  directions chosen for the entire system are also shown,  $(Q_0, U_0)$ .

discussion following Eq. 2.20, systems which have the same  $q/p$  ratio *will* have the same spectral shape.

### 2.5.2 Pure disc expansion

In this case of pure expansion Eq. 2.10 reduces to,

$$\phi_0 = \cos^{-1} \left( \frac{\beta_r(x) - \alpha[1 - \beta_r(x)]}{\beta_r(x) \sin i} \right), \quad 2\pi - \cos^{-1} \left( \frac{\beta_r(x) - \alpha[1 - \beta_r(x)]}{\beta_r(x) \sin i} \right). \quad (2.22)$$

The Stokes fluxes are then given by Eq. 2.12 as,

$$\begin{Bmatrix} \nu F_\nu^I(\alpha) \\ \nu F_\nu^Q(\alpha) \\ \nu F_\nu^U(\alpha) \end{Bmatrix} = 2\sigma_0 F_0 \begin{Bmatrix} I_3(\alpha) + \sin^2 i I_4(\alpha) \\ I_3(\alpha) - (1 + \cos^2 i) I_4(\alpha) \\ 0 \end{Bmatrix}, \quad (2.23)$$

where the integrals  $I_3(\alpha)$  and  $I_4(\alpha)$  are,

$$\left\{ \begin{array}{l} I_3(\alpha) \\ I_4(\alpha) \end{array} \right\} = \int \frac{\Sigma(x)[1 - \beta_r(x)]}{x\beta_r(x)\sin i \sqrt{1 - \left(\frac{\alpha[1 - \beta_r(x)] - \beta_r(x)}{\beta_r(x)\sin i}\right)^2}} \left\{ \begin{array}{l} 1 \\ \left(\frac{\alpha[1 - \beta_r(x)] - \beta_r(x)}{\beta_r(x)\sin i}\right)^2 \end{array} \right\} dx. \quad (2.24)$$

The upper and lower limits on these integrals are determined from the maximum and minimum  $x$  values permitted by Eq. 2.22.

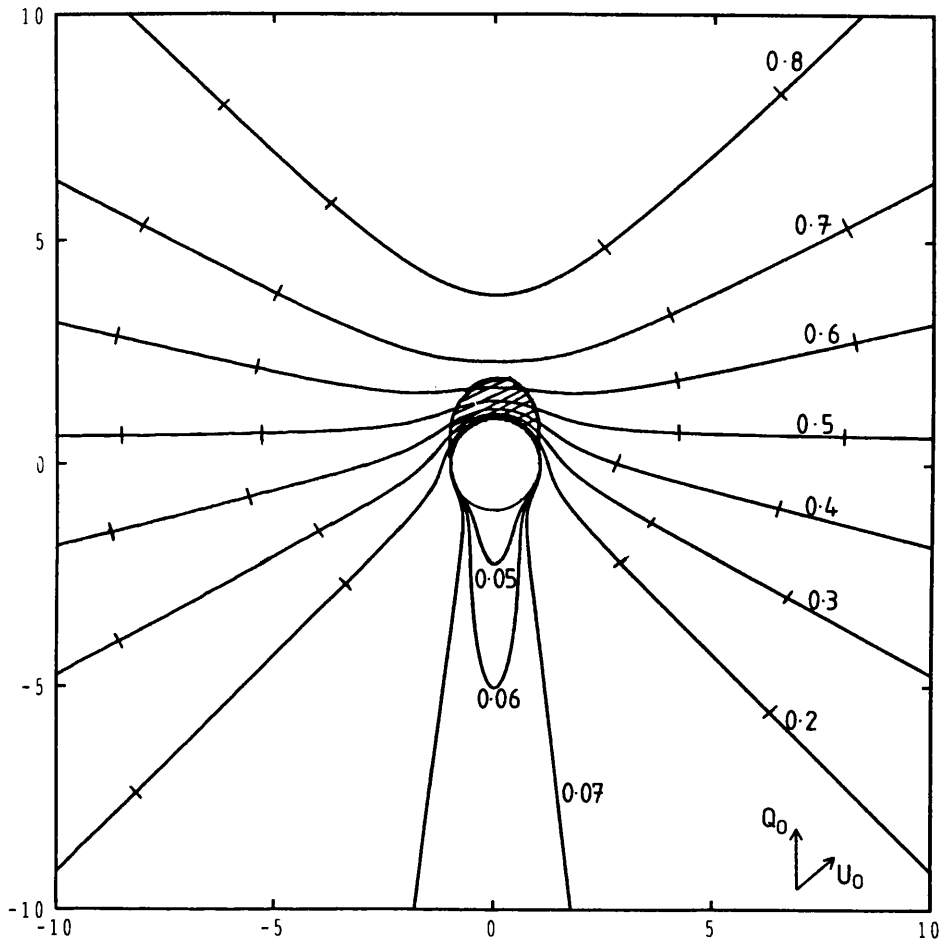


**Fig. 2.10** As for Fig. 2.9 except for an expanding disc with velocity profile  $v(x) = v_\infty(1 - 1/x)^{1/2}$ .

A monotonic decreasing parametrisation of the disc expansion velocity similar to that in the previous section (i.e. decelerating outflow) is not valid since stellar winds generally accelerate outward (e.g. Castor et al, 1975). The wind velocity law often adopted for modelling purposes is the following,

$$\beta(x) = \beta_\infty(1 - 1/x)^\gamma, \quad (2.25)$$

where the size of the effective acceleration region depends on  $\gamma$ . Adopting this velocity profile allows the integration limits for Eq. 2.24 to be determined from Eq. 2.22. Noting that  $1 - \beta_r(x) \approx 1$ , since typical stellar wind speeds are such that  $\beta_r \ll 1$ , the integral limits for  $0 \leq \alpha \leq \beta_\infty(1 - \sin i)$

are,

$$x_{\min} = \frac{1}{1 - \left[ \frac{\alpha}{\beta_{\infty}(1+\sin i)} \right]^{\frac{1}{\gamma}}}, \quad x_{\max} = \frac{1}{1 - \left[ \frac{\alpha}{\beta_{\infty}(1-\sin i)} \right]^{\frac{1}{\gamma}}}, \quad (2.26)$$

while for  $\alpha$  in the range  $\beta_{\infty}(1 - \sin i) \leq \alpha \leq \beta_{\infty}(1 + \sin i)$  the limits are,

$$x_{\min} = \frac{1}{1 - \left[ \frac{\alpha}{\beta_{\infty}(1+\sin i)} \right]^{\frac{1}{\gamma}}}, \quad x_{\max} = \infty. \quad (2.27)$$

These two domains for the limits on  $x$  arise because for  $0 \leq \alpha \leq \beta_{\infty}(1 - \sin i)$  the isowavelength-shift contours are "closed" curves on the stellar disc (see Fig. 2.10) with the maximum and minimum  $x$  values given by Eq. 2.26. (Note that the  $\alpha = \beta_{\infty}(1 - \sin i)$  contour "closes" at infinity.) For  $\alpha \geq \beta_{\infty}(1 - \sin i)$  the isowavelength-shift contours "break" and tend to radial lines for,

$$\cos \phi_0 = \frac{\beta_{\infty} - \alpha}{\beta_{\infty} \sin i}, \quad (2.28)$$

thus giving the infinite upper limit in Eq. 2.27.

Equation 2.24 can be simplified by noting that in a steady disc wind the continuity equation gives,

$$\Sigma(x) = \frac{\Sigma_1}{\beta_r(x) x}, \quad (2.29)$$

where  $\Sigma_1$  is a constant. Now making the change of variable,

$$z = \frac{\alpha - \beta_r(x)}{\beta_r(x) \sin i}, \quad (2.30)$$

in Eq. 2.24 where  $\beta_r(x)$  is given by Eq. 2.25 yields,

$$\left\{ \begin{array}{l} \nu F_{\nu}^I(\alpha) \\ \nu F_{\nu}^Q(\alpha) \end{array} \right\} = 2\sigma_0 F_0 \frac{\Sigma_1 \alpha^{\frac{1}{\gamma}-2}}{\gamma \beta_{\infty}^{\frac{1}{\gamma}}} \left\{ \begin{array}{l} G_1(\alpha, \gamma, i) + \sin^2 i G_2(\alpha, \gamma, i) \\ G_1(\alpha, \gamma, i) - (1 + \cos^2 i) G_2(\alpha, \gamma, i) \end{array} \right\}, \quad (2.31)$$

where the  $G$  functions are

$$\left\{ \begin{array}{l} G_1(\alpha, \gamma, i) \\ G_2(\alpha, \gamma, i) \end{array} \right\} = \int_{\max[-1, (\alpha - \beta_{\infty})/\beta_{\infty} \sin i]}^1 \frac{dz}{\sqrt{1 - z^2} (1 + z \sin i)^{\frac{1}{\gamma}-1}} \left\{ \begin{array}{l} 1 \\ z^2 \end{array} \right\}. \quad (2.32)$$

Analysis of the scattered Stokes fluxes then yields the parameters  $\gamma$ ,  $i$  and  $\beta_{\infty}$  in the following way.

From Eqs. 2.31 and 2.32 it is clear that for  $0 \leq \alpha \leq \beta_{\infty}(1 - \sin i)$  the spectral shape of the scattered Stokes fluxes is governed by  $\gamma$  which may be obtained from,

$$\frac{d \log F_{\nu}^I(\alpha)}{d\alpha} = \frac{d \log F_{\nu}^Q(\alpha)}{d\alpha} = \frac{1}{\gamma} - 2. \quad (2.33)$$

Determination of  $\gamma$  in this way requires analysis of the Stokes fluxes for small  $\alpha$  (i.e.  $0 \leq \alpha \leq \beta_{\infty}(1 - \sin i)$ ) since for  $\alpha > \beta_{\infty}(1 - \sin i)$  the integration limits in Eq. 2.32 contain  $\alpha$ , thus giving a more complex  $\alpha$ -dependence of the scattered Stokes fluxes.

Once  $\gamma$  is determined from Eq. 2.33 the inclination may be obtained, again for  $0 \leq \alpha \leq \beta_\infty(1 - \sin i)$ , from,

$$\frac{F_V^Q(\alpha)}{F_V^Q(\alpha)} = \frac{1 + g(i, \gamma) \sin^2 i}{1 - g(i, \gamma)(1 + \cos^2 i)}, \quad (2.34)$$

where  $g(i, \gamma) = G_2(\alpha, \gamma, i)/G_1(\alpha, \gamma, i)$  which is independent of  $\alpha$  for  $0 \leq \alpha \leq \beta_\infty(1 - \sin i)$ . The inclination is only uniquely determined in this way if the right hand side of Eq. 2.34 is monotonic in  $i$  for the given  $\gamma$ . This is only true for  $\gamma \geq 1$  as is illustrated in Fig. 2.11, thus  $i$  can only be determined uniquely for these  $\gamma$  values. It is to be noted that, as in the pure rotation case, determination of the inclination requires polarimetry in addition to spectrometry.

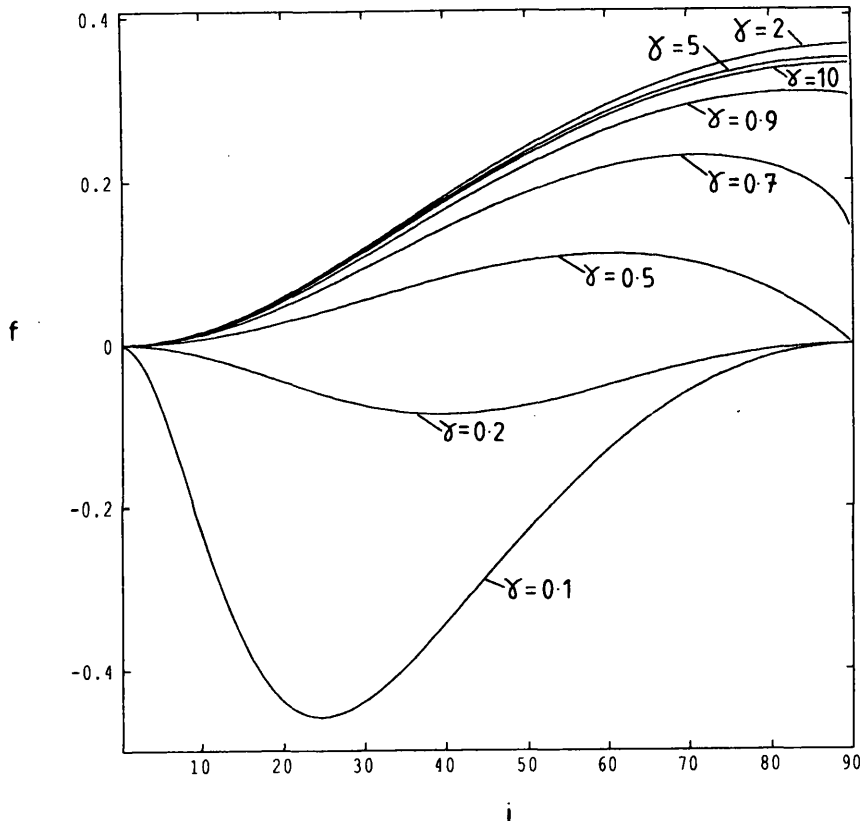


Fig. 2.11 The function  $f(i, \gamma) = [1 + g(i, \gamma) \sin^2 i]/[1 - g(i, \gamma)(1 + \cos^2 i)]$  for various  $\gamma$  values.

The terminal velocity,  $\beta_\infty$ , is now determined from the maximum  $\alpha$  value of the scattered Stokes fluxes which is  $\alpha_{\max} = \beta_\infty(1 + \sin i)$  for this particular velocity parameterisation (note that  $\alpha_{\min} = 0$  for scattering of radiation at the stellar surface where the wind velocity is zero in accordance with Eq. 2.25).

### Illustrative example

The analysis presented above allows the Stokes fluxes for any  $i$  and  $\gamma$  to be calculated numerically from Eq. 2.31. Returning to Eq. 2.24 an analytic form for the scattered Stokes fluxes arises when the expansion velocity is constant throughout the disc (i.e.  $\gamma = 0$  in Eq. 2.25). Physically this constant velocity law is equivalent to assuming that the acceleration zone is very thin. Assuming

then that the outflow velocity is given by  $\beta_r(r) = \beta_\infty$ , the resulting Stokes fluxes are then,

$$\begin{pmatrix} \nu F_\nu^I(\alpha) \\ \nu F_\nu^Q(\alpha) \\ \nu F_\nu^U(\alpha) \end{pmatrix} = \frac{2\sigma_0 F_0 \Sigma_1}{|\sin \phi_1| \beta_\infty \sin i} \begin{pmatrix} 1 + \sin^2 i \cos^2 \phi_1 \\ \sin^2 i - (1 + \cos^2 i) \cos 2\phi_1 \\ 0 \end{pmatrix}, \quad (2.35)$$

where the limits on the  $x$ -integrals, Eq. 2.24, are 1 and  $\infty$  as is evident from the form of the isowavelength-shift contours for this velocity profile (radial lines) shown in Fig. 2.13. The wavelength dependence enters via  $\phi_1$  which is given by,

$$\cos \phi_1 = \frac{\alpha - \beta_\infty}{\beta_\infty \sin i}. \quad (2.36)$$

These profiles are shown in Fig. 2.12 and are explained with reference to the isowavelength-shift contours in Fig. 2.13. The maximum and minimum  $\alpha$  values of the scattered spectral profile for this case are given by,

$$\alpha_{\min} = \beta_\infty(1 - \sin i), \quad \alpha_{\max} = \beta_\infty(1 + \sin i). \quad (2.37)$$

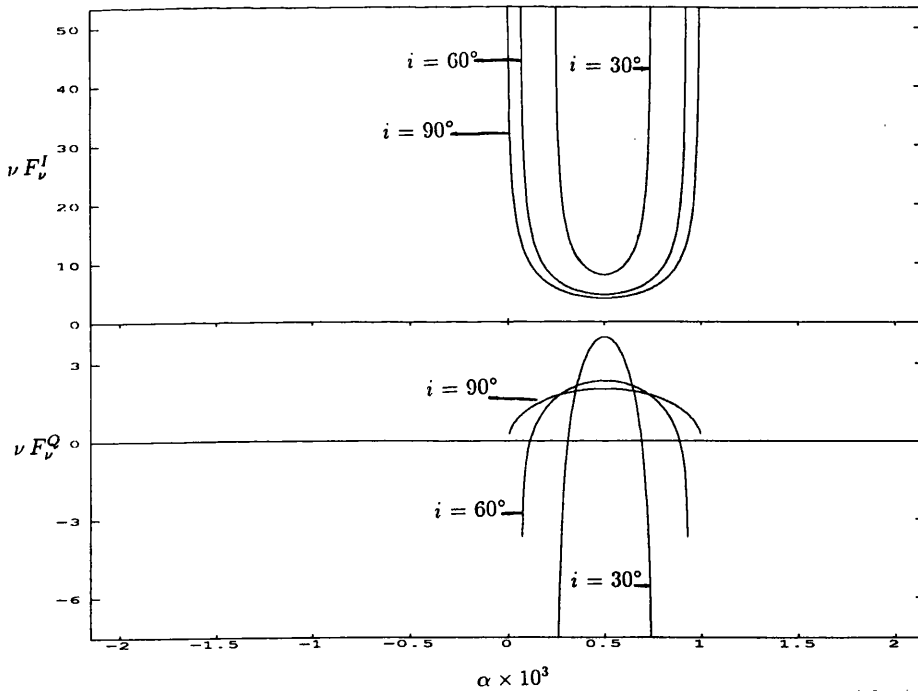


Fig. 2.12 The resulting Stokes fluxes after scattering monochromatic stellar line radiation in a disc expanding with a constant velocity of  $150 \text{ km.s}^{-1}$ .

For pure expansion the two Doppler shifts described by Eq. 2.1 result in light scattered from any region of the disc appearing red-shifted with respect to that emitted by the star, except for  $i = 90^\circ$  when the two shifts exactly cancel along the line  $\phi = 0$ . Figure 2.13 shows isowavelength-shift contours on a disc expanding at a constant velocity for  $i = 60^\circ$  and illustrates that due to the two Doppler shifts the greatest total red-shift will occur for the back half of the disc.

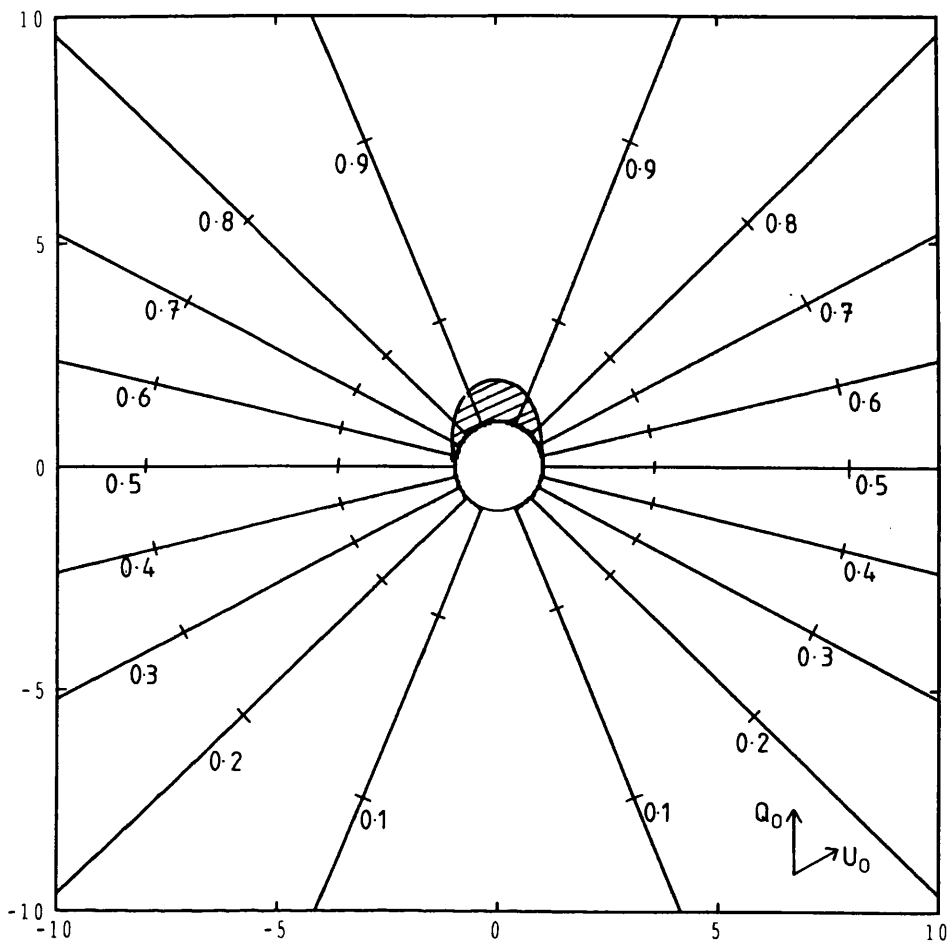


Fig. 2.13 As for Fig. 2.9 except for a disc expanding at a constant velocity.

The polarisation vectors along each isowavelength-shift contour will combine to give a net  $Q$ , but no  $U$  flux due to the left/right symmetry of the contours. The contours for the extreme  $\alpha$  values given by Eq. 2.37 are radial lines parallel to the line of sight to the observer. The scattered  $I$  flux for these  $\alpha$  values is maximum since the scattering phase function takes its maximum value along these  $\alpha$ -contours, as described in the previous section on pure disc rotation. Towards intermediate  $\alpha$  values the scattering phase function decreases along the contours resulting in a decrease in  $F^I$ . For the extreme  $\alpha$  values the  $Q$  flux is negative as is evident from the scattered polarisation vectors along these contours, and swings positive at intermediate values.

For this parametrisation of the disc outflow velocity the only parameters influencing the scattered fluxes are the disc inclination and the outflow speed which are both determined by Eq. 2.37 using measurements of  $\alpha_{\min}$  and  $\alpha_{\max}$ . The  $\alpha_{\min}$  and  $\alpha_{\max}$  contours, being radial lines along  $\phi = 0$  and  $\pi$  respectively, give different scattering angles and Doppler shifts of the stellar radiation from the front and rear halves of the disc such that the expansion velocity and inclination enter the expressions for  $\alpha_{\min}$  and  $\alpha_{\max}$  in a separable fashion, thus enabling these parameters to be determined from spectroscopy alone – again providing  $F^I$  can be separated from the direct stellar flux.

### 2.5.3 Rotation and expansion

When the disc velocity is a combination of rotation and expansion Eq. 2.10 gives, for  $\beta_r \ll 1$ ,

$$\begin{aligned} \phi_0 &= \cos^{-1} \left( \frac{\beta_r(x) - \alpha}{\sqrt{\beta_r(x)^2 + \beta_\phi(x)^2 \sin^2 i}} \right) - \tan^{-1} \left( \frac{\beta_\phi(x)}{\beta_r(x)} \right), \\ 2\pi - \phi_0 &= \cos^{-1} \left( \frac{\beta_r(x) - \alpha}{\sqrt{\beta_r(x)^2 + \beta_\phi(x)^2 \sin^2 i}} \right) - \tan^{-1} \left( \frac{\beta_\phi(x)}{\beta_r(x)} \right). \end{aligned} \quad (2.38)$$

When these values are inserted into Eq. 2.12 and summed over the individual  $\phi_0$ s the scattered Stokes fluxes are,

$$\begin{Bmatrix} \nu F_\nu^I(\alpha) \\ \nu F_\nu^Q(\alpha) \\ \nu F_\nu^U(\alpha) \end{Bmatrix} = 4\sigma_0 F_0 \begin{Bmatrix} I_5(\alpha) + \sin^2 i I_6(\alpha) \\ I_5(\alpha) - (1 + \cos^2 i) I_6(\alpha) \\ 2 \cos i I_7(\alpha) \end{Bmatrix}, \quad (2.39)$$

where the integral functions are, again assuming  $\beta_r \ll 1$ ,

$$I_5(\alpha) = \int \frac{\Sigma(x) dx}{x \sqrt{(\beta_r^2 + \beta_\phi^2) \sin^2 i - (\alpha - \beta_r)^2}}, \quad (2.40)$$

$$I_6(\alpha) = \int \frac{\Sigma(x) [\beta_r^2 (\alpha - \beta_r)^2 + \beta_\phi^2 \{(\beta_r^2 + \beta_\phi^2) \sin^2 i - (\alpha - \beta_r)^2\}] dx}{x (\beta_r^2 + \beta_\phi^2)^{\frac{3}{2}} \sin^2 i \sqrt{(\beta_r^2 + \beta_\phi^2) \sin^2 i - (\alpha - \beta_r)^2}}, \quad (2.41)$$

$$I_7(\alpha) = \int \frac{\Sigma(x) \beta_r \beta_\phi [(\beta_r^2 + \beta_\phi^2) \sin^2 i - 2(\alpha - \beta_r)^2] dx}{x (\beta_r^2 + \beta_\phi^2)^{\frac{3}{2}} \sin^2 i \sqrt{(\beta_r^2 + \beta_\phi^2) \sin^2 i - (\alpha - \beta_r)^2}}. \quad (2.42)$$

The complex dependence of the scattered Stokes fluxes on the disc velocity structure does not appear to yield a simple parametric inversion of the equations similar to those of Sects. 3.1 and 3.2. The inversion procedure for this case of the rotational and expansional components of the disc velocity being comparable is not considered in this thesis and for now a numerical solution is presented for the scattered Stokes fluxes of Eqs. 2.39.

Assuming the rotational component of the velocity to be parameterised by Eq. 2.17 and the outflow velocity is constant then the lower limit of the  $x$  integral is 1 and the upper limits of the integral depend on  $\alpha$  in the following way.

For  $(\beta_1 - \sqrt{\beta_1^2 + \beta_0^2} \sin i)/(1 - \beta_1) \leq \alpha \leq \beta_1(1 - \sin i)/(1 - \beta_1)$  and  $\beta_1(1 + \sin i)/(1 - \beta_1) \leq \alpha \leq (\beta_1 + \sqrt{\beta_1^2 + \beta_0^2} \sin i)/(1 - \beta_1)$  then

$$x_{\max} = \frac{(\beta_0 \sin i)^{\frac{1}{p}}}{([\beta_1 - \alpha(1 - \beta_1)]^2 - \beta_1^2 \sin^2 i)^{\frac{1}{p}}}, \quad (2.43)$$

where  $\beta_0$  and  $\beta_1$  are as before. While for  $\beta_1(1 + \sin i)/(1 - \beta_1) \leq \alpha \leq \beta_1(1 + \sin i)/(1 - \beta_1)$  then

$$x_{\max} = \infty. \quad (2.44)$$

The upper limit of infinity for these particular  $\alpha$  values is explained by considering the isowavelength-shift contours for this velocity profile in Fig. 2.15 (with the rotation being Keplerian). It is seen that for these  $\alpha$  values the contours tend to radial lines at large radial distances (producing a similar pattern to the contours in Fig. 2.13) where  $\phi_0$  becomes independent of  $x$  and hence the infinite upper limit. This contour shape occurs because the disc velocity for these outer regions is dominated by the constant expansion velocity – rotation dominating the contour shape close to disc centre due to its  $x^{-p}$  parametrisation.

The  $\alpha$  range of scattered radiation for this case of disc rotation and expansion is,

$$(\beta_1 - \sqrt{\beta_1^2 + \beta_0^2 \sin i}) / (1 - \beta_1) \leq \alpha \leq (\beta_1 + \sqrt{\beta_1^2 + \beta_0^2 \sin i}) / (1 - \beta_1). \quad (2.45)$$

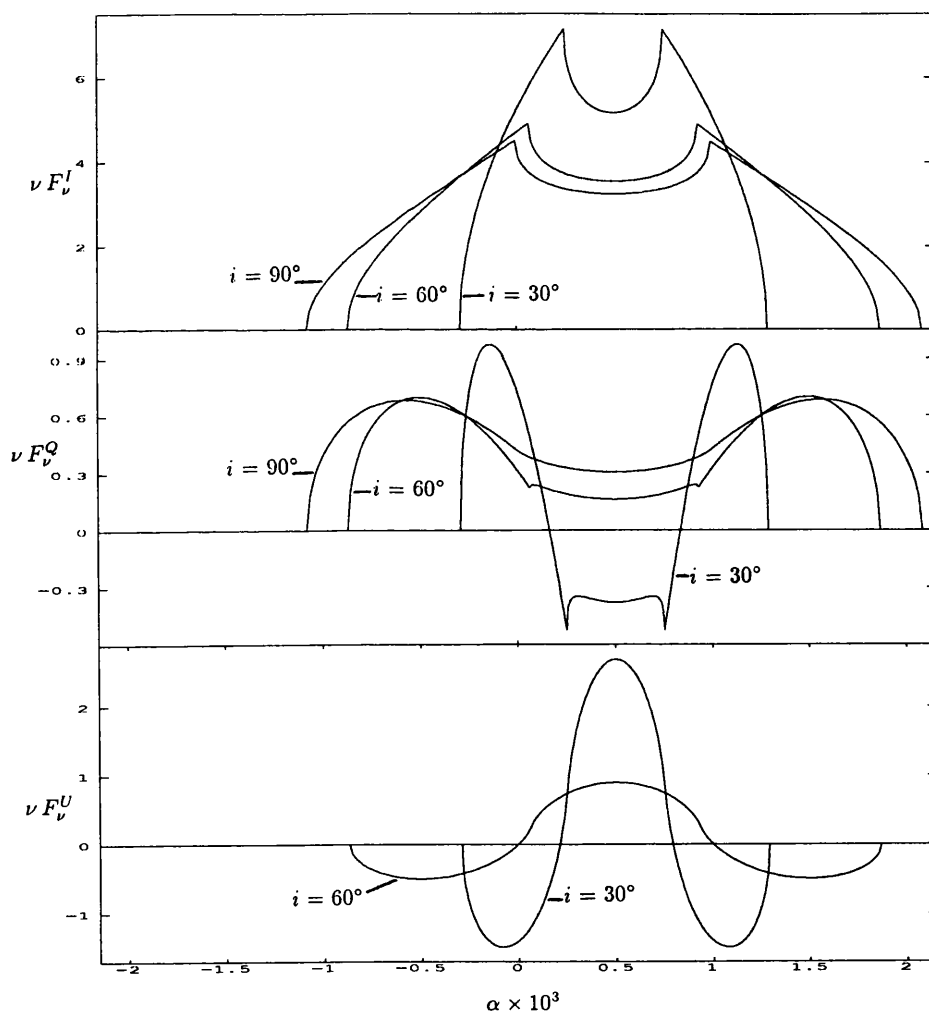


**Fig. 2.14** The resulting Stokes fluxes after scattering monochromatic stellar line radiation in a disc rotating with a Keplerian velocity profile and expanding with a constant velocity.

Figure 2.14 shows the computed scattered Stokes fluxes for this case of a rotating, expanding disc which are explained with reference to the isowavelength-shift contours in Fig. 2.15. For the extreme  $\alpha$  values in Eq. 2.45 the scattered  $I$  and  $Q$  fluxes resemble those of Fig. 2.8 since they arise from scattering close to disc centre where rotation dominates the contour shape. At intermediate values of Eq. 2.45 the scattered  $I$  and  $Q$  fluxes arise from scattering off contours whose shape is dominated by the constant expansion velocity thus yielding results similar to the pure disc expansion case in Fig. 2.12. The symmetry-breaking effect on the contours due to the combination of expansion and rotation results in a net  $U$  flux on summing over individual contours. It is evident that all three Stokes flux profiles of Fig. 2.14 are symmetric about the midpoint of Eq. 2.45 due to the  $\alpha$  contours on the disc being symmetric about this value.

The profiles are all red-shifted from line centre due to the red-shifting effect of scattering off electrons in an expanding envelope explained in the previous section.

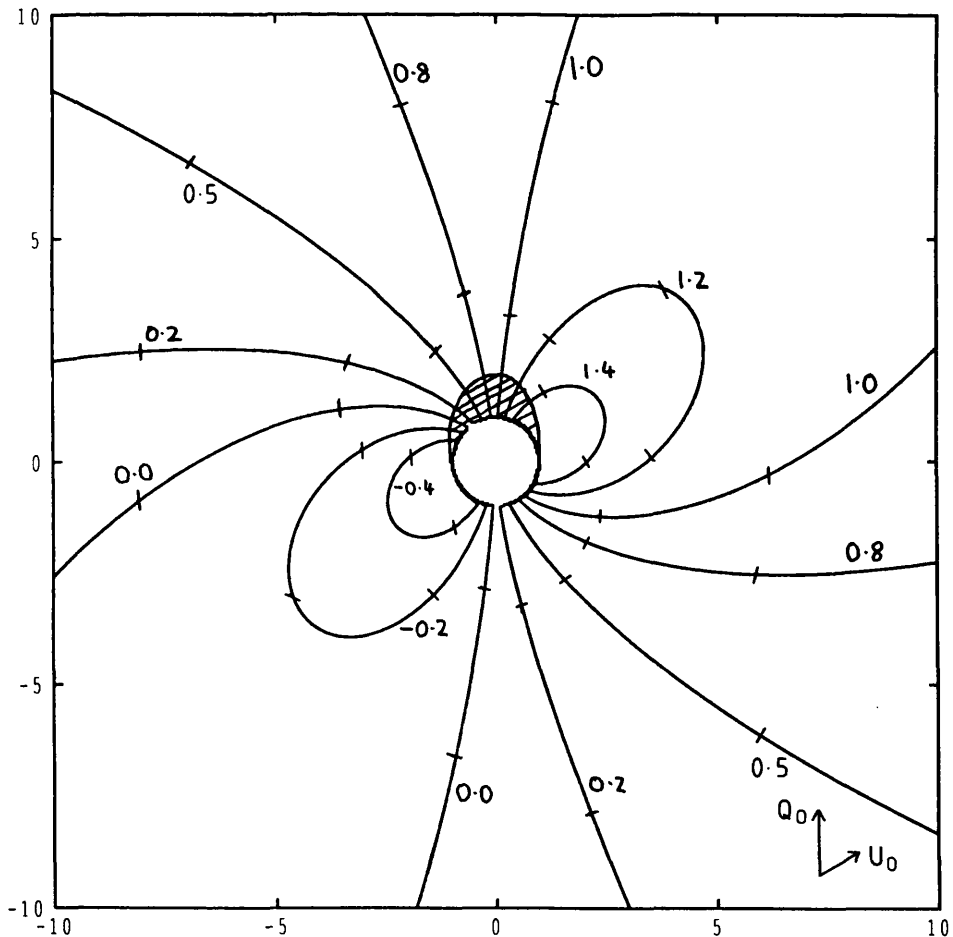


Fig. 2.15 As for Fig. 2.9 except for a rotating and expanding disc.

## 2.6 Non-monochromatic source

In this section the scattering of non-monochromatic line radiation superposed on a continuum is considered. The stellar spectrum line source is taken to have a gaussian line profile superposed on the continuum so that around  $\lambda_0$  the intensity is

$$I_{\nu_*}(\lambda_*) = I_0 \left[ 1 + s \exp - \left( \frac{\lambda_* - \lambda_0}{\lambda_b} \right)^2 \right], \quad (2.46)$$

where  $I_0$  is the continuum specific intensity,  $\lambda_*$  is the wavelength emitted by the star,  $\lambda_0$  is the rest wavelength at the line centre and  $\lambda_b$  is the width of the stellar line.  $s$  gives the strength of the line relative to the continuum with  $-1 < s < 0$  and  $s > 0$  corresponding to absorption and emission lines respectively. Equation 2.5 enables the exponent in Eq. 2.46 to be written as,

$$\left( \frac{\lambda_* - \lambda_0}{\lambda_b} \right)^2 = A(r, \phi, \lambda)^2, \quad (2.47)$$

where  $A(r, \phi, \lambda)$  is,

$$A(r, \phi, \lambda) = \frac{\{1 - \beta_r(r)\}\lambda - \{1 - \beta_r(r) \sin i \cos \phi + \beta_\phi(r) \sin i \sin \phi\} \lambda_0}{\{1 - \beta_r(r) \sin i \cos \phi + \beta_\phi(r) \sin i \sin \phi\} \lambda_b}, \quad (2.48)$$

Equation 2.48 describes the Doppler redistribution of scattered photons and is the key equation governing the scattered spectropolarimetric line profile. It should be noted that although  $\beta_r$  and  $\beta_\phi$  are much less than unity the rapid variation with wavelength of the line profile in Eq. 2.46 requires that all the terms in Eq. 2.48 should be retained since they will yield significant variation in the wavelength shifts from different disc regions and thus also in the scattered spectropolarimetric line profile.

The scattered Stokes fluxes are now given by Eqs. 2.3 and 2.13 thus,

$$\begin{Bmatrix} F_\nu^I \\ F_\nu^Q \\ F_\nu^U \end{Bmatrix} = \sigma_0 F_0 \int_A (1 + s \exp - \{A(r, \phi, \lambda)\}^2) \Sigma(r) \begin{Bmatrix} 2(1 + \sin^2 i \cos 2\phi) \\ \sin^2 i - (1 + \cos^2 i) \cos 2\phi \\ 2 \cos i \sin 2\phi \end{Bmatrix} \frac{dA}{r^2}. \quad (2.49)$$

The Stokes parameters are formed by dividing the  $Q$  and  $U$  fluxes above fluxes by the direct flux – neglecting  $F_\nu^I$  for the reasons given in Sect. 2.3 for the scattering of line radiation in the presence of a continuum. Following Fox and Brown (1991), the area,  $A$ , is the area of the disc minus the area occulted by the star and the integral operator is given in Eq. 1.34.

A subtlety to be noted here is that, unlike the case of a monochromatic source, the incident Gaussian line profile is non-zero at all frequencies and so there is a non-zero contribution to the scattered flux at each scattered frequency from each frequency in the incident spectrum. The effect of this is that at each wavelength there will be a contribution to the scattered flux arising from the *entire* disc and not simply from the discrete isowavelength-shift contours of the previous sections. However, most of the scattered flux at a given wavelength will arise from a “smeared” region around

the particular isowavelength contour with the “degree of smearing” being proportional to the line width,  $\lambda_b$  – e.g. when  $\lambda_b$  tends to zero the incident line profile becomes very sharp (i.e. approaches monochromaticity) and the regions contributing to the scattered flux at a given wavelength tend to the discrete contours of before.

Due to the complexity of the integrals the Stokes  $Q$  and  $U$  fluxes are computed by a numerical quadrature routine, with and without occultation, for cases when the disc velocity is purely rotational, purely expansional and a combination of these. Figs. 2.16–2.18 show the Stokes fluxes, the degree of linear polarisation and position angle for the case of an emission line originating at the star centre and being single Thomson scattered in the disc. The input profile is given by Eq. 2.46 with  $s = 2$ , the line centre at  $\lambda_0 = 6562 \text{ \AA}$  ( $H_\alpha$ ), and a width of  $\lambda_b = 4 \text{ \AA}$  corresponding to a characteristic broadening velocity of about  $180 \text{ km.s}^{-1}$ . This line is assumed to be broadened in the photosphere prior to Thomson scattering in the disc whose radius is ten times the stellar radius ( $\alpha_D = 10$  in Eq. 1.37). A possible broadening mechanism could be Linear Stark Broadening, Griem (1960), at a photospheric electron number density of about  $10^{16} \text{ cm}^{-3}$ . The rotational velocity is assumed to be Keplerian with  $v_0 = 450 \text{ km.s}^{-1}$ , while the expansion velocity is given by Eq. 2.25 with  $v_\infty = 150 \text{ km.s}^{-1}$  and  $\gamma = 1/2$ . These parameter values are typical of Be star discs.

### 2.6.1 Pure disc rotation

In this case the surface number density and velocity are given by Eq. 2.17 with  $p = 1/2$  and  $q = 1$ , the expansion velocity being zero.

#### 2.6.1 (a) Point source without occultation

From Fig. 2.16(b) (solid lines) the polarimetric profile,  $P_0 = \sigma_0 \Sigma_0$ , is seen to be symmetric about the line centre, being stronger in the wings and less towards line centre than the continuum polarisation due to the depolarising effect of direct line radiation. The position angle is zero at all frequencies. These variations are explained in a similar manner as that presented in Section 2.4

The scattered Stokes  $I$  and  $Q$  fluxes in Fig. 2.16(a), for this case of pure rotation (solid lines – neglecting occultation), have similar spectral shapes to those presented in Fig 2.8, but do not go to zero at a maximum wavelength-shift. This arises since the initial Gaussian line profile is non-zero at all wavelengths thus giving a non-zero contribution to the scattered flux at all wavelengths even if the constant continuum were to be removed. The  $U$  flux (and hence the position angle also) is zero at all wavelengths due to the front-back symmetrical cancellation described in Section 2.4.1. The degree of polarisation is then determined by dividing  $F^Q$  by the direct flux (assuming  $F^I \ll F^D$ ) and hence the spectral shape of Fig. 2.16(b).

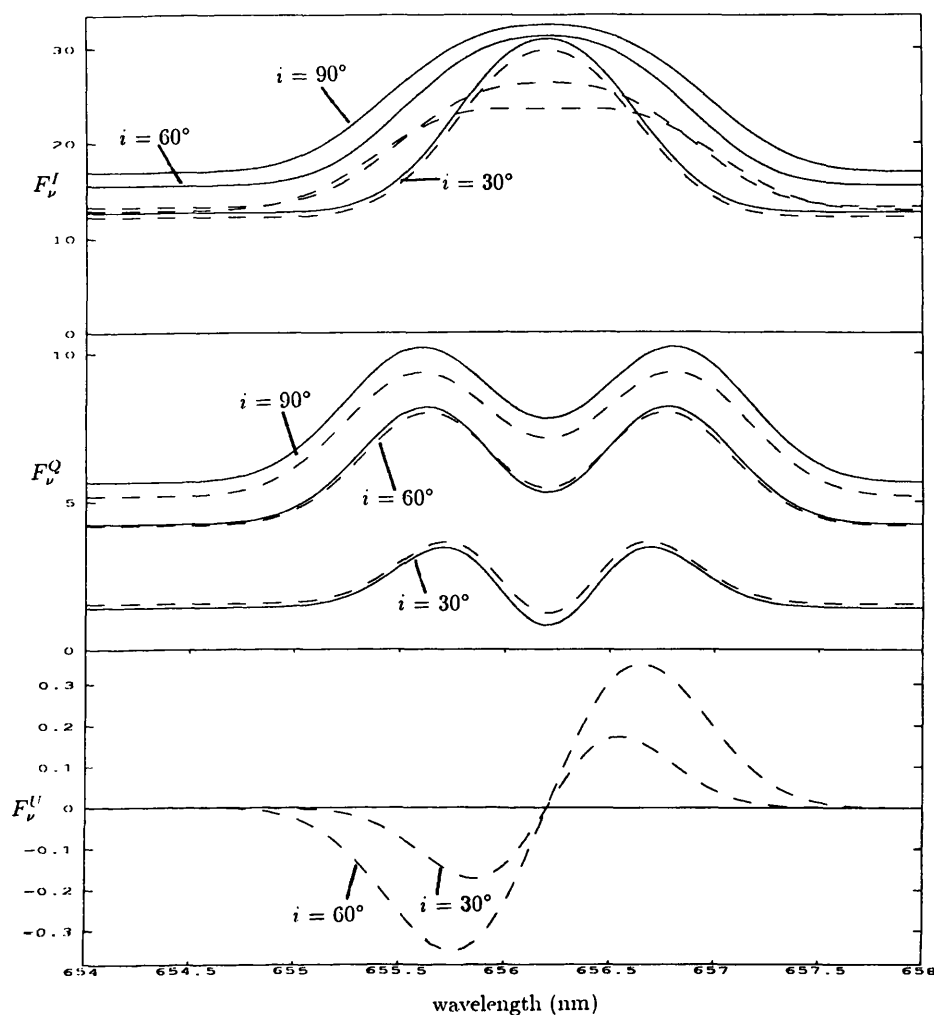


**Fig. 2.16 (a)** The resulting Stokes fluxes for scattering stellar radiation with a spectral shape given by Eq. 2.46 in a Keplerian rotating disc whose velocity at the stellar surface is  $450 \text{ km.s}^{-1}$ . The solid curve is for a point source and the dotted curve is for a point source with occultation effects included. The pairs of curves are for inclinations of  $30^\circ$ ,  $60^\circ$  and  $90^\circ$ .

### 2.6.1 (b) Point source with occultation

From Fig. 2.16(b) (dashed lines) the degree of polarisation is seen to have the same spectral shape as the previous case, but occultation has resulted in an asymmetric position angle variation with wavelength which is again explained with reference to Fig. 2.9, as follows.

When occultation is included photons from the occulted area of the disc (the shaded region in Fig. 2.9) are unable to reach the observer and are effectively removed, cf Eq. 1.34. From Fig. 2.9 it is seen that this occultation removes the positive  $U$  and  $Q$  contributions in the blue and the negative  $U$  and positive  $Q$  contributions in the red. Hence  $U$  changes sign – Fig. 2.16(a) – and  $\Psi$  rotates across line centre from negative to positive (where positive and negative position angles here mean  $0^\circ < \Psi < 90^\circ$  and  $90^\circ < \Psi < 180^\circ$  respectively). As the inclination increases the scattered  $I$  flux is reduced since a progressively larger area of the disc is being occulted thus reducing the total scattered flux.

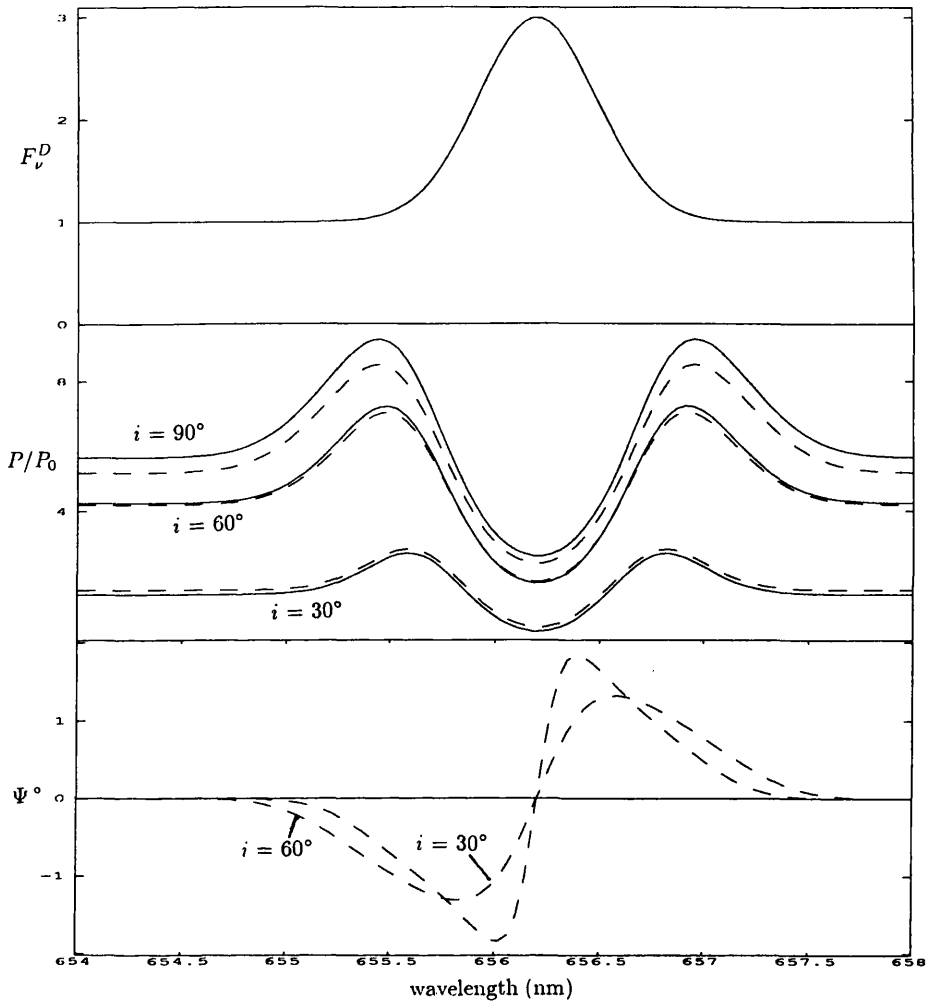


Fig. 2.16 (b) The direct flux (Eq. 2.46) normalised to the continuum, the scattered polarisation,  $P_0 = \sigma_0 \Sigma_0$ , and position angle for the rotating disc.

Another (small) effect of occultation, explained in Sect. 1.4.4, is that, for low inclinations, occultation serves to enhance the polarisation, while for high values of inclination it has the effect of reducing the polarisation.

### 2.6.2 Pure disc expansion

For this case the density distribution and velocity field are the same as presented in Eqs. 2.25 and 2.29. Results are shown in Fig. 2.17 for a point source with and without the effects of occultation. These spectral shapes are explained with reference to the isowavelength-shift contours in Fig. 2.10.

The Stokes flux,  $F_\nu^Q$ , has a profile resembling the direct flux, but is red-shifted due to the disc expansion velocity and the  $U$  flux is zero at all wavelengths due the left-right symmetry of the isowavelength-shift contours in Fig. 2.10. Occultation will remove polarised flux from the back half of the disc and the remaining polarisation vectors will combine to give a net  $Q$ , but no

$U$  flux because of the left/right symmetry of Fig. 2.10 and hence no change in position angle. The spectral shape of the degree of polarisation is then again given by dividing  $F^Q$  by  $F^D$ . The gradual reduction of the  $I$  flux with increasing inclination and the enhancement in polarisation for low inclinations and the reduction at high inclinations is evident in Fig. 2.17 as it was for the pure rotation case.

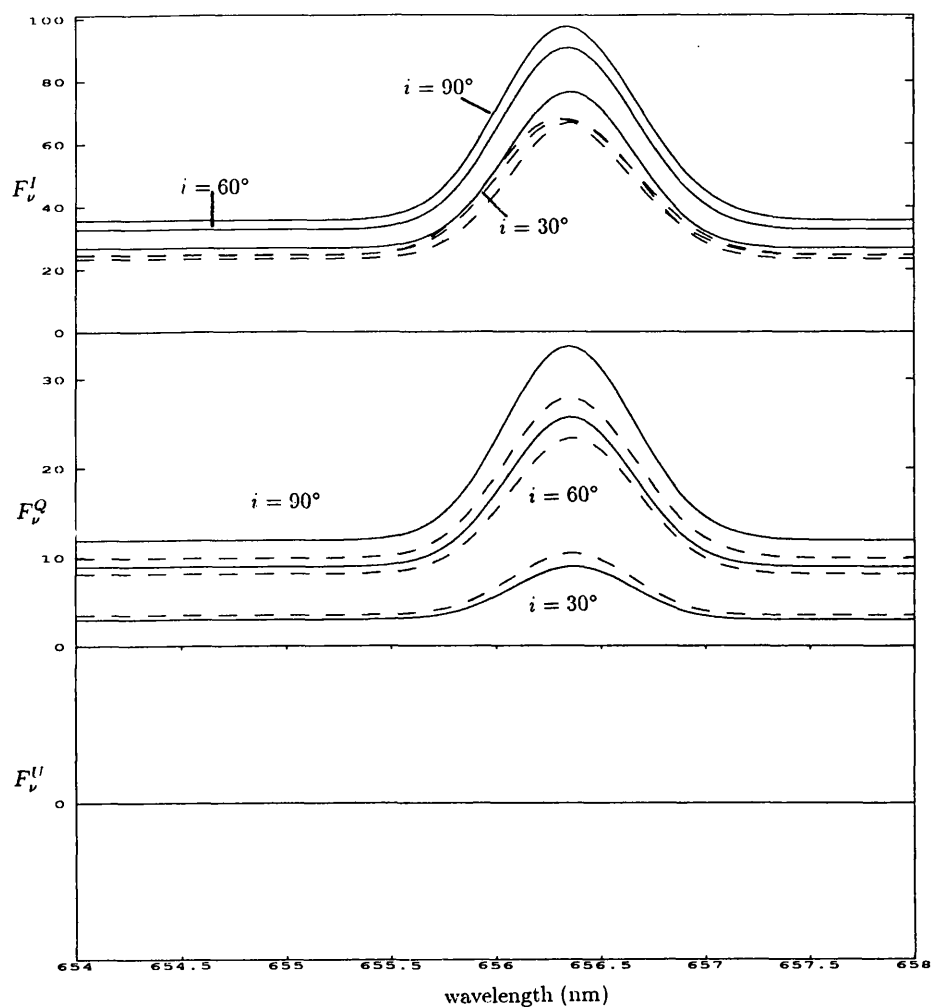


Fig. 2.17(a) As for Fig. 2.16(a), but for the disc velocity being purely expansional.

### 2.6.3 Disc expansion and rotation

In this case the density distribution and velocity field are given by Eqs. 2.17 (Keplerian rotation), 2.25 and 2.29. Figures 2.18(a-b) show the polarisation,  $P_0 = \sigma_0 \Sigma_1$ , and position angle variations for a point source with and without occultation. The polarisation profiles obtained are similar to Figs. 2.16(a-b) but are stronger in the red wing due to the red-shifting effect of the disc expansion.

The change in position angle is explained with reference to Fig. 2.19. The isowavelength-shift contours in this figure show that the greatest red and blue shifts occur for regions of the disc where the  $U/Q$  component ratio of the polarisation vector is negative, so in the red and blue wings of

the line the position angle is negative. Towards the line centre the position angle swings positive. This is because the regions of small red and blue shift are where the  $U/Q$  ratio is positive.

Occultation removes the positive  $U$  and  $Q$  contributions in the blue and the negative  $U$  and positive  $Q$  contributions in the red, so the position angle is less in the blue and greater in the red compared to results without occultation. The enhancement in polarisation for low inclinations and the reduction at high inclinations is again evident in Fig. 2.18.

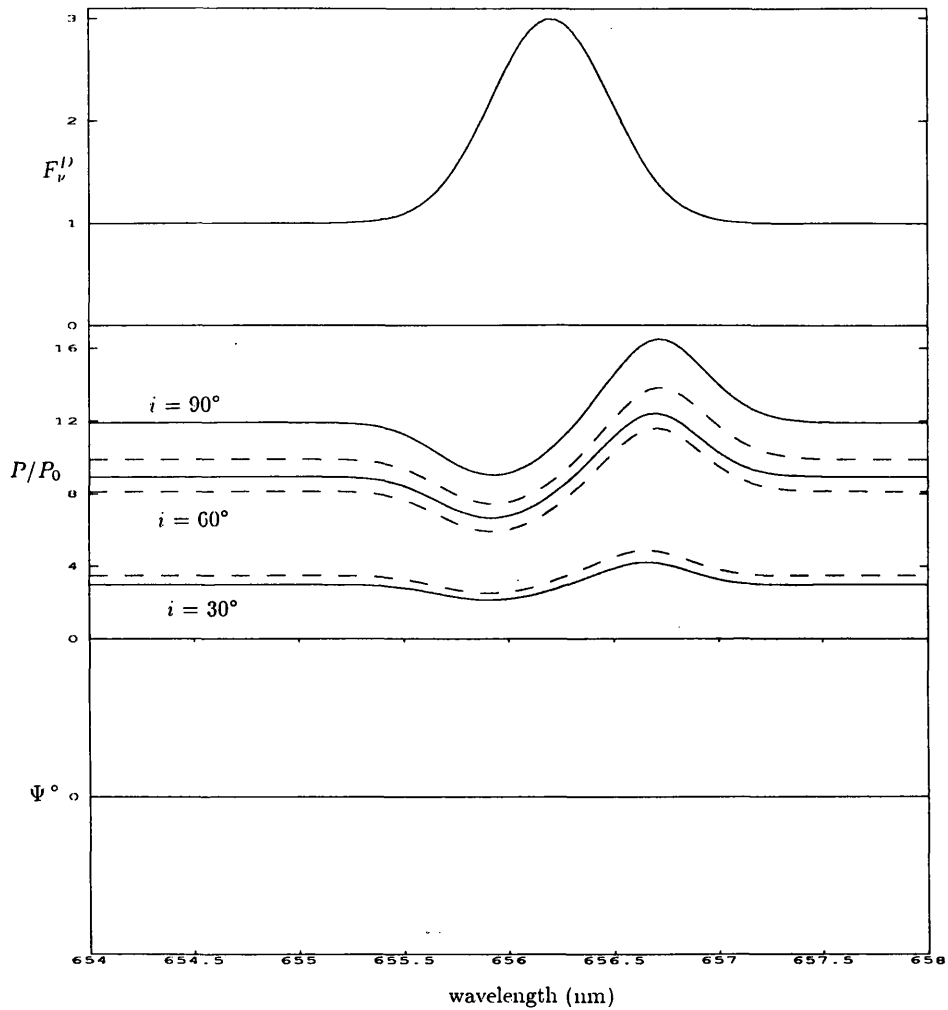


Fig. 2.17(b) As for Fig. 2.16(b), but for the disc velocity being purely expansional,  $P_0 = \sigma_0 \Sigma_1$ .

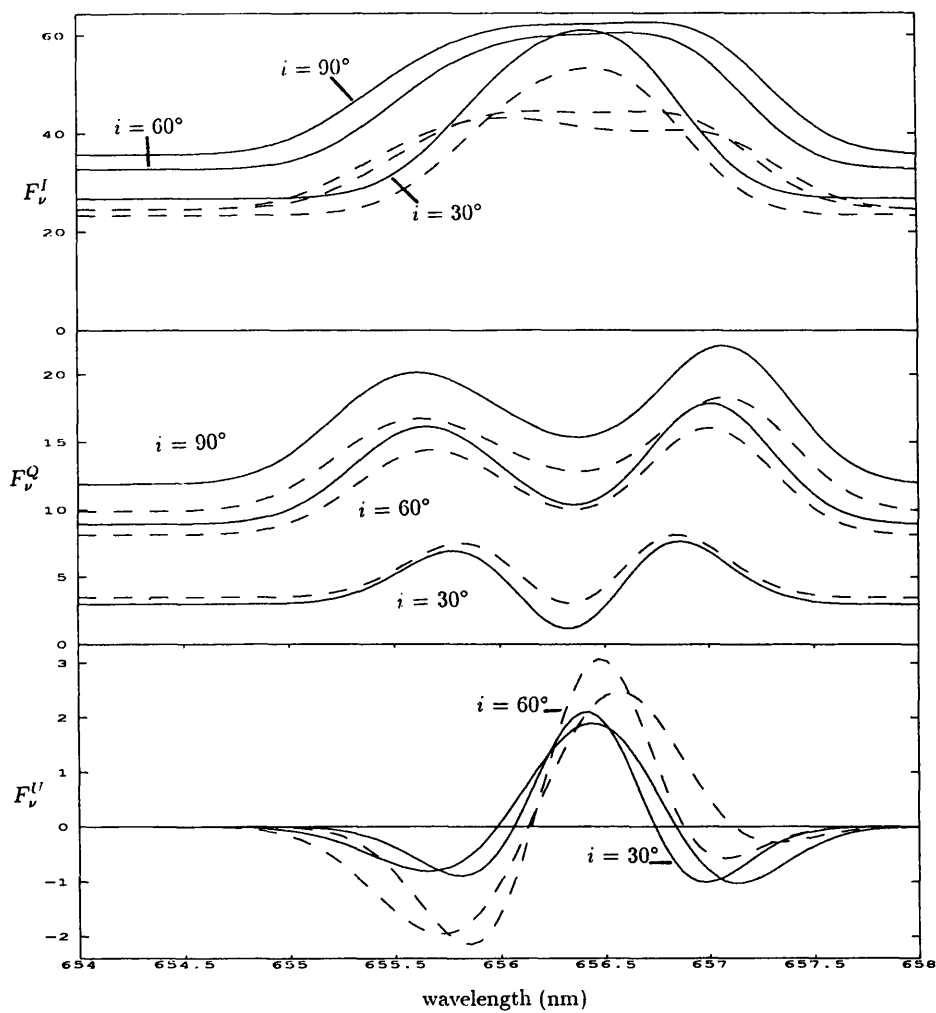


Fig. 2.18(a) As for Fig. 2.16(a), but for a rotating and expanding disc.

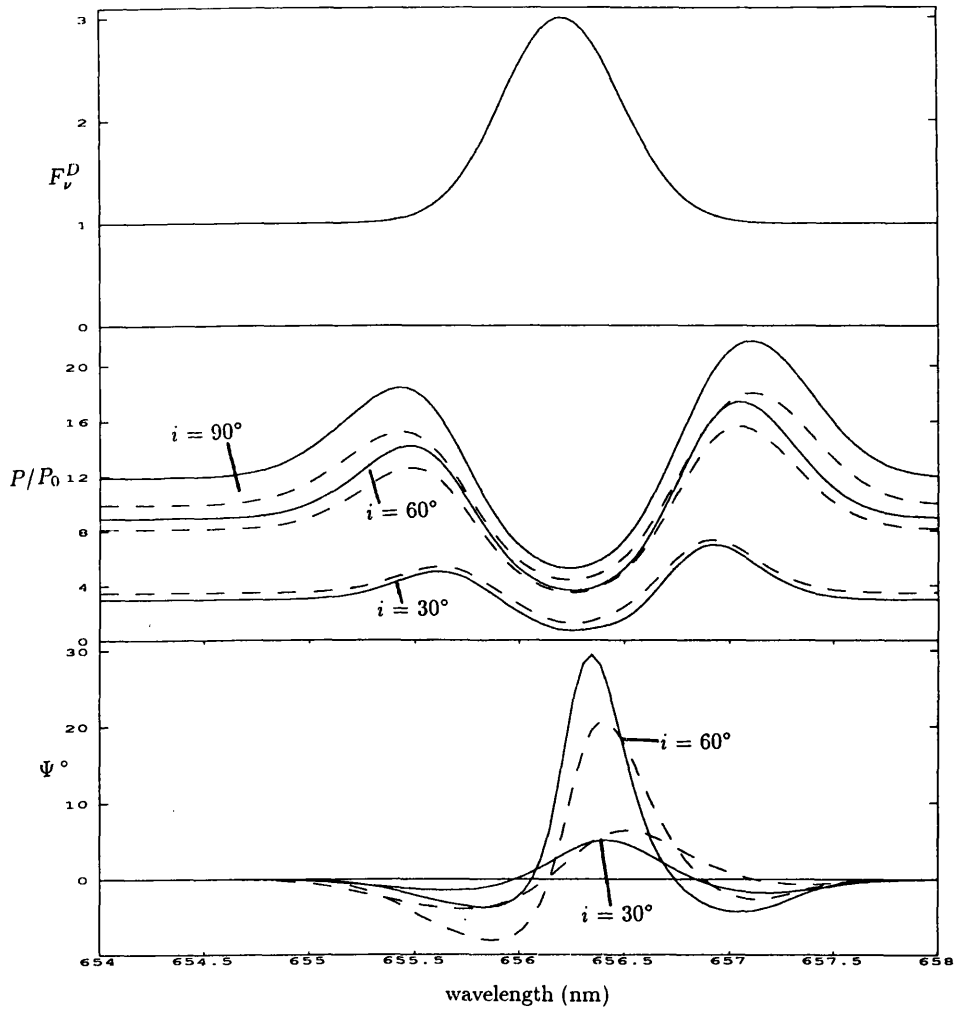
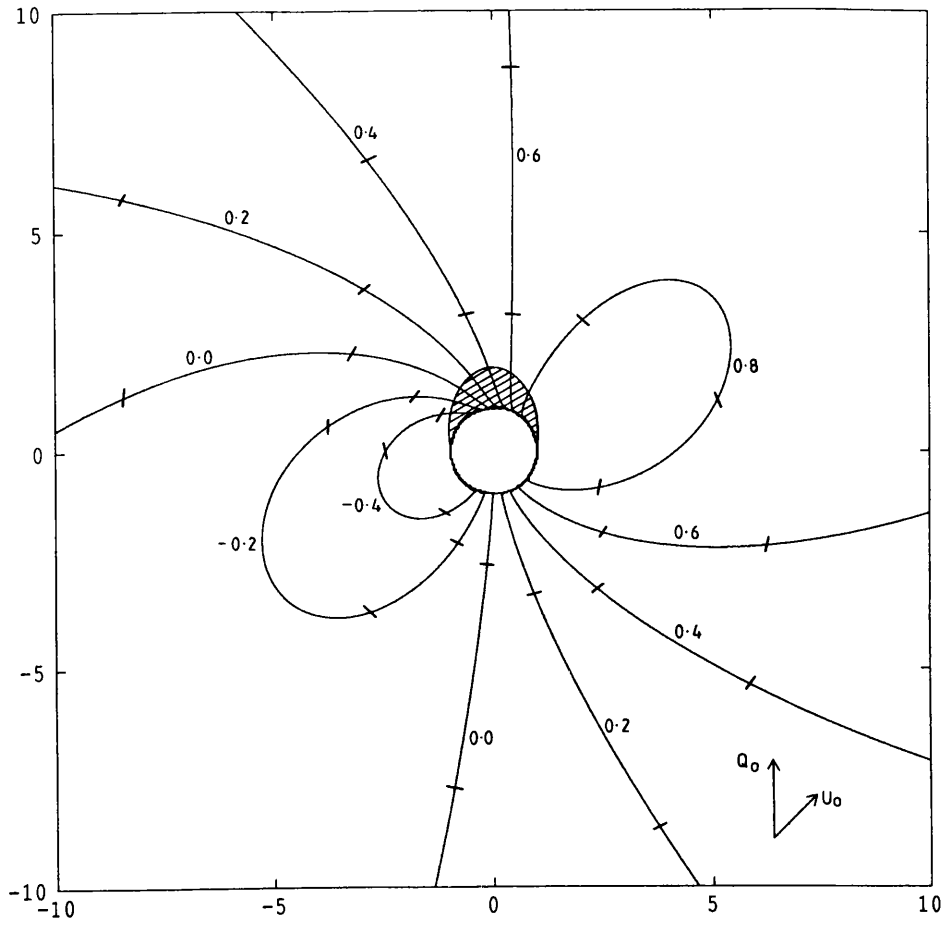


Fig. 2.18(b) As for Fig. 2.16(b), but for a rotating and expanding disc,  $P_0 = \sigma_0 \Sigma_1$ .



**Fig. 2.19** As for Fig. 2.9, but for a disc rotating with a Keplerian velocity and expanding with the stellar wind law of Eq. 2.25.

## 2.7 General determination of disc inclination

A more robust method to determine the disc inclination than that given in the monochromatic analysis of Sect. 2.4 is to determine the ratio of the wavelength integrated Stokes fluxes. Performing the integral over wavelength (or  $\alpha$ ) for the scattered Stokes fluxes from a monochromatic source requires Eqs. 2.16, 2.24, and 2.40–2.42 to be presented in a slightly different form. This is done in the next chapter which considers the general inversion technique to determine the disc velocity and density structure and the analysis is left until then. However, the wavelength integral can readily be performed for the non-monochromatic case of Sect. 2.5 and is presented here.

Integrating Eqs. 2.49 (with the constant continuum polarisation removed) over all scattered wavelengths (from 0 to  $\infty$ ) does not yield a simple analytic form due to the normalisation properties of the chosen line profile. Any line profile should, strictly, be normalised such that,

$$\int_0^{\infty} \phi(\lambda) d\lambda = 1, \quad (2.50)$$

where  $\phi(\lambda)$  determines the spectral shape of the line – e.g. Mihalas (1978). The Gaussian line profile in Sect 2.5 instead satisfies the normalisation condition,

$$\int_{-\infty}^{\infty} \phi(\lambda) d\lambda = 1. \quad (2.51)$$

However, the adoption of this particular stellar line profile may be justified by noting that, due to its exponential nature, there is a negligible contribution to the line profile at wavelengths which lie further than a few “e-folding” lengths from line centre,  $\lambda_0$ . When determining the integrated scattered Stokes fluxes it is therefore (mathematically) convenient to allow the scattered wavelengths to range from  $-\infty$  to  $\infty$ . Performing this wavelength integral in Eq. 2.49 then yields,

$$\begin{aligned} \begin{Bmatrix} F^I \\ F^Q \\ F^U \end{Bmatrix} &= \int_{-\infty}^{\infty} \begin{Bmatrix} F_{\nu}^I \\ F_{\nu}^Q \\ F_{\nu}^U \end{Bmatrix} d\lambda = \frac{\sigma_0 F_0 s}{\sqrt{2\pi}} \int_A \frac{\Sigma(r)}{(1 - \beta \cdot \hat{\mathbf{k}}_*) (1 - \beta \cdot \hat{\mathbf{k}})} \\ &\times \begin{Bmatrix} 2(1 + \sin^2 i \cos 2\phi) \\ \sin^2 i - (1 + \cos^2 i) \cos 2\phi \\ 2 \cos i \sin 2\phi \end{Bmatrix} \frac{dA}{r^2}. \end{aligned} \quad (2.52)$$

The bracketed terms on the denominator of this equation may be set equal to unity since the disc velocity is much less than that of light ( $\beta \ll 1$ ). Ignoring occultation effects the integration over the disc area is easily performed yielding,

$$\frac{F^Q}{F^I} = \frac{\sin^2 i}{2 + \sin^2 i}, \quad (2.53)$$

Equation 2.52 shows that the scattered  $U$  flux averages to zero across the line – as would be expected from the polarimetric cancellation properties of an axisymmetric disc. Since only Doppler

wavelength redistribution was considered in this scattering analysis the result of Eq. 2.53 is an obvious one since it is precisely the ratio of the scattered total to polarised broad-band fluxes for any disc as derived by Brown & McLean. If aberrational effects – which were ignored due to the slow disc speeds – were important then this result would not hold since the angular dependence of the scattered radiation would differ from that of the Rayleigh phase function (see Chapter 7 for a discussion of such relativistic effects).

So, providing the stellar line is narrow so that, apart from the region within the direct line core, the direct and scattered fluxes can be separated then Eq. 2.53 provides a means of determining disc inclinations irrespective of their velocity profiles (again neglecting stellar rotational broadening). Note that there is no longer an ambiguity in determining  $i$  as in Eq. 2.34. It will be shown in Chapter 4 that Eq. 2.53 holds even when the Doppler redistribution due to scattering off thermal electrons is included.

### 3. Inversion of Thomson scattered spectropolarimetric line profiles to yield the velocity structure of rotating or expanding circumstellar discs

#### Summary

Using previous analytic expressions for the Stokes fluxes of a narrow line scattered in a moving disc, the cases of rotation only and expansion only are formulated as integral equations. These equations relate the density and gradient weighted disk bulk velocity distribution to the observed Stokes flux line profiles. It is shown how these equations can be solved analytically for the weighted velocity distributions and the system inclination, for exact data. In the case of real noisy data the analytic forms of the integral equations provide a convenient basis for methods of statistical inversion.

#### 3.1 Introduction

Inference of the density and velocity structure of rotating/expanding circumstellar discs/winds is of considerable interest in the understanding of stellar mass loss. High resolution line spectropolarimetry creates the possibility of diagnosing such envelope structure much more fully than broad band polarimetry or high resolution spectrometry alone since each element of the scattered spectropolarimetric profile picks out the element of the envelope with the appropriate Doppler shift and provides orientation information on it. This problem has been formulated in detail in the previous chapter for scattering of a finite width line in a flattened envelope. It was also shown how, in the case of a narrow stellar line scattered in a rotating or expanding flat disc with a simply parametrised density and velocity structure, it is possible to infer the system inclination and structure model parameters from the resulting spectropolarimetric line profile.

In this chapter the diagnostic technique is extended to general density and velocity structure functions for the cases of pure rotation and of pure expansion of flat axisymmetric envelopes. These will be applicable respectively to the cases of a disc supported by rotation (with expansion speed very much less than the rotation speed) and a flat wind with negligible rotation. The general case where rotation and expansion speeds are comparable has been analysed numerically in Sect. 2.4.3 for simple models of the velocity distribution. It appears, however, not to be amenable to any obvious inverse solution in the general case and its further consideration is deferred. The other simplification made in these papers is that line smearing by scattering off thermal electrons can be neglected – see Chapter 4 for thermal effects. The problems are cast in the form of integral equations for a single weighted velocity distribution function with the  $I$  and  $Q$  spectropolarimetric profiles as data functions, the equations also containing the system inclination  $i$  as an unknown parameter. It is shown that these integral equations have analytic solutions for the velocity structure function

and for  $i$ . These analytic solutions show that spectropolarimetric data are capable of yielding the envelope structure from exact data and provide a basis for development of regularised solution methods in the case of real noisy data.

### 3.2 Formulation of the integral equation

Following Chapter 2,  $F_0$  denotes the flux of the (unscattered) narrow stellar line and  $F_\nu$  the flux of the scattered line at frequency  $\nu$ . Defining  $f(\alpha) = \nu F_\nu / 4 F_0$  at relative wavelength shift  $\alpha = (\lambda - \lambda_0) / \lambda_0$ , where  $\lambda_0 = c / \nu_0$  is the original line wavelength, the expressions for the scattered line Stokes fluxes, measured with respect to the projection of the system axis on the sky, are, for the case of *pure disc rotation*,

$$\begin{Bmatrix} f_\nu^I(\alpha) \\ f_\nu^Q(\alpha) \\ f_\nu^U(\alpha) \end{Bmatrix} = \begin{Bmatrix} I_1(\alpha) + \sin^2 i I_2(\alpha) \\ I_1(\alpha) - (1 + \cos^2 i) I_2(\alpha) \\ 0 \end{Bmatrix}, \quad (3.1)$$

with the integral functions  $I_1(\alpha)$  and  $I_2(\alpha)$  given by,

$$\begin{Bmatrix} I_1(\alpha) \\ I_2(\alpha) \end{Bmatrix} = \int \frac{\sigma_0 \Sigma(x)}{x \beta_\phi(x) \sin i} \begin{Bmatrix} \left[ 1 - \left( \frac{\alpha}{\beta_\phi(x) \sin i} \right)^2 \right]^{-\frac{1}{2}} \\ \left[ 1 - \left( \frac{\alpha}{\beta_\phi(x) \sin i} \right)^2 \right]^{\frac{1}{2}} \end{Bmatrix} dx. \quad (3.2)$$

In the case of *pure disc expansion*,

$$\begin{Bmatrix} f_\nu^I(\alpha) \\ f_\nu^Q(\alpha) \\ f_\nu^U(\alpha) \end{Bmatrix} = \begin{Bmatrix} I_3(\alpha) + \sin^2 i I_4(\alpha) \\ I_3(\alpha) - (1 + \cos^2 i) I_4(\alpha) \\ 0 \end{Bmatrix}, \quad (3.3)$$

with

$$\begin{Bmatrix} I_3(\alpha) \\ I_4(\alpha) \end{Bmatrix} = \int \frac{\sigma_0 \Sigma(x)}{x \beta_r(x) \sqrt{\sin^2 i - (\alpha / \beta_r(x) - 1)^2}} \begin{Bmatrix} 1 \\ \frac{1}{\sin^2 i} (\alpha / \beta_r(x) - 1)^2 \end{Bmatrix} dx. \quad (3.4)$$

where it assumed assumed  $\beta_r \ll 1$ . Here  $\beta_\phi(x)$ ,  $\beta_r(x)$  are respectively the rotational and expansion speeds, in units of  $c$ , at distance  $r = R x$  from the star, radius  $R$ , and  $\Sigma(x)$  is the electron surface density ( $\text{m}^{-2}$ ) of the flat disc.

In Eqs. 3.1 and 3.2 the integral limits are over all  $x$  where  $\beta_\phi(x)$  is such that a Doppler shift occurs at some point on that circle shifting the line wavelength by  $\alpha \lambda_0$  for the observed  $\alpha$ , namely those  $x$  where,

$$\beta_\phi(x) \geq \frac{|\alpha|}{\sin i}. \quad (3.5)$$

Physically this is because the highest line of sight speed on the circle of radius  $x$  is  $\beta_\phi(x) \sin i$  and if Eq. 3.5 is not satisfied then the stellar line cannot be shifted by  $\alpha$  from any point on that circle.

In Eqs. 3.3 and 3.4 the integral limits on  $x$  are slightly more complicated. This is because in the case of expansion *all* stellar line photons are red-shifted when they encounter a scatterer at  $x$  by an amount  $\beta_r(x)$  and subsequently red or blue shifted in the observers frame after scattering by an amount in the range  $\pm\beta_r \sin i$ . The total shift is thus in the range  $\beta_r(1 \pm \sin i)$  and the integral limits on  $x$  for a specified  $\alpha$  are such that,

$$\frac{\alpha}{(1 + \sin i)} \leq \beta_r(x) \leq \frac{\alpha}{(1 - \sin i)} . \quad (3.6)$$

It is at once clear from the forms of Eqs. 3.1–3.4 that  $\Sigma(x)$  and  $\beta_\phi(x)$  or  $\beta_r(x)$  cannot be solved for individually from  $f^I(\alpha)$ ,  $f^Q(\alpha)$  since only the combination  $\Sigma(x)/x\beta(x)$  (where  $\beta$  is either the expansion or the rotation speed) occurs in the integrands, and since only  $\beta$  and not  $x$  occurs within the kernel functions. This is to be expected physically since redistribution of the scatterer function,  $\Sigma(x)/x$ , over  $x$ , but with the same  $\beta$ , can lead to the same scattered profile contribution at  $\alpha$ . The central property of the envelope in determining  $f^I(\alpha)$ ,  $f^Q(\alpha)$  is rather the “amount” of scattering in each range of  $\beta_\phi$  or  $\beta_r$ . This can be seen by defining the scattering optical depth  $\tau = \sigma_0 \Sigma$  through the disc at  $x$ , replacing  $x$  by  $\beta$  as the variable of integration and defining,

$$g(\beta) = \frac{\tau(x[\beta])}{x(\beta)\beta |d\beta/dx|} . \quad (3.7)$$

where  $|d\beta/dx|$  is assumed to be monotonic. This is certainly true for all likely  $\beta(x)$  (with  $|d\beta/dx| < 0$  in the case of rotation and  $|d\beta/dx| > 0$  in the case of expansion), but this assumption could be dropped by generalising the following to include summation of integrals over each element of the disc in which  $\beta$  is monotonic.

It can thus be seen that what determines the scattered line profiles in the two cases are functions  $g$  which are a kind of disc optical depth per unit speed ( $\beta$ ) range, weighted with respect to inverse distance (this is closely analogous to the role of differential emission measure in spectral problems – Craig & Brown (1986)). Denoting by  $g_\phi$ ,  $g_r$  the  $g$  functions for the rotation and expansion cases, the Stokes profile integrals in Eqs. 3.1–3.4 can now be expressed as,

$$f^I(\alpha) = \int_{|\alpha|/\sin i}^{\infty} \frac{g_\phi(\beta_\phi)}{\sin i} \frac{d\beta_\phi}{\sqrt{1 - (\alpha/\beta_\phi \sin i)^2}} + \sin^2 i \int_{|\alpha|/\sin i}^{\infty} \frac{g_\phi(\beta_\phi)}{\sin i} \sqrt{1 - (\alpha/\beta_\phi \sin i)^2} d\beta_\phi , \quad (3.8)$$

$$f^Q(\alpha) = \int_{|\alpha|/\sin i}^{\infty} \frac{g_\phi(\beta_\phi)}{\sin i} \frac{d\beta_\phi}{\sqrt{1 - (\alpha/\beta_\phi \sin i)^2}} - (1 + \cos^2 i) \int_{|\alpha|/\sin i}^{\infty} \frac{g_\phi(\beta_\phi)}{\sin i} \sqrt{1 - (\alpha/\beta_\phi \sin i)^2} d\beta_\phi , \quad (3.9)$$

for the rotation problem, and,

$$f^I(\alpha) = \int_{\alpha/(1+\sin i)}^{\alpha/(1-\sin i)} \frac{g_r(\beta_r) d\beta_r}{\sqrt{\sin^2 i - (\alpha/\beta_r - 1)^2}} - \int_{\alpha/(1+\sin i)}^{\alpha/(1-\sin i)} \frac{g_r(\beta_r) [\alpha/\beta_r - 1]^2}{\sqrt{\sin^2 i - (\alpha/\beta_r - 1)^2}} d\beta_r , \quad (3.10)$$

$$f^I(\alpha) = \int_{\alpha/(1+\sin i)}^{\alpha/(1-\sin i)} \frac{g_r(\beta_r) d\beta_r}{\sqrt{\sin^2 i - (\alpha/\beta_r - 1)^2}} - \frac{1 + \cos^2 i}{\sin^2 i} \int_{\alpha/(1+\sin i)}^{\alpha/(1-\sin i)} \frac{g_r(\beta_r) [\alpha/\beta_r - 1]^2}{\sqrt{\sin^2 i - (\alpha/\beta_r - 1)^2}} d\beta_r , \quad (3.11)$$

for the expansion problem.

Note that in all of these integrals, Eqs. 3.8–3.11, the  $\beta$  limits may in practice be replaced (for some  $\alpha$ ) by maximum or minimum  $\beta$ 's in the envelope itself. This possibility is, however, incorporated in Eqs. 3.8–3.11 since it corresponds to having  $g(\beta) = 0$  for  $\beta < \beta_{\min}$ ,  $\beta > \beta_{\max}$ . Should such a cut-off feature be present in  $g(\beta)$  then it will automatically appear in solution of the equations for the corresponding  $f(\alpha)$ .

Equations 3.8–3.11 can now be recognised as integral equations to be solved for  $g_\phi(\beta_\phi)$  or  $g_r(\beta_r)$  from data functions  $f^I(\alpha)$  and  $f^Q(\alpha)$ . Solution also requires, however, determination of  $i$ . This can be done because each of the problems is in fact overdetermined providing two functional equations for only one unknown function  $g(\beta)$  and one unknown parameter  $i$ . Note, however, that observation of the scattered spectrometric intensity profile  $f^I(\alpha)$  alone is *not* sufficient to allow solution for  $g(\beta)$  and  $i$  since the problem is underdetermined. Spectropolarimetry is thus the key allowing complete solution of the problem.

Once  $i$  is found one may thus, in principle, use either of the integral equations (3.8 or 3.9 for the rotation case, 3.10 or 3.11 for the expansion case) to find  $g_\phi(\beta_\phi)$ ,  $g_r(\beta_r)$ . (In the practical case of noisy data one would, however, utilise both equations to yield the optimal numerical solution.) Before considering solution of the integral equations it is first shown how  $i$  can be determined.

### 3.3 Determination of disc inclination

#### 3.3.1 Rotating disc

It is seen from Eqs. 3.8 and 3.9 that, for any particular  $\alpha$ , the ratio  $f^Q/f^I$  depends only on  $i$  and on the ratio of two integrals over  $g_\phi(\beta_\phi)$ . If the ratio of the integrals for any particular  $\alpha$  can be found then the ratio  $f^Q/f^I$  should allow  $i$  to be determined. The most obvious choice is to choose  $\alpha \approx 0$  – in practice this will mean  $\alpha$  as small as possible while still outwith the profile of the direct unscattered stellar line. Then,

$$f^I(0) = \frac{1}{\sin i} \int_0^\infty g_\phi(\beta_\phi) d\beta_\phi + \sin i \int_0^\infty g_\phi(\beta_\phi) d\beta_\phi, \quad (3.12)$$

$$f^Q(0) = \frac{1}{\sin i} \int_0^\infty g_\phi(\beta_\phi) d\beta_\phi - \frac{1 + \cos^2 i}{\sin i} \int_0^\infty g_\phi(\beta_\phi) d\beta_\phi, \quad (3.13)$$

so that,

$$\frac{\cos^2 i}{1 + \sin^2 i} = -\frac{f^Q(0)}{f^I(0)}, \quad (3.14)$$

which yields  $i$  from the data. This is exactly the same result as found in Chapter 2 for a particular parametrisation for  $\beta_\phi(x)$ ,  $\Sigma(x)$  and with the same physical explanation. That is,  $\alpha = 0$  corresponds to scattering on a line in the disc in the plane containing the observer and the disc axis,

along which the scattering angle is either  $\pi/2 - i$  or  $\pi/2 + i$  and the ratio of the scattered total to polarised flux is a function of  $i$  only.

A more robust way to find  $i$ , minimising the effect of uncertainty of  $f(\alpha)$  near  $\alpha = 0$ , is to consider the total fluxes under the scattered profiles - i.e.  $F = \int_{-\infty}^{\infty} f(\alpha) d\alpha$  - as in Chapter 2. By Eqs 3.8 and 3.9 these reduce, on reversing the order of integration and changing the inner variable from  $\alpha$  to  $\alpha/\beta \sin i$ , to,

$$F^I = \int_{-\infty}^{\infty} f^I(\alpha) d\alpha = \pi \int_0^{\infty} g_{\phi}(\beta_{\phi}) d\beta_{\phi} + \frac{\pi \sin^2 i}{2} \int_0^{\infty} g_{\phi}(\beta_{\phi}) d\beta_{\phi}, \quad (3.15)$$

$$F^Q = \int_{-\infty}^{\infty} f^Q(\alpha) d\alpha = \pi \int_0^{\infty} g_{\phi}(\beta_{\phi}) d\beta_{\phi} - \frac{\pi(1 + \cos^2 i)}{2} \int_0^{\infty} g_{\phi}(\beta_{\phi}) d\beta_{\phi}, \quad (3.16)$$

so that,

$$\frac{\sin^2 i}{2 + \sin^2 i} = \frac{F^Q}{F^I}, \quad (3.17)$$

from which  $i$  can be found. This result should be reliable since the integral quantities  $F^I$ ,  $F^Q$  are better determined than  $f^I$ ,  $f^Q$  and will only be slightly in error when a small region near  $\alpha = 0$  (containing the direct stellar line) is omitted in the integrals.

### 3.3.4 Expanding discs

Since all points on an expanding disc produce a redshift of scattered stellar radiation there is no plane corresponding to  $\alpha = 0$  as in the case of rotation above. If there exists a finite maximum or minimum value of  $\beta$  the corresponding extremes in  $\alpha$  might be useable to determine  $i$  similarly to the first method above. However, without any such conditions,  $i$  can always be found for an expanding disc as in the second method above - i.e. by considering  $F^I$ ,  $F^Q$ . Integrating Eqs. 3.10 and 3.11 over all  $\alpha$  and taking the ratio then yields,

$$\frac{F^Q}{F^I} = \frac{1 - R(1 + \cos^2 i)}{1 + R \sin^2 i}, \quad (3.18)$$

where, with the integral order reversed,

$$R = \frac{I_4}{I_3} = \frac{\frac{1}{\sin^2 i} \int_0^{\infty} \beta_r g_r(\beta_r) \int_{\beta_r(1-\sin i)}^{\beta_r(1+\sin i)} \frac{(\alpha/\beta_r - 1)^2 d\alpha d\beta_r}{\sqrt{(\beta_r(1+\sin i) - \alpha)(\alpha - \beta_r(1-\sin i))}}}{\int_0^{\infty} \beta_r g_r(\beta_r) \int_{\beta_r(1-\sin i)}^{\beta_r(1+\sin i)} \frac{d\alpha d\beta_r}{\sqrt{(\beta_r(1+\sin i) - \alpha)(\alpha - \beta_r(1-\sin i))}}}. \quad (3.19)$$

By the change of variable  $\sin \theta = (\alpha/\beta_r - 1)/\sin i$  the inner integral in the denominator of Eq. 3.19 is found to be simply  $\pi$  and that in the numerator to be  $\pi \sin^2 i/2$ , both independent of  $\beta$ . Thus  $\int_0^{\infty} \beta_r g_r(\beta_r) d\beta_r$  cancels from the ratio  $R$  and Eq. 3.18 yields,

$$\frac{\sin^2 i}{2 + \sin^2 i} = \frac{F^Q}{F^I}, \quad (3.20)$$

exactly as for the rotation case Eq. 3.17.

### 3.4. Solution of the integral equations

#### 3.4.1 Rotating disc

Given  $i$  from Sect. 3.1 then in principle either Eq. 3.8 or Eq. 3.9 can be solved to find  $g_\phi(\beta_\phi)$  or, for real data, perform a joint numerical solution to give the best fit to both  $f^I(\alpha)$  and  $f^Q(\alpha)$ . Here the possibility of solution is demonstrated by considering a single integral equation. The most convenient form to consider is for the combination of data,

$$2f(\alpha) = (1 + \cos^2 i) f^I(\alpha) + \sin^2 i f^Q(\alpha), \quad (3.21)$$

which, by Eqs. 3.8 and 3.9, satisfies,

$$f(\alpha) = \int_{\alpha/\sin i}^{\infty} \frac{g_\phi(\beta_\phi) d\beta_\phi}{\sqrt{\sin^2 i - (\alpha/\beta_\phi)^2}}. \quad (3.22)$$

Integral equation 3.22 can be solved by a number of methods. Defining  $\xi = \sin^2 i/\alpha^2$ ,  $\eta = \beta_\phi^{-2}$ ,  $\psi(\xi) = f(\sin i/\sqrt{\xi}) \sin i/\sqrt{\xi}$  and  $\varphi(\eta) = g_\phi(\eta^{-1/2})/2\eta^{3/2}$  the equation becomes,

$$\psi(\xi) = \int_0^\xi \frac{\varphi(\eta)}{\sqrt{\xi - \eta}} d\eta, \quad (3.23)$$

which is Abel's equation with solution (e.g. Sneddon, 1972).

$$\varphi(\eta) = \frac{1}{\pi} \frac{d}{d\eta} \int_0^\eta \frac{\psi(\xi)}{\sqrt{\eta - \xi}} d\xi, \quad (3.24)$$

or, in terms of the original variables,

$$g_\phi(\beta_\phi) = \frac{-4 \sin i}{\pi} \frac{d}{d\beta_\phi} \left[ \beta_\phi \int_{\beta_\phi}^{\infty} \frac{f(\alpha) d\alpha}{\alpha \sqrt{\beta^2 - \alpha^2/\sin^2 i}} \right]. \quad (3.25)$$

In a real situation differentiation of data may be impossible because of noise amplification (Craig & Brown, 1986) and a regularised (smoothed) solution will be required. One convenient way to achieve this is by singular value decomposition. For kernels which depend only on the ratio of the variables, as in the kernel of Eq. 3.22 which contains only  $\alpha/\beta_\phi$ , the singular functions can be found by taking the Mellin transform,

$$M\{f(x); s\} = f(s) = \int_0^\infty f(x) x^{s-1} dx. \quad (3.26)$$

Taking the Mellin transform of Eq. 3.22 yields.

$$g_\phi(\beta_\phi) = \frac{1}{\beta} M^{-1} \left\{ \frac{\hat{f}(s)}{\sin^{s-1} i \int_0^1 y^{s-1}/\sqrt{1-y^2} dy}; \beta_\phi \right\}, \quad (3.27)$$

as solution. This is clearly related to the solution of Eq. 3.22 in terms of integral moments. Defining,

$$\{f\}_j = \int_0^\infty f(x) x^j dx, \quad (3.28)$$

then from Eq. 3.22 the following relation between the moments of  $f(\alpha)$  and  $g(\alpha)$  is obtained,

$$\{g_\phi\}_j = \frac{\{f\}_{j-1}}{\sin^{j-1} i B\left(\frac{j-1}{2}, \frac{1}{2}\right)}, \quad (3.29)$$

where  $B$  is the beta function.

### 3.4.2 Expanding disc

Constructing  $f(\alpha)$  as in Eq. 3.21 gives from Eqs. 3.10 and 3.11 one of the integral equations for the expansion problem, viz,

$$f(\alpha) = \int_{\alpha/(1+\sin i)}^{\alpha/(1-\sin i)} \frac{g_r(\beta_r) d\beta_r}{\sqrt{\sin^2 i - (\alpha/\beta_r - 1)^2}}. \quad (3.30)$$

Though this equation is close in form to Abel's equation, the kernel singularity at both limits seems to preclude an explicit solution like Eq. 3.25 in terms of integral and differential operators on  $f(\alpha)$ . As in Eq. 3.22, however, the kernel of Eq. 30 depends only on  $\alpha/\beta_r$  so that solution is again possible via the Mellin transform. After some manipulation the Mellin solution here is,

$$g_r(\beta_r) = \frac{1}{\beta_r} M^{-1} \left\{ \frac{f(s)}{\int_{-\sin i}^{\sin i} (1 + y \sin i)^{s-1} / \sqrt{1-y^2} dy}; \beta_r \right\}. \quad (3.31)$$

Also, similarly to Eq. 29 the integral moments of  $g_r(\beta_r)$  may be related to those of  $f(\alpha)$ , namely,

$$\{g\}_j = \{f\}_{j-1} / \int_{-\sin i}^{\sin i} \frac{(1 + y \sin i)^j}{\sqrt{1-y^2}} dy. \quad (3.32)$$

### 3.5 Interpretation of the solutions

By Eq. 3.27  $g_\phi(\beta_\phi)$  can be inferred and from Eq. 3.31  $g_r(\beta_r)$ , but these functions are combinations of the functions  $\beta \Sigma(x)$  and  $\beta_\phi(x)$  or  $\beta_r(x)$  as given by Eq. 3.7. Without model assumptions these are all that can be inferred from spectropolarimetric line profiles. However, rotating discs generally have a known velocity structure given either by the Keplerian law,

$$\beta_\phi(x) = \beta_1 x^{-\frac{1}{2}}, \quad (3.33)$$

or, for a viscous disc,

$$\beta_\phi(x) = \beta_1 x^{-\delta}, \quad (3.34)$$

where  $\delta$  is a constant and  $\beta_1$  is the value at  $x = 1$ . Substituting Eq. 3.34 in Eq. 3.7 then gives for the disc density structure,

$$\Sigma(x) = \sigma_0 \delta x^{-2\delta} \beta_1^2 g_\phi(\beta_1 x^{-\delta}) . \quad (3.35)$$

In the case of expansion the density structure  $\Sigma(x)$  is related to the velocity structure  $\beta_r(x)$ , if a steady 2-D continuity equation is assumed, by,

$$\Sigma(x) = \frac{\Sigma_1}{x \beta_r(x)} , \quad (3.36)$$

so that Eq. 3.7 becomes,

$$g_r(\beta_r) = \frac{\sigma_0 \Sigma_1}{x \beta_r^2 d\beta_r/dx} , \quad (3.37)$$

where it is assumed that  $d\beta_r/dx \geq 0$ . Consequently  $\beta_r(x)$  can be recovered by integrating,

$$g_r(\beta_r) \beta_r^2 \frac{d\beta_r}{dx} = \frac{\sigma_0 \Sigma_1}{x} , \quad (3.38)$$

or,

$$x(\beta_r) = \exp \frac{1}{\sigma_0 \Sigma} \int_{\beta_1}^{\beta_r} g_r \beta_r^2 d\beta_r , \quad (3.39)$$

where  $g_r(\beta_r)$  is given by Eq. 3.31.

### 3.6 Conclusions

The theoretical analysis of this chapter has demonstrated the possibility of determining the structure of rotating or expanding circumstellar discs from analysis of exact data of scattered spectropolarimetric line profiles. Clearly real data of this type is subject to considerable noise and is undersampled in the wavelength domain – Sect 2.2 – which may yield large errors in the recovered solutions. As is discussed in Chapter 6, the procedures for analysing noisy data can be very complex and are not discussed in detail in this thesis. However, it should be noted that the properties of the inverse solutions presented in this chapter – Abel's Equation and the Mellin Transform – have been investigated for the effects of noisy data. The Abel equation turns out to be fairly robust and its application to noisy data can be treated with standard numerical techniques (Craig & Brown), but the Mellin transform is not as stable.

As was stated previously the integral equations relating the spectropolarimetric line profiles to the disc structure may be solved by numerical techniques alone – such as matrix inversion, but the existence of analytic solutions, albeit only for the rotation and expansion cases individually, illustrates further the diagnostic potential of spectropolarimetric line data.

#### 4. Effect of electron thermal motions on Thomson scattered line profiles from hot circumstellar envelopes

##### Summary

This chapter presents the theory which describes the Doppler frequency redistribution for the scattering of unpolarised radiation off electrons which are in random (Maxwellian) thermal motion. The theory is then applied to the scattering of stellar radiation in isothermal circumstellar discs which may also have a bulk velocity component.

##### 4.1 Introduction

In the single scattering treatment presented in Chapter 2, no consideration was given to the smearing effect caused by the Doppler redistribution of scattered radiation due to the random thermal motions of the scattering electrons. The analysis was applied to scattering in the discs of Be stars where typical bulk velocities are a few hundred  $\text{km.s}^{-1}$  and typical temperatures are  $\sim 10^4\text{K}$ , at which the average electron thermal velocity is  $\sim 400 \text{ km.s}^{-1}$ . Since, for Be stars, the bulk and thermal velocities of electrons are of the same order the analysis should be extended to account for this thermal smearing.

In what follows, the effect of thermal smearing on the scattered Stokes fluxes is determined using a treatment originally formulated by Dirac (1925) and applied by Munch (1947) to illustrate the line broadening effect of scattering off electrons in thermal motion in a plane parallel atmosphere. Sen and Lee (1960) applied the same approach to calculate the emergent polarisation of initially unpolarised line radiation after multiple Thomson scattering and their analysis predicted variations across the line in the degree of polarisation of up to 5%. This variation is not observed and the discrepancy of their results with observations may be attributed to the fact that Dirac's analysis is valid only for scattering of unpolarised radiation, i.e. in calculating the emergent polarisation this treatment should only be applied in the single scattering case, since the incident radiation for subsequent scatterings will be polarised.

##### 4.2 Theory

When calculating the polarisation of scattered radiation the scattering "redistribution function" is used which determines the degree of polarisation of radiation scattered into a certain direction with a certain frequency. The redistribution function is, in general, a function of frequency and scattering angle, the angle between the incident and scattered radiation. For Thomson scattering off stationary electrons the phase function is frequency independent, i.e. incident and scattered radiation have the same frequency. However, when the electron is in motion there is a Doppler

redistribution in frequency which must be taken into account. In Chapter 2 this redistribution was incorporated directly into the frequency dependent expressions for the scattered radiation – the bulk velocity field of the scattering region was specified and the Doppler shifts arising from the bulk motion of the electrons with respect to the source and the observer varied only from point to point in the scattering region. This approach cannot be applied when the electrons are in thermal motion since there is a distribution of velocities *at each point* and thus a local averaging procedure must be employed. This was investigated by Dirac (1925) where he assumed that the electron thermal velocity could be specified by the classical Maxwellian distribution. Dirac's analysis, which is summarised here, resulted in an expression for the frequency redistribution of scattered radiation, which was initially unpolarised, in terms of the electron temperature, the scattering angle and the incident and scattered frequencies.

In Chapter 2 the frequency redistribution for scattering radiation off electrons in bulk motion was described by Eq. 2.1. The complete form of this equation, incorporating the quantum Compton wavelength shift, for scattering off electrons with momenta  $\mathbf{p} = (p_x, p_y, p_z)$  is,

$$(m_e c - p_x) \frac{\nu_*}{\nu} - (m_e c - p_x \cos \Theta - p_y \sin \Theta) = \frac{h \nu_*}{c} (1 - \cos \Theta), \quad (4.1)$$

where  $\Theta$  is the scattering angle for radiation incident in the  $x$  direction and scattered in the  $x$ - $y$  plane. The term on the right hand side of Eq. 3.1 is the quantum mechanical Compton wavelength shift. In a classical approximation this term can be ignored and for  $\mathbf{p} \ll m_e c$  this equation reduces to,

$$(1 - \cos \Theta) p_x - p_y \sin \Theta = m_e c (\nu_*/\nu - 1). \quad (4.2)$$

In Dirac's treatment he considered the frequency redistribution of radiation scattered off electrons whose momenta were specified by the classical Maxwellian distribution function such that in a mass  $dm$  there are,

$$dm \frac{N}{(2 \pi m_e k T)^{\frac{3}{2}}} e^{-(p_x^2 + p_y^2 + p_z^2)/2 m_e k T} dp_x dp_y dp_z, \quad (4.3)$$

electrons with momenta in the range  $(p_x, p_y, p_z)$  to  $(p_x + dp_x, p_y + dp_y, p_z + dp_z)$ , with  $N$  the number of electrons per unit mass. This mass of electrons will scatter radiation incident from direction  $\hat{\mathbf{k}}_*$  with frequency  $\nu_*$  into direction  $\hat{\mathbf{k}}$  with frequency  $\nu$ . However, not all incident and scattered frequencies and electron momenta are arbitrary, but must be related in accordance with Eq. 4.2 as follows. Suppose radiation has been scattered from solid angle  $d\Omega_*$  about direction  $\hat{\mathbf{k}}_*$  and is observed with a frequency in the range  $\nu$  to  $\nu + d\nu$  in the solid angle  $d\Omega$  about the direction  $\hat{\mathbf{k}}$ . With these parameters fixed then  $dp_x, dp_y, dp_z$  and the incident frequency  $\nu_*$  must be related via Eq. 4.2 before integrating over all possible electron momenta. Due to the formulation of the problem – scattering in the  $x$ - $y$  plane –  $p_z$  may be integrated over directly since its value does

not effect the scattered frequency - cf Eqs. 4.1 and 4.2. Writing  $dp_x$  as  $(\partial p_x / \partial \nu_*) d\nu_*$ , then the radiant energy scattered by the thermal electrons from  $(\nu_*, \hat{\mathbf{k}}_*)$  to  $(\nu, \hat{\mathbf{k}})$  is,

$$\sigma_T I_{\nu_*} dm d\nu_* d\nu d\Omega_* \frac{d\Omega}{4\pi} dt g(\hat{\mathbf{k}}_*; \hat{\mathbf{k}}) \frac{N}{(2\pi m_e k T)^{\frac{3}{2}}} \int_{-\infty}^{\infty} \int_{-\infty}^{\infty} e^{-(p_x^2 + p_y^2 + p_z^2)/2 m_e k T} \frac{\partial p_x}{\partial \nu_*} dp_y dp_z, \quad (4.4)$$

where  $g(\hat{\mathbf{k}}_*; \hat{\mathbf{k}})$  is the Rayleigh phase function. Comparing this with Eq. 3.5 the redistribution function  $R$  may be written as the product of the Rayleigh phase function and a thermal frequency redistribution function viz,

$$R(\nu_*, \hat{\mathbf{k}}_*; \nu, \hat{\mathbf{k}}) = g(\hat{\mathbf{k}}_*; \hat{\mathbf{k}}) \psi(\nu_*, \nu), \quad (4.5)$$

where

$$\psi(\nu_*, \nu) = \frac{1}{(2\pi m_e k T)^{\frac{3}{2}}} \int_{-\infty}^{\infty} \int_{-\infty}^{\infty} \exp -(p_x^2 + p_y^2 + p_z^2)/2 m_e k T \frac{\partial p_x}{\partial \nu_*} dp_y dp_z. \quad (4.6)$$

From Eq. 4.2  $\partial p_x / \partial \nu_*$  and  $p_x^2 + p_y^2$  are

$$\frac{\partial p_x}{\partial \nu_*} = \frac{m_e c}{\nu(1 - \cos \Theta)}, \quad p_x^2 + p_y^2 = \frac{2}{(1 - \cos \Theta)} \left[ p_y + \frac{m_e c (\nu_* - \nu) \sin \Theta}{2\nu(1 - \cos \Theta)} \right]^2 + \frac{m_e^2 c^2 (\nu_* - \nu)^2}{2\nu^2(1 - \cos \Theta)}. \quad (4.7)$$

which allows Eq. 4.6 to be written as,

$$\psi(\nu_*, \nu) = \left[ \frac{m_e c^2}{4\pi k T \nu^2 (1 - \cos \Theta)} \right]^{\frac{1}{2}} \exp \left[ -\frac{m_e c^2}{4kT(1 - \cos \Theta)} \left( \frac{\nu_* - \nu}{\nu} \right)^2 \right]. \quad (4.8)$$

This then is the frequency redistribution function for scattering radiation off a Maxwellian distribution of electrons at temperature  $T$ . When the temperature tends to zero the redistribution function for Thomson scattering off stationary electrons is retrieved -  $\psi(\nu_*, \nu) = \delta(\nu_* - \nu)$ . Note that  $\psi(\nu_*, \nu)$  could have been derived by relating  $p_y$  and  $\nu_*$  - i.e.  $dp_y = (\partial p_y / \partial \nu_*) d\nu_*$  and integrating over  $p_x$ .

It is to be noted that this does not possess the same symmetries as the Rayleigh phase function which is equal for radiation scattered through  $\Theta$  or  $\pi - \Theta$ . Instead the Maxwellian frequency redistribution for radiation scattered through  $\pi - \Theta$  is greater than that for radiation scattered through  $\Theta$  which can be explained by considering the scattering properties of a volume of thermal electrons. In such a volume as many electrons are likely to be approaching the incident photon as there are electrons receding from it. Consider now the case of two incident photons, which are undeviated from their original direction after scattering ( $\Theta = 0^\circ$ ), one scattering off the approaching, the other off the receding electron. From Eq. 2.1 it is clear that these photons will be scattered with a frequency equal to the incident frequency since the two Doppler shifts described by this equation exactly cancel. However, for photons which are backscattered,  $\Theta = 180^\circ$ , the photon which scatters off the receding electron will have a net redshift,  $1/(1 - \beta)$ , while the other photon will be observed with a net blue-shift,  $1/(1 + \beta)$ , such that the mean energy,  $\sim [1/(1 + \beta) + 1/(1 - \beta)]/2$ ,

of these two photons is greater, by a factor  $1/(1-\beta^2)$ , than that of the undeviated photons. Hence radiation which is backscattered from a volume of thermal electrons will be of greater intensity than that which is forward scattered – this is incorporated in the mathematical form for the thermal redistribution function in Eq. 4.8. As will be illustrated in Sect. 4.6 when bulk and thermal velocities are considered this asymmetry of the redistribution function can yield position angle changes within scattered spectral lines where no changes occur when bulk or thermal motions are considered separately.

Following the analysis set out earlier and incorporating Dirac's local frequency redistribution, the Stokes vector flux,  $\mathbf{F}_\nu$ , of radiation Thomson scattered off hot electrons may now be written as,

$$\mathbf{F}_\nu = \frac{3\sigma_T}{16\pi D^2} \int_V \int_{\Omega_*} \int_0^\infty n I_{\nu_*} \mathbf{P} \psi(\nu_*, \nu) d\nu_* d\Omega_* dV, \quad (4.9)$$

where  $\mathbf{P}$  is the Rayleigh phase vector of Eq. 1.23. The right hand side of this equation may be transformed into wavelength space ( $\lambda_* = c/\nu_*$ ) to give,

$$\mathbf{F}_\nu(\lambda) = \frac{3\sigma_T}{16\pi D^2} \int_V \int_{\Omega_*} \int_0^\infty n I_{\nu_*}(\lambda_*) \mathbf{P} \psi(\lambda_*, \lambda) d\lambda_* d\Omega_* dV, \quad (4.10)$$

where the thermal wavelength redistribution function is,

$$\psi(\lambda_*, \lambda) = \left[ \frac{m_e c^2}{4\pi k T \lambda^2 (1 - \cos \Theta)} \right]^{\frac{1}{2}} \exp \left[ -\frac{m_e c^2}{4k T (1 - \cos \Theta)} \left( \frac{\lambda_* - \lambda}{\lambda_*} \right)^2 \right]. \quad (4.11)$$

For  $\lambda_* = 5000\text{\AA}$  and a temperature of  $10^4\text{K}$  this thermal smearing function has a "width" of about  $10\text{\AA}$ .

Using the same assumptions as Munch it is convenient to replace  $\lambda_*$  and  $\lambda$  by a constant wavelength,  $\lambda_0$  – e.g. line "centre" – except where the difference  $(\lambda_* - \lambda)$  is involved and extend the range of  $(\lambda_* - \lambda)$  from  $-\infty$  to  $\infty$ . On making the substitutions,

$$\xi = \left( \frac{m_e c^2}{4k T} \right)^{\frac{1}{2}} \left( \frac{\lambda - \lambda_0}{\lambda_0} \right), \quad \xi_* = \left( \frac{m_e c^2}{4k T} \right)^{\frac{1}{2}} \left( \frac{\lambda_* - \lambda_0}{\lambda_0} \right), \quad (4.12)$$

Eq. 4.10 becomes,

$$\mathbf{F}_\nu(\xi) = \frac{3\sigma_T}{16\pi D^2} \int_V \int_{\Omega_*} \int_{-\infty}^\infty n \mathbf{P} I_{\nu_*}(\xi_*) \psi(\xi_* - \xi) d\xi_* d\Omega_* dV, \quad (4.13)$$

where,

$$\psi(\xi_* - \xi) = \frac{\exp \frac{-(\xi_* - \xi)^2}{(1 - \cos \Theta)}}{\sqrt{\pi(1 - \cos \Theta)}}. \quad (4.14)$$

Note that the substitutions made in Eq. 4.12 are only valid if the scattering region is isothermal with no bulk velocity component.

Specific forms of the incident stellar radiation field shall now be investigated.

### 4.3 Continuum polarisation

When investigating processes such as Doppler redistributions, whose effects are most pronounced over bandpasses where the radiation field varies rapidly with wavelength it is convenient to assume wavelength independence of a slowly varying continuum radiation field. In the case of thermal smearing this is a valid assumption since the width of the thermal smearing function is typically tens of angstroms and thus will only have a significant effect on the wavelength redistribution of scattered radiation when the incident intensity is a rapidly varying function of wavelength. Therefore,  $I_{\nu_*}$  is set equal to a constant,  $I_0$ , and the Stokes fluxes are,

$$\mathbf{F}_\nu(\xi) = \frac{3\sigma_T}{16\pi} I_0 \int_V \int_{\Omega_*} \int_{-\infty}^{\infty} n \psi(\xi_* - \xi) d\xi_* \mathbf{P} d\Omega_* dV. \quad (4.15)$$

Due to the normalisation properties of the thermal redistribution function integrating this equation over  $\xi_*$  yields,

$$\mathbf{F}_\nu(\xi) = \frac{3\sigma_T I_0}{16\pi} \int_V \int_{\Omega_*} n \mathbf{P} d\Omega_* dV, \quad (4.16)$$

This result is the same as the analysis presented in Chapter 1 and shows that, under the assumption of a slowly varying incident continuum radiation field, the continuum polarisation of Thomson scattered starlight is unaffected by electron thermal motions.

Attention is now focussed on the scattering of line radiation in an isothermal planar disc, in which case variations in the incident radiation field occur over wavelength ranges which are comparable to, or smaller than, the width of the thermal smearing function. The scattering geometry for a planar disc allows the scattering angle  $\Theta$  to be expressed in terms of the inclination,  $i$ , and the disc polar coordinate,  $\phi$ , thus,

$$\cos \Theta = \sin i \cos \phi.$$

### 4.4 Monochromatic point source

Here the case of an infinitely sharp emission line centred at  $\xi_*$  is considered, i.e.  $I_{\nu_*} = I_0 \delta(\xi_*)$ . Inserting this form for the incident radiation field reduces Eq. 4.13 (for a point source and planar disc) to,

$$\begin{Bmatrix} F_\nu^I(\xi) \\ F_\nu^Q(\xi) \\ F_\nu^U(\xi) \end{Bmatrix} = 2\sigma_0 F_0 \int \frac{\Sigma(r)}{r} dr \begin{Bmatrix} (1 + \sin^2 i) I_8 - \sin^2 i I_9 \\ -\cos^2 i I_8 + (1 + \cos^2 i) I_9 \\ \cos i I_{10} \end{Bmatrix}, \quad (4.17)$$

where the integrals  $I_8$ ,  $I_9$ , and  $I_{10}$  are,

$$\begin{Bmatrix} I_8(\xi) \\ I_9(\xi) \\ I_{10}(\xi) \end{Bmatrix} = \int_0^{2\pi} \frac{\exp\left[\frac{-\xi^2}{1 - \sin i \cos \phi}\right]}{\sqrt{\pi(1 - \sin i \cos \phi)}} \begin{Bmatrix} 1 \\ \sin^2 \phi \\ \sin 2\phi \end{Bmatrix} d\phi. \quad (4.18)$$

From symmetry considerations  $I_{10}$  is zero for all  $\xi$ , hence the scattered  $U$  flux is zero. This result is not as obvious as it may appear due to the asymmetry of the thermal redistribution function and is explained as follows. For scattering stellar radiation in a stationary disc without any frequency redistribution the observed polarisation vectors at each point on the disc are perpendicular to radial lines from the star (considered to be a point source). When summed over the entire disc the  $U$  component of each polarisation vector at polar coordinate  $(r, \phi)$  will cancel with the  $U$  component of the polarisation vector at  $(r, \pi - \phi)$  or  $(r, -\phi)$  yielding a zero net Stokes  $U$  flux. Due to the symmetry properties of the Rayleigh phase function each polarisation vector may be "paired" with either one of the two polarisation vectors of the same magnitude, but opposite  $U$  - i.e. there is a double antisymmetry. This possible pairing with two other polarisation vectors does not occur when frequency redistribution due to electron thermal velocities is considered. Since the thermal redistribution function "favours" backscattered radiation the  $U$  component of a polarisation vector from the back half of the disc,  $(r, \phi)$  will not entirely cancel with the  $U$  component of the polarisation vector which is at  $(r, \pi - \phi)$  on the front half of the disc, but will cancel with the  $U$  component of the polarisation vector which is on the back half of the disc at  $(r, -\phi)$  - i.e. there is still a single antisymmetry. Pairing off the polarisation vectors in this way will thus yield a net zero  $U$  component. Note that inclusion of occultation effects will not yield any  $U$  component of the scattered flux since occultation will remove polarised flux from the rear of the disc where the  $(r, \phi)$ - $(r, -\phi)$  pairings occur and hence the scattered  $U$  flux will average to zero over the occulted and visible regions of the disc.

Analytic solutions for  $I_8$  and  $I_9$  can only be found for the following cases. When  $i = 0$  the integrals reduce to

$$\begin{Bmatrix} I_8(\xi) \\ I_9(\xi) \end{Bmatrix} = \begin{Bmatrix} \frac{2}{\sqrt{\pi}} \\ \frac{1}{\sqrt{\pi}} \end{Bmatrix} e^{-\xi^2}, \quad (4.19)$$

while for  $i = \pi/2$ , on making the substitution  $y = (\xi)^2/(1 - \cos \phi)$ , the solutions are,

$$\begin{Bmatrix} I_8(\xi) \\ I_9(\xi) \end{Bmatrix} = \begin{Bmatrix} \frac{1}{\sqrt{2\pi}} K_0(\xi^2/4) \\ 2\xi W_{-1,0}(\xi^2/2) \end{Bmatrix} e^{-\xi^2/4}, \quad (4.20)$$

where  $K_0$  is a Bessel function and  $W_{-1,0}$  is the Whittaker function (Gradshteyn & Ryhzik, 1963). When  $i = 0$  the Stokes  $Q$  flux in Eq. 4.18 is zero (as expected for an axisymmetric disc viewed pole-on) and the scattered total flux is,

$$F_\nu^I(\xi) = \frac{4\sigma_0 F_0}{\sqrt{2\pi}} e^{-\xi^2}, \quad (4.21)$$

For  $i = \pi/2$  the scattered Stokes fluxes are,

$$\begin{Bmatrix} F_\nu^I(\xi) \\ F_\nu^Q(\xi) \\ F_\nu^U(\xi) \end{Bmatrix} = 4\sigma_0 F_0 e^{-\frac{\xi^2}{4}} \begin{Bmatrix} \frac{1}{\sqrt{2\pi}} K_0(\xi^2/4) - \xi W_{-1,0}(\xi^2/2) \\ \xi W_{-1,0}(\xi^2/2) \\ 0 \end{Bmatrix}. \quad (4.22)$$

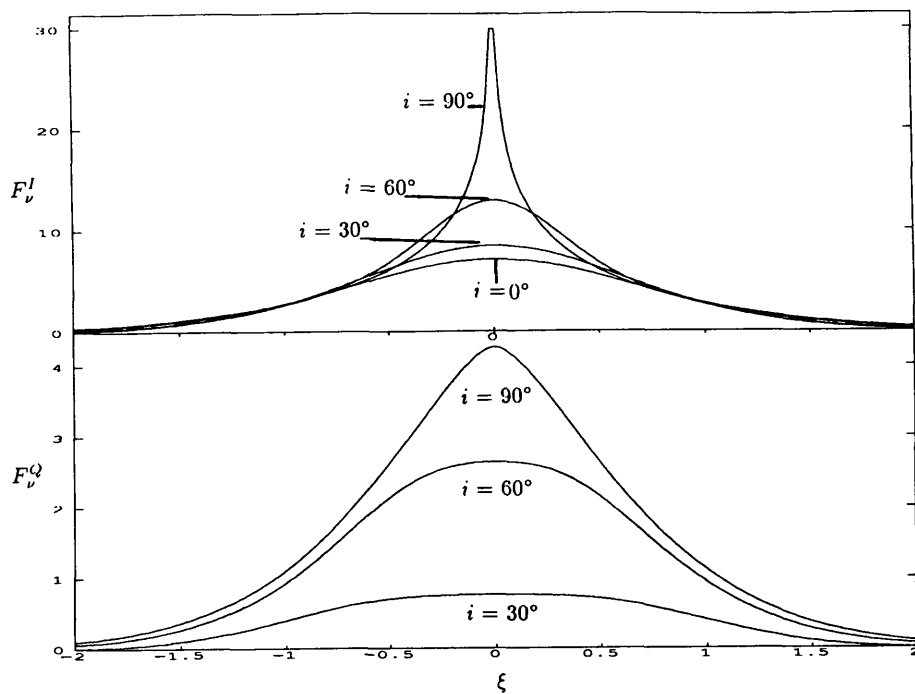


**Fig. 4.1** The resultant Stokes fluxes after scattering monochromatic stellar radiation in an isothermal planar disc at various inclinations

Figure 4.1 shows the scattered Stokes fluxes for the above inclination values (Eqs. 4.21 and 4.22) and also the results of numerical calculations of Eq. 4.17 for inclination values where “analytic” solutions could not be found. It is seen that the scattered fluxes are broadened symmetrically about line centre, illustrating the broadening of line radiation due to (single) Thomson scattering off hot electrons.

#### 4.5 Gaussian line source

In this case the source is taken to be a Gaussian emission line, according to Eq. 2.30, viz,

$$I_{\nu_*}(\lambda_*) = I_0 \left[ 1 + s \exp - \left( \frac{\lambda_* - \lambda_0}{\lambda_b} \right)^2 \right] . \quad (4.23)$$

For scattering in an isothermal disc this may be expressed as,

$$I_{\nu_*}(\xi_*) = I_0 \left[ 1 + s e^{-a \xi_*^2} \right] , \quad (4.24)$$

where  $\xi_*$  is given by Eq. 4.12 and,

$$a = \frac{4 k T}{m_e c^2} \left( \frac{\lambda_0}{\lambda_b} \right)^2 . \quad (4.25)$$

The choice of a Gaussian line profile and the Gaussian nature of the thermal redistribution function allows the integration over the incident wavelengths ( $\xi_*$ ) in Eq. 4.13 to be performed explicitly. The scattered Stokes fluxes for this case of a point Gaussian emission line source scattering in an

isothermal planar disc are then determined by,

$$\begin{pmatrix} F_{\nu}^I(\xi) \\ F_{\nu}^Q(\xi) \\ F_{\nu}^U(\xi) \end{pmatrix} = \sigma_0 F_0 \int_A \left[ 1 + \frac{s \exp \frac{-\xi^2}{1+a(1-\sin i \cos \phi)}}{\sqrt{1+a(1-\sin i \cos \phi)}} \right] \Sigma(r) \begin{pmatrix} 2(1 + \sin^2 i \cos^2 \phi) \\ \sin^2 i - (1 + \cos^2 i) \cos 2\phi \\ 2 \cos i \sin 2\phi \end{pmatrix} \frac{dA}{r^2}. \quad (4.26)$$

These equations are integrated numerically, neglecting occultation effects, for  $i = 60^\circ$ ,  $s = 2$ ,  $\lambda_0 = 6562\text{\AA}$ ,  $\lambda_b = 4\text{\AA}$  and compared with the results of Sect. 2.5.1 where the scattering electrons were cold, but moving with a Keplerian velocity profile with  $\beta_0 c = 450 \text{ km.s}^{-1}$ . Figure 4.2(a) shows these comparative results for isothermal discs at  $10^2$ ,  $10^3$  and  $10^4$  Kelvin. The scattered  $U$  flux is zero at all wavelengths as explained previously – i.e. cancellation of the  $U$  component of the polarisation vectors at  $(r, \phi)$  and  $(r, -\phi)$  for the isothermal disc and cancellation when summing over the isowavelength-shift contours on the rotating disc. In Fig. 4.2(b) the initial stellar line profile and the scattered degree of polarisation –  $P = F^Q/F^D$  – across the line are shown for the two cases. These figures show that for typical Be star temperatures thermal smearing results in spectropolarimetric profiles which are similar in shape to scattering in a rotating disc – i.e. symmetrically broadened about line centre with a decrease in the polarisation at line centre. High temperatures result in extended line wings, similar to Munch's results for the emergent intensity from a plane parallel electron scattering atmosphere. Note, however, that Munch calculated the resultant intensity profiles for atmospheres of different optical depths and the work presented above only considered the optically thin (single scattering) limit.

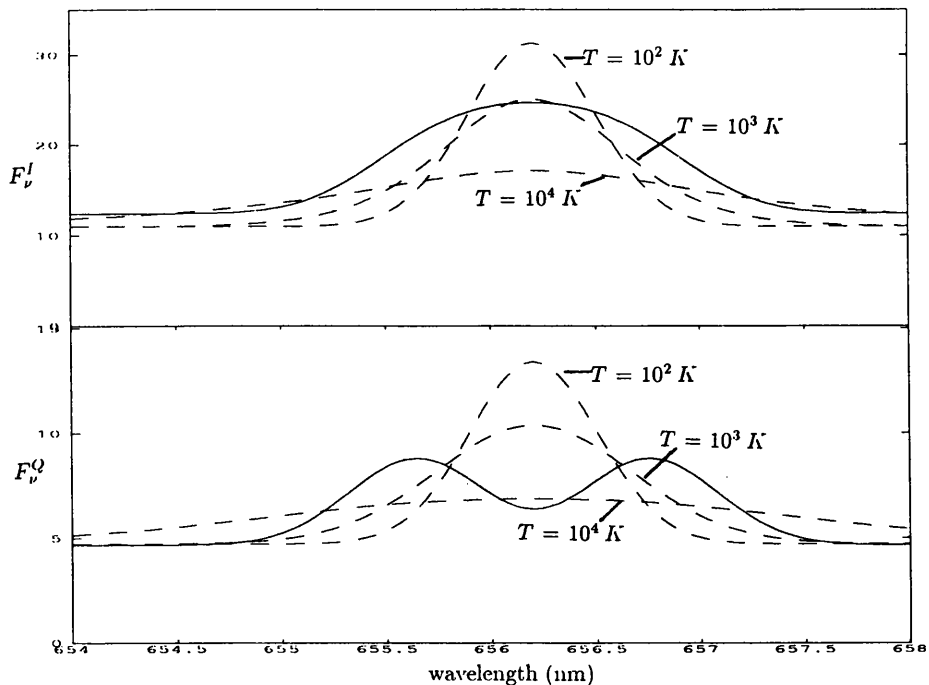


**Fig. 4.2(a)** Resultant Stokes fluxes after scattering stellar radiation with a spectral profile given by Eq. 4.23 in an isothermal disc at temperatures of  $10^2$ ,  $10^3$  and  $10^4$  Kelvin with  $i = 60^\circ$ . Also shown for comparison are the fluxes arising from scattering of stellar radiation in a cold Keplerian rotating disc (solid lines).

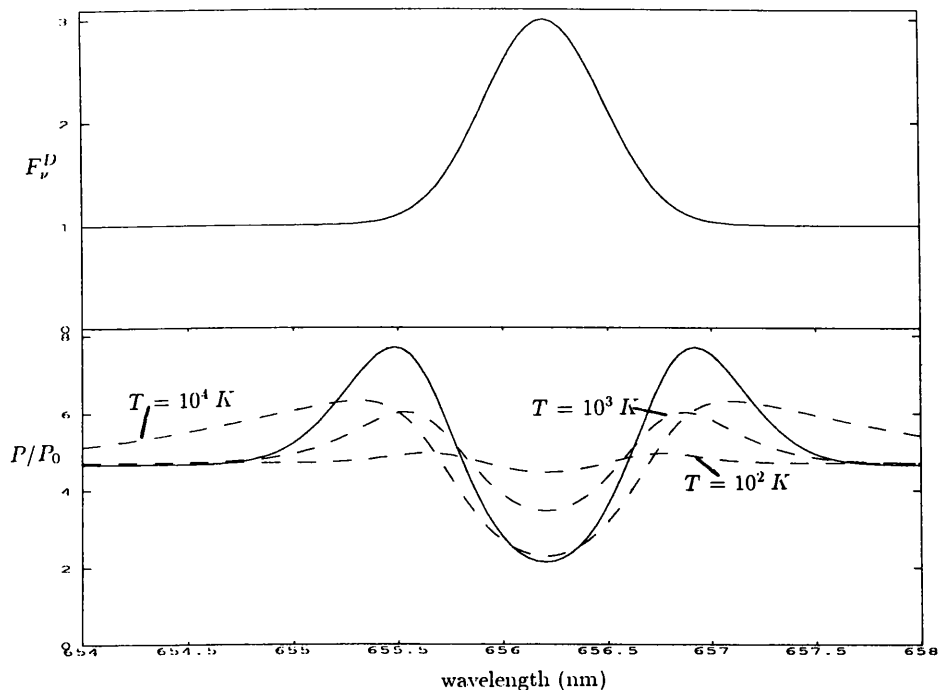


Fig. 4.2(b) Direct flux normalised to the continuum and degree of scattered polarisation for the case described above.

#### 4.6 Effect of electron bulk and thermal motions

The above analysis has considered the formation of spectropolarimetric line profiles from the Doppler redistribution of scattered radiation arising from either the bulk motion of the disc electrons or their thermal velocity. Clearly the effect of both bulk *and* thermal motions on the scattered radiation should be considered. This may be formulated by assuming that the electron velocity may be specified by a bulk component,  $\beta c$ , and a random thermal component,  $\beta_T c$ . Transforming into a frame in which the bulk velocity is zero, the redistribution function for the scattered radiation is given by Eq. 4.8, noting that the incident frequency (seen as  $\nu_B$ ) must be transformed into that frame via,

$$\nu_B \approx (1 - \beta \cdot \hat{\mathbf{k}}_*) \nu_*, \quad (4.27)$$

where  $\gamma = 1/\sqrt{1 - \beta^2}$  is assumed to be unity due to the small stellar wind speeds under investigation. The scattered frequency due to this thermal smearing,  $\nu_T$ , must now be related to the frequency,  $\nu$ , seen by the observer, thus,

$$\nu_T \approx (1 - \beta \cdot \hat{\mathbf{k}}) \nu. \quad (4.28)$$

Therefore, radiation from a point source incident at frequency  $\nu_*$  is redistributed in frequency due to bulk and thermal Doppler shifts according to,

$$I_\nu(\nu) = \int I_{\nu_*}(\nu_*) \psi(\nu_B, \nu_T) d\nu_B, \quad (4.29)$$

where  $\psi(\nu_B, \nu_T)$  is the thermal smearing function, Eq. 4.8, and  $\nu_B$  and  $\nu_T$  are given by Eqs. 4.27 and 4.28 respectively. The resultant scattered Stokes fluxes are then determined by integrating

Eq. 4.29 multiplied by the Rayleigh angular redistribution functions and the density factors over the entire scattering region.

#### 4.7 The effect of electron bulk and thermal motions on the scattering of monochromatic radiation

Following Eq. 4.27 and the properties of the delta function a monochromatic source may be represented as,

$$I_{\nu_*}(\nu_*) = I_0 \delta[\nu_* - \nu_0] = (1 - \beta \cdot \hat{\mathbf{k}}_*) I_0 \delta[\nu_B - (1 - \beta \cdot \hat{\mathbf{k}}_*)\nu_0], \quad (4.30)$$

which reduces Eq. 4.29 to,

$$I_\nu(\nu) = I_0 \left[ \frac{m_e c^2 (1 - \beta \cdot \hat{\mathbf{k}}_*)^2}{4 \pi k T \nu_T^2 (1 - \cos \Theta)} \right]^{\frac{1}{2}} \exp \left[ -\frac{m_e c^2}{4 k T (1 - \cos \Theta)} \left( \frac{(1 - \beta \cdot \hat{\mathbf{k}}_*)\nu_0 - \nu_T}{\nu_T} \right)^2 \right]. \quad (4.31)$$

For a point source at the centre of a planar disc, with  $D = (1 - \beta \cdot \hat{\mathbf{k}}_*)/(1 - \beta \cdot \hat{\mathbf{k}})$  and  $\alpha = (\lambda - \lambda_0)/\lambda_0$  the dimensionless wavelength shift from line centre, the Stokes fluxes are,

$$\begin{aligned} \left\{ \begin{array}{l} \nu F_\nu^I(\alpha) \\ \nu F_\nu^Q(\alpha) \\ \nu F_\nu^U(\alpha) \end{array} \right\} &= \sigma_0 F_0 \left[ \frac{m_e c^2}{4 \pi k T} \right]^{\frac{1}{2}} \iint_D \frac{\Sigma(\mathbf{x})}{x} \frac{\exp \left[ \frac{-m_e c^2 (1 - (1 + \alpha) D)^2}{4 k T (1 - \sin i \cos \phi)} \right]}{\sqrt{(1 - \sin i \cos \phi)}} \\ &\times \left\{ \begin{array}{l} 2(1 + \sin^2 i \cos^2 \phi_0) \\ \sin^2 i - (1 + \cos^2 i) \cos 2\phi_0 \\ 2 \cos i \sin 2\phi_0 \end{array} \right\} dx d\phi. \end{aligned} \quad (4.32)$$

These equations are now integrated numerically for the cases of scattering monochromatic stellar line radiation in an isothermal disc which has bulk rotational, expansional and a combination of these velocity profiles.

##### 4.7.1 Isothermal rotating disc

Figure 4.3 shows the Stokes fluxes arising from scattering of monochromatic stellar radiation in an isothermal disc which is rotating with a Keplerian velocity profile (rotational speed at stellar surface is  $450 \text{ km} \cdot \text{s}^{-1}$ ) and the number density is inversely proportional to radial distance ( $q = 1$  in Eq. 2.17).

The scattered  $I$  and  $Q$  flux profiles have spectral shapes similar to the “cold” case of Sect. 2.4.1, but are symmetrically broadened about line centre with the degree of “smearing” depending

on the disc temperature. For low temperatures the scattered fluxes are, essentially, formed by summing over the isowavelength-shift contours as in Chapter 2. However, as the temperature is increased other parts of the disc will contribute to the scattered flux at a given  $\alpha$  since the electron thermal motion from these areas will yield a sufficient thermal Doppler shift to “overcome” the bulk Doppler shift from that area allowing the scattered radiation to appear at the given  $\alpha$ . Since increasing the disc temperature allows larger regions of the disc to contribute to the scattered flux at a given  $\alpha$  the spectral features associated with scattering in a cold disc (which isolated localised disc regions at different  $\alpha$  values) tend to be “washed out”. This is evident in the  $Q$  flux profile of Fig. 4.3 which loses the negative spectral feature at  $\alpha \approx 0$  (explained in Sect. 2.4.1 for a cold disc) as the temperature rises.

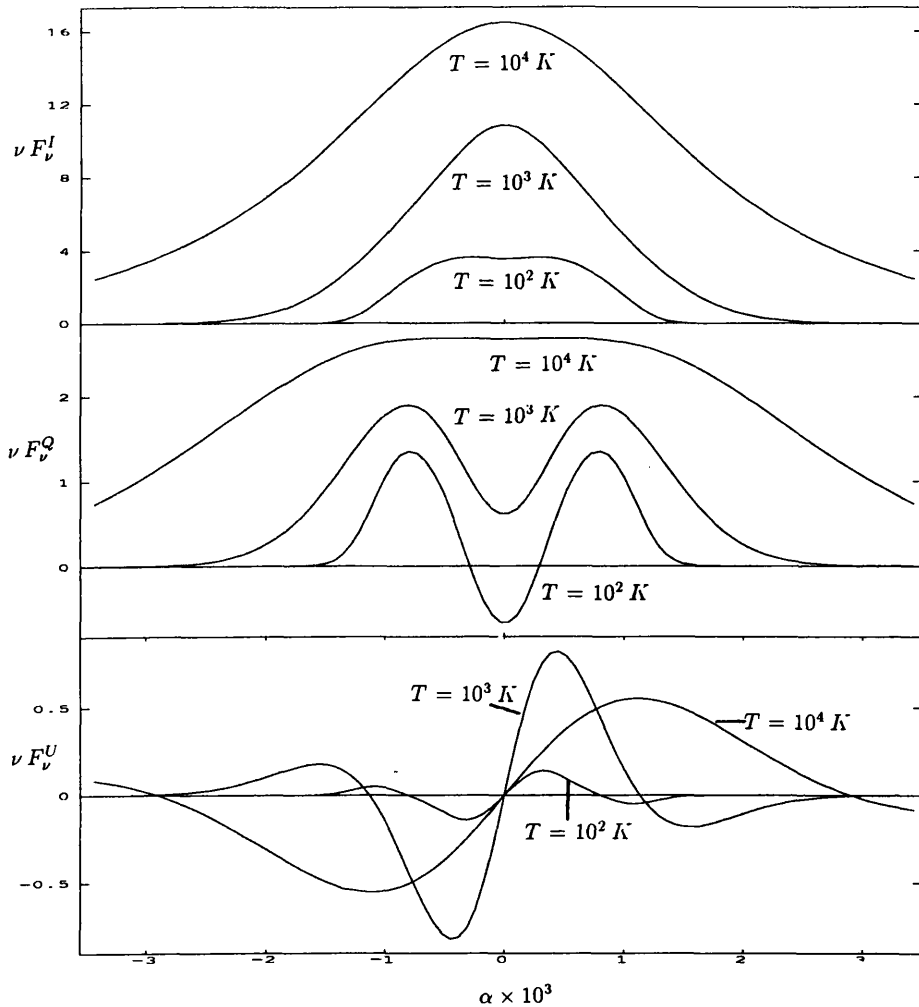


**Fig. 4.3** Resulting Stokes fluxes after scattering monochromatic stellar radiation in an isothermal disc which also has a bulk Keplerian velocity component

Another effect of combined bulk and thermal Doppler shifts is that the scattered  $U$  flux is now non-zero possessing an antisymmetric variation about  $\alpha = 0$ . This is explained by a combination of the preferential back-scattering of the thermal redistribution function as before and by the disc rotation which breaks the antisymmetry across the disc.

#### 4.7.2 Isothermal expanding disc

The Stokes fluxes arising from scattering monochromatic stellar radiation in an isothermal disc expanding with a constant velocity of  $150 \text{ km.s}^{-1}$  are shown in Fig. 4.4. This figure again illustrates the “washing out” of spectral features at high temperatures (e.g. the negative  $Q$  flux at extreme  $\alpha$  values) caused by the dominance of the thermal over bulk Doppler shifts. In this case of pure expansion of the isothermal disc the scattered  $U$  flux is zero at all frequencies. For an expanding disc the isowavelength-shift contours are symmetric about  $\phi = 0$  (e.g. Fig. 2.13, unlike a rotating disc) resulting in cancellation of the  $U$  components at  $(r, \phi)$  and  $(r, -\phi)$ . This same symmetrical cancellation occurs when the electrons are in random thermal motion (Sect. 4.4 above) so that combining bulk and thermal effects will not yield any  $U$  flux throughout the scattered polarimetric line profile.

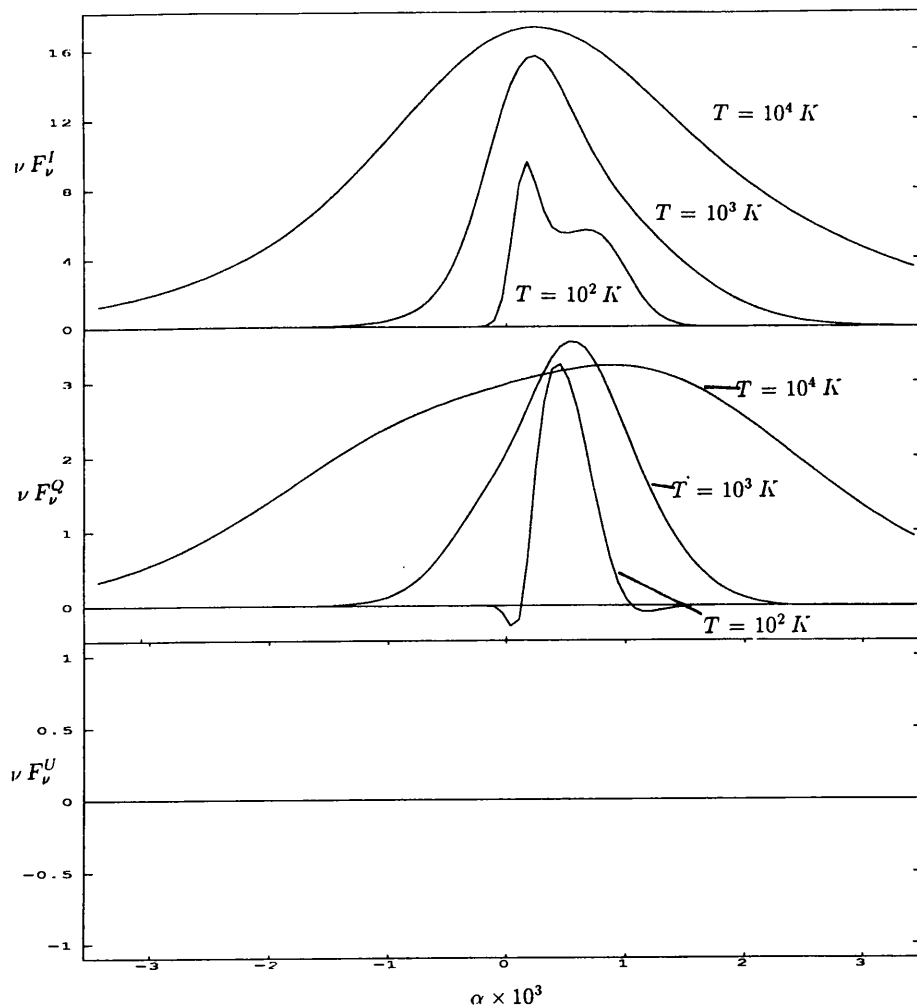


**Fig. 4.4** As for Fig. 4.3 except for a constant expansion bulk component of the disc velocity.

### 4.7.3 Rotating and expanding isothermal disc

The scattered Stokes fluxes arising when the bulk velocity of the isothermal disc is a combination of Keplerian rotation and constant expansion are shown in Fig. 4.5. This again illustrates the gradual “washing out” of the spectral features as the disc temperature rises.

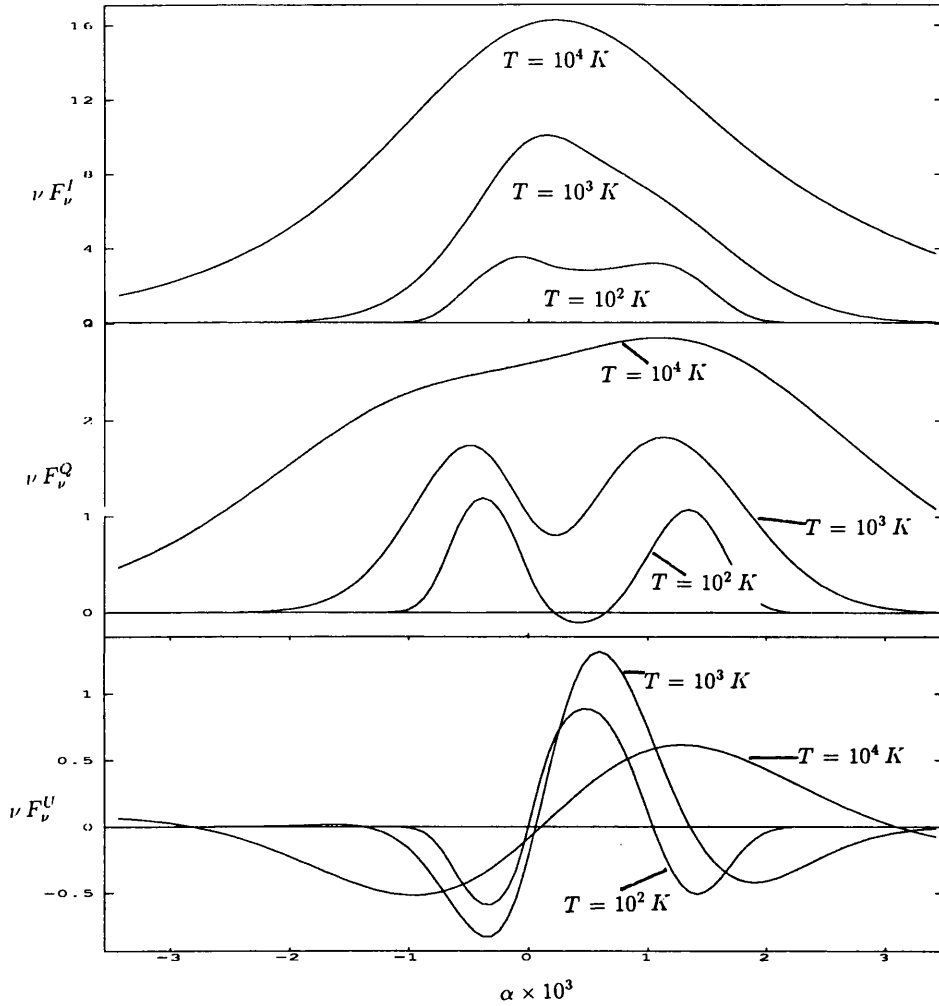


Fig. 4.5 As for Fig. 4.3 except for an isothermal disc with both rotational and expansive bulk velocity components.

### 4.8 Determination of disc inclination

The disc inclination may be determined by taking the ratio of the integrated scattered total to polarised fluxes as in Sect. 2.6. Due to the normalisation properties of the thermal redistribution function and the monochromatic line profile integrating Eq. 4.32 over all  $\alpha$  gives,

$$\begin{Bmatrix} \nu F^I(\alpha) \\ \nu F^Q(\alpha) \\ \nu F^U(\alpha) \end{Bmatrix} = \int_{-\infty}^{\infty} \begin{Bmatrix} \nu F_{\nu}^I(\alpha) \\ \nu F_{\nu}^Q(\alpha) \\ \nu F_{\nu}^U(\alpha) \end{Bmatrix} d\alpha = \sigma_0 F_0 \iint \frac{\Sigma(x)}{x} \begin{Bmatrix} 2(1 + \sin^2 i \cos^2 \phi_0) \\ \sin^2 i - (1 + \cos^2 i) \cos 2\phi_0 \\ 2 \cos i \sin 2\phi_0 \end{Bmatrix} dx d\phi, \quad (4.33)$$

which yields the same result as in Sect. 2.6, namely,

$$\frac{F^Q}{F^I} = \frac{\sin^2 i}{2 + \sin^2 i} \quad (4.34)$$

Thus when the wavelength average across the line is performed the scattered  $U$  flux averages to zero as before. The beauty of this is that relation 4.34 determines  $i$  even with thermal electron broadening present.

## 5. Spectropolarimetric scattered line profiles from axisymmetric three-dimensional circumstellar envelopes

### Summary

This chapter considers the Thomson scattering of stellar line radiation in a three dimensional axisymmetric circumstellar envelope which is undergoing bulk and thermal motion. Based on computations of spectropolarimetric line profiles for the scattering of stellar line radiation, a discussion is presented of future theoretical work to be undertaken in the study of such profiles with application to current data and instrumentation capabilities.

### 5.1 Three dimensional axisymmetric circumstellar envelopes

The polarisation arising from Be stars is generally considered to arise through Thomson scattering in an axisymmetric flattened circumstellar envelope (Coyne, 1976) and in Chapters 2, 3 and 4 this circumstellar region was modelled as a planar disc. This parametrisation is obviously an extreme case, but was shown to give considerable insight into the formation of spectropolarimetric line profiles. A more realistic model, which will now be considered, is that of a spherical circumstellar envelope which has an axisymmetric electron number density thus,

$$n(x, \theta) = n_0 x^{-q} \sin^m \theta, \quad (5.1)$$

where  $n_0$  is the equatorial electron number density at the stellar surface ( $x = 1$ ),  $\theta$  is the polar angle,  $q$  and  $m$  are indices which determine the radial and angular density distribution and  $x = r/R$  as before. This form for the density law can range from a completely spherical distribution ( $m = 0$ ) to a planar disc ( $m = \infty$ ) and is thus very adaptable for modelling purposes. A common model for a Be star is that of a central star surrounded by a wedge-shaped envelope of a specified opening angle (e.g. Cassinelli & Haisch, 1974). Something akin to this may be approximated by Eq. 5.1 by considering the angle measured from the equator,  $\theta_0$  at which the electron number density is one half of its equatorial value, viz,

$$\theta_0 = \cos^{-1} 2^{-1/m}. \quad (5.2)$$

With this definition the "opening angle" of the envelope is just  $2\theta_0$ .

The radial dependence of the density may be determined from the continuity equation for a three dimensional region - e.g. a constant expansion velocity has  $q = 2$  while a more complex dependence of the velocity with radial distance requires the simple radial power law form of Eq. 5.1 to be replaced by,

$$n(x) = \frac{n_0}{\beta_r(x) x^2}. \quad (5.3)$$

In this chapter the bulk rotational and expansional components of the envelope velocity shall be parametrised as,

$$\beta_\phi(x, \theta) = \beta_0 x^{-\frac{1}{2}} \sin \theta, \quad \beta_r(x, \theta) = \beta_1, \quad (5.4)$$

that is, a constant expansion velocity and a Keplerian rotational component which decreases with latitude (maximum at the equator, falling to zero at the pole).

For scattering unpolarised radiation from a point source in a three dimensional envelope the Rayleigh angular phase function is, from Eq. 1.29,

$$\mathbf{P} = \begin{pmatrix} (3 - \cos^2 i) - (1 - 3 \cos^2 i) \cos^2 \theta + \sin^2 i \sin^2 \theta \cos 2\phi + \sin 2i \sin 2\theta \cos \phi \\ \sin^2 i (1 - 3 \cos^2 \theta) - (1 + \cos^2 i) \sin^2 \theta \cos 2\phi + \sin 2i \sin 2\theta \cos \phi \\ 2 \cos i \sin^2 \theta \sin 2\phi - 2 \sin i \sin 2\theta \sin \phi \end{pmatrix}. \quad (5.5)$$

The above formalism now allows the Stokes fluxes arising from the scattering of stellar line radiation in a three dimensional axisymmetric envelope to be calculated.

## 5.2 Scattering of stellar line radiation

The spectral shape of the central point emission line source is assumed to be Gaussian as before, viz,

$$I_{\nu_*}(\lambda_*) = I_0 \left[ 1 + s \exp - \left( \frac{\lambda_* - \lambda_0}{\lambda_b} \right)^2 \right]. \quad (5.6)$$

For a three dimensional scattering envelope the observed wavelength arising from the Doppler redistribution of scattered radiation is, from Eq. 2.1,

$$\lambda = \left( \frac{1 - \beta_r(x, \theta) \sin \theta \cos \phi \sin i + \beta_\phi(x, \theta) \sin \phi \sin i - \beta_r(x, \theta) \cos \theta \cos i}{1 - \beta_r(x, \theta)} \right) \lambda_*, \quad (5.7)$$

so that the exponent in Eq. 5.6 may be written as,

$$A(x, \theta, \phi, \lambda) = \left( \frac{\lambda_* - \lambda_0}{\lambda_b} \right) = \frac{\{1 - \beta_r(x, \theta)\} \lambda - \{1 - \beta_r(x, \theta) \sin i \sin \theta \cos \phi + \beta_\phi(x, \theta) \sin i \sin \phi - \beta_r(x, \theta) \cos i \cos \theta\} \lambda_0}{\{1 - \beta_r(x, \theta) \sin i \sin \theta \cos \phi + \beta_\phi(x, \theta) \sin i \sin \phi - \beta_r(x, \theta) \cos i \cos \theta\} \lambda_b}. \quad (5.8)$$

The Stokes fluxes arising from scattering of radiation from a point source in a three dimensional envelope (ignoring occultation effects) are determined from solution of,

$$\mathbf{F}_\nu = \sigma_0 F_0 \int_V (1 + s \exp - \{A(r, \theta, \phi, \lambda)\}^2) n(r, \theta) \mathbf{P} \frac{dV}{r^2}, \quad (5.9)$$

where  $\mathbf{P}$ ,  $A(r, \theta, \phi, \lambda)$  and  $n(r, \theta)$  are given by Eqs. 5.5, 5.7 and 5.3 respectively.

In Chapter 2 the spectral shapes of the scattered Stokes fluxes were explained with reference to isowavelength-shift contours on the flat disc (Eq. 2.2). However, in this chapter these contours

are replaced by *surfaces* (determined from Eq. 2.2 for a three dimensional envelope) from which the scattered radiation has the same relative Doppler shift. These surfaces are not presented in graphical form, but their features which determine the scattered spectropolarimetric line profiles will be described in the relevant sections below. As in Section 2.5 the isowavelength–shift surfaces become smeared when considering the scattering of non–monochromatic radiation with the degree of smearing being proportional to  $\lambda_b$ .

The variations in the Stokes fluxes across the scattered line are now calculated for cases when the envelope’s bulk velocity is pure rotation, pure expansion and a combination of these. The initial unpolarised stellar line is specified with  $s = 2$ ,  $\lambda_0 = 6562\text{\AA}$  and  $\lambda_b = 4\text{\AA}$ . The effect on the scattered spectropolarimetric line profiles of various disc “opening angles” are investigated by changing the  $m$  value in Eq. 5.1 while the radial density distribution is parametrised by  $q = 2$  (pure radial expansion) and the inclination is fixed at  $i = 60^\circ$ .

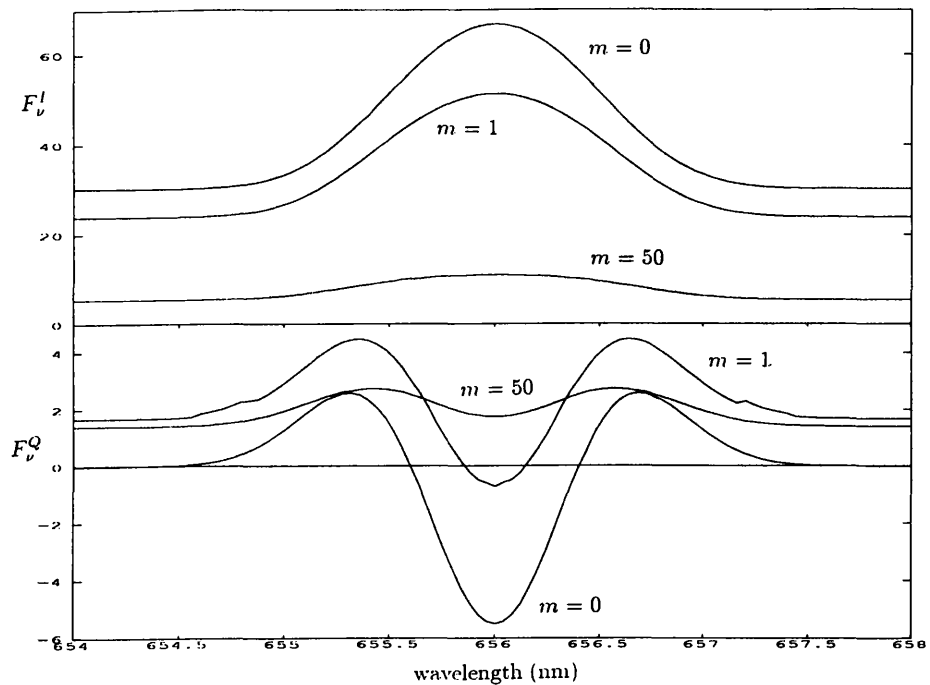


**Fig. 5.1** The resulting Stokes fluxes for scattering stellar radiation with a spectral shape given by Eq. 5.6 in a Keplerian rotating envelope, at  $i = 60^\circ$ .  $\beta_0 c = 450 \text{ km.s}^{-1}$ . in Eq. 5.4.

### 5.2.1 Pure envelope rotation

Figure 5.1 shows the scattered spectropolarimetric line profiles for scattering of stellar line radiation in an envelope with polar density indices of  $m = 0, 1$  and  $50$  and  $i = 60^\circ$ . These  $m$  values represent a spherical and progressively more equatorial density distributions –  $\theta_0$  values being  $60^\circ$  and  $\sim 10^\circ$ . It is seen that the symmetry breaking effect of the envelope rotation results in a non-zero  $Q$  flux within the scattered line even for the spherical,  $m = 0$ , density distribution. This occurs due to the shape of the isowavelength–shift surfaces which are such that the zero shift occurs along

the meridional plane containing the observer where the line of sight velocity is zero. Radiation scattered from these regions has its polarisation vector oriented perpendicular to the envelope's rotational symmetry axis hence the negative  $Q$  flux at the centre of the scattered line. The higher wavelength shifts occur towards the regions of the stellar limb. Since there is more solid angle toward the equator than the pole the  $Q$  flux is positive in the wings falling to zero (the expected continuum value for scattering in a spherical envelope) beyond the maximum Doppler shift. As the density becomes more equatorial (increasing  $m$ ) the scattered spectropolarimetric line profiles resemble the results for a planar disc – Fig. 2.16(a), though the spectral features are not as distinct due to the increased polarimetric cancellation between the polar and equatorial regions which occurs in a non planar electron distribution. The scattered  $U$  flux is zero at all wavelengths (neglecting occultation) due to the symmetry of the isowavelength-shift surfaces within the rotating envelope.

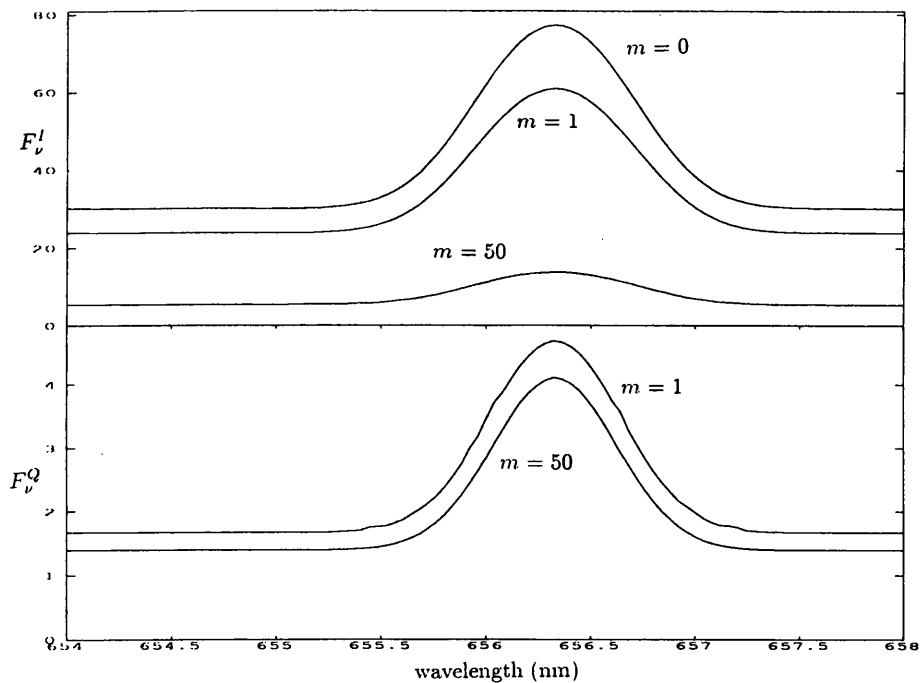


Fig. 5.2 As for Fig. 5.1, but for the envelope velocity being purely expansional.

### 5.2.2 Pure envelope expansion

When the envelope velocity is pure radial expansion (Eq. 5.4) the scattered spectropolarimetric line profiles for  $m = 0, 1$  and  $50$  are shown in Fig. 5.2. When the envelope density is spherically symmetric the  $Q$  and  $U$  fluxes are zero across the scattered line due to the polarimetric symmetry of the isowavelength-shift surfaces for this case of pure envelope expansion. For a radially expanding spherical envelope it is impossible to define any reference plane (or inclination) so there is complete polarimetric cancellation across the scattered line. Note that the (single) scattered  $I$  flux exhibits red shifts similar to the Monte Carlo results of Lefevre (Fig. 2.7) who used an anisotropic radiation source and hence obtained non-zero polarimetric profiles. As the density becomes more equatorial

the scattered profiles again tend to resemble the spectral shape of the Chapter 2 profiles – Fig. 2.17(a). The polarimetric cancellation about the line of sight of the isowavelength–shift surfaces is such that the scattered  $U$  flux is zero for all  $m$  values (and all inclinations also).

### 5.2.3 Envelope rotation and expansion

Figure 5.3 shows the scattered spectropolarimetric line profiles when the envelope has bulk rotational and expansional velocity components given by Eq. 5.4. The profiles have similar spectral shapes to those of Sect. 2.5.3 (stronger  $Q$  flux in the red wing,  $U$  flux and hence position angle variations across the line, etc), but at lower amplitude and “resolution” due to the polarimetric cancellation of the non planar electron distribution as in the above sections.

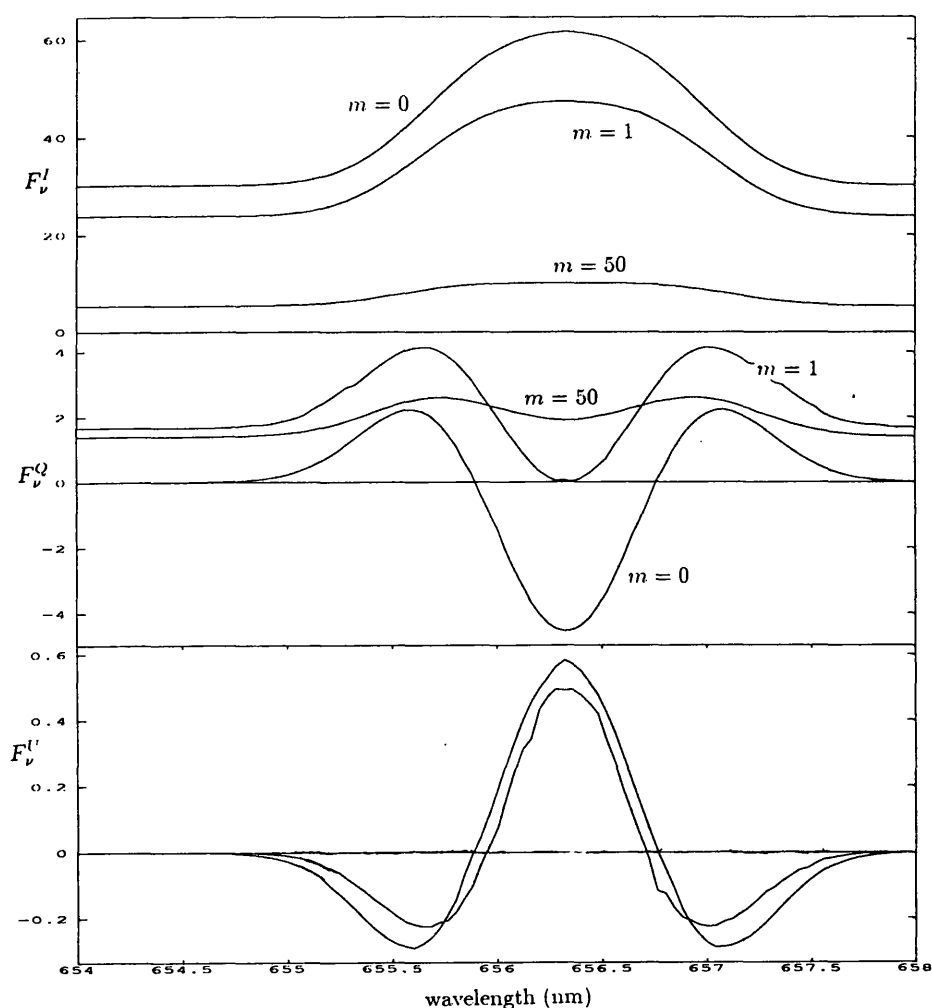


Fig. 5.3 As for Fig. 5.1, but for a rotating and expanding envelope.

### 5.3 Electron bulk and thermal motions in a three dimensional envelope

This section considers the effect of electron bulk and thermal motions on the Doppler redistribution of scattered stellar radiation in the axisymmetric envelope described in Sect. 5.1. The equations determining the scattered spectropolarimetric line profiles are derived in the same manner as in

Sect 4.6 – assuming the total electron velocity to be the sum of bulk and Maxwellian components, transforming the incident frequency to the frame in which the bulk component is zero, applying the thermal redistribution in this frame and then transforming the result to the observer's frame. Proceeding in this way for incident monochromatic stellar radiation gives the same result as Eq. 4.32, except the velocity and direction vectors and the scattering angular phase function are modified for scattering in a three dimensional envelope, viz,

$$\mathbf{F}_\nu(\alpha) = \frac{3\sigma_T}{16\pi} I_0 \left[ \frac{m_e c^2}{4\pi kT} \right]^{\frac{1}{2}} \int_V \frac{\exp \left[ \frac{-m_e c^2(1-(1+\alpha)D)^2}{4kT(1-\cos\chi)} \right]}{\sqrt{(1-\cos\chi)}} D n(r, \theta, \phi) \mathbf{P} \frac{dV}{r^2}, \quad (5.10)$$

where  $\chi$  is the scattering angle, viz,

$$\cos \chi = \cos \theta \cos i + \sin \theta \cos \phi \sin i. \quad (5.11)$$

$\mathbf{P}$  is given by Eq. 5.5 and  $D = (1 - \beta \cdot \hat{\mathbf{k}}_*) / (1 - \beta \cdot \hat{\mathbf{k}})$ . For a point source scattering in a three dimensional envelope this becomes,

$$D = \frac{1 - \beta_r(x, \theta)}{1 - \beta_r(x, \theta) \sin \theta \cos \phi \sin i - \beta_\phi(x, \theta) \sin \phi \sin i - \beta_r(x, \theta) \cos \theta \cos i}. \quad (5.12)$$

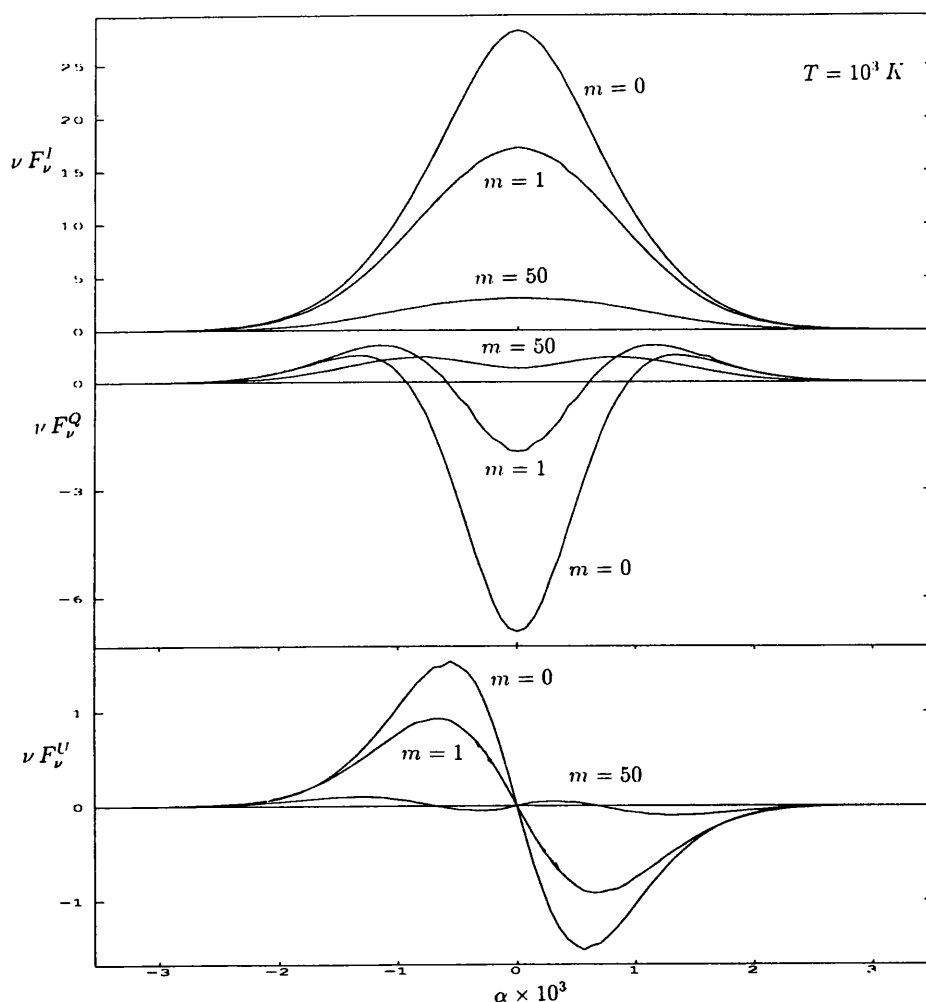


**Fig. 5.4(a)** Resulting Stokes fluxes after scattering monochromatic stellar radiation in an isothermal envelope,  $T = 10^3 K$ , which also has a bulk Keplerian velocity component.

Equation 5.10 is integrated numerically for  $i = 60^\circ$ , temperatures of  $10^3$  and  $10^4$  Kelvin and  $m$  values of 0, 1 and 50 when the bulk component of the envelope velocity is pure rotation, pure radial expansion and a combination of these (Eq. 5.4). The scattered Stokes fluxes for these cases are presented in Figs. 5.4 to 5.6. Comparing these scattered profiles with those of Sect. 4.7 (planar disc) it is seen that the spectral shapes are similar, but again they are not as defined due to the polarimetric cancellation properties of the envelope.

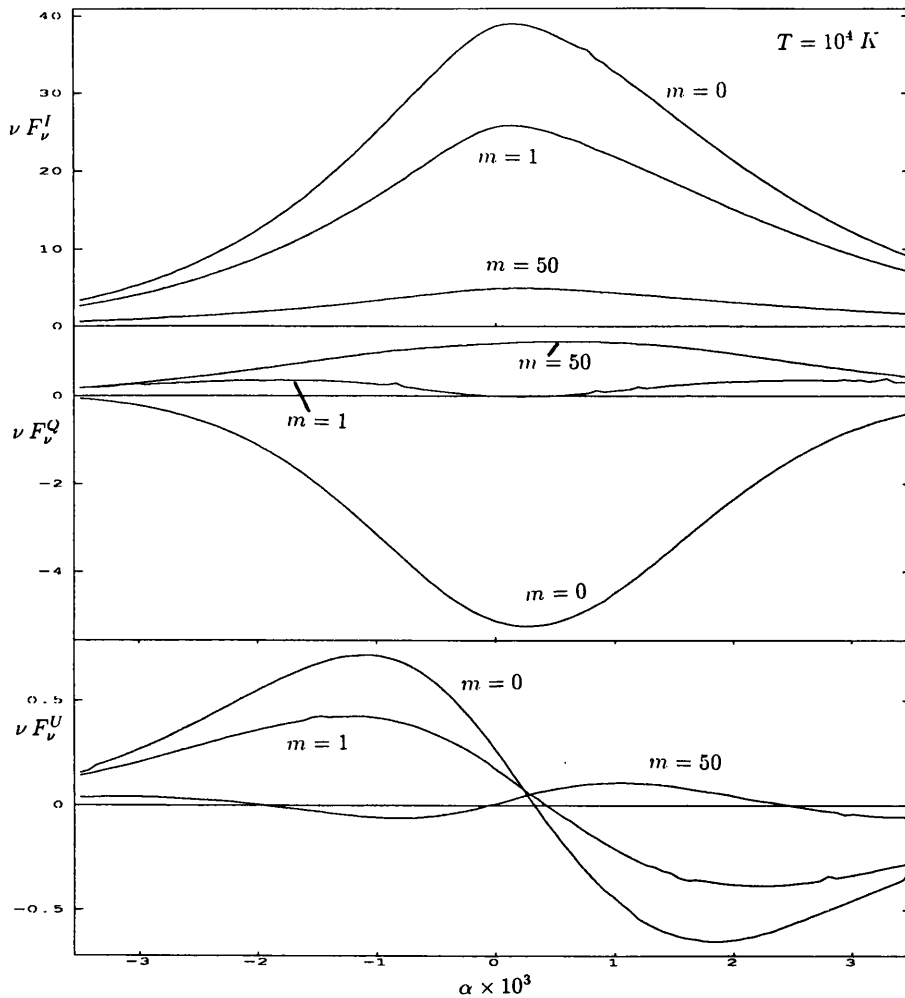
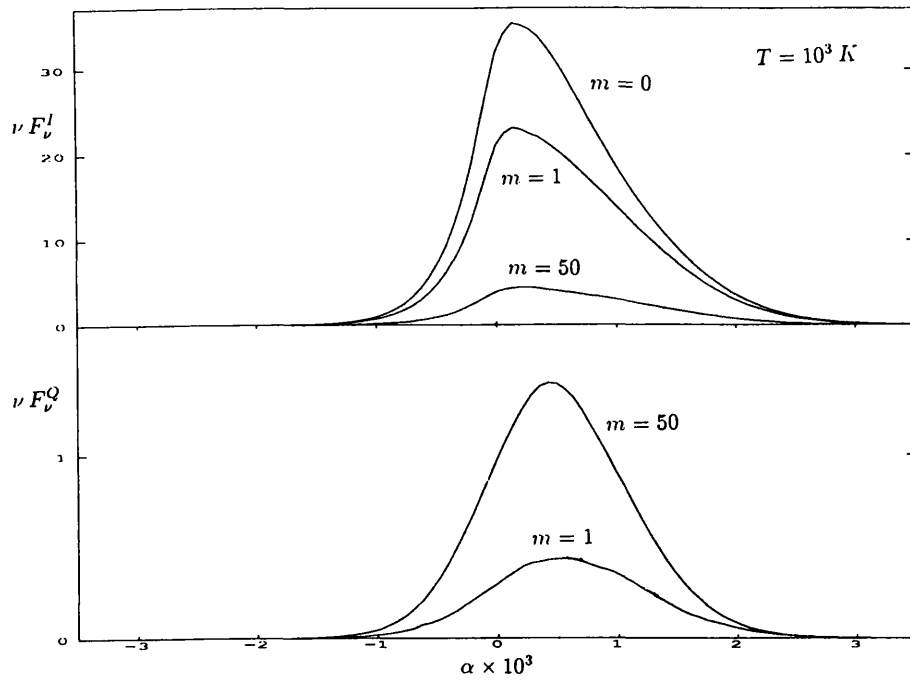


Fig. 5.4(b) As for Fig. 5.4(a) except for a temperature of  $T = 10^4 K$ .



**Fig. 5.5(a)** Resulting Stokes fluxes after scattering monochromatic stellar radiation in an isothermal envelope,  $T = 10^3 K$ , which also has a bulk expansion velocity component.

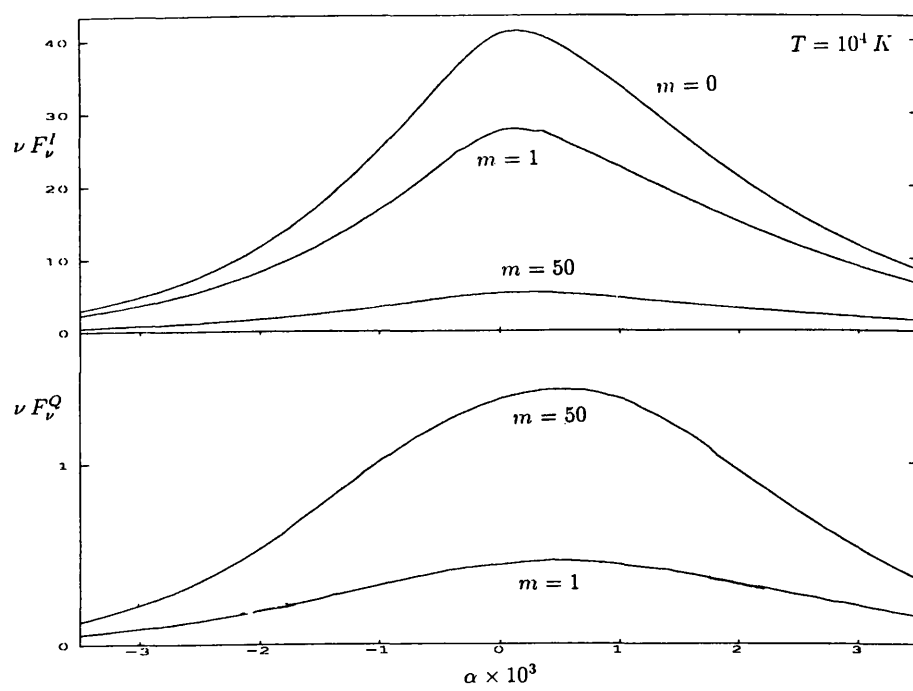
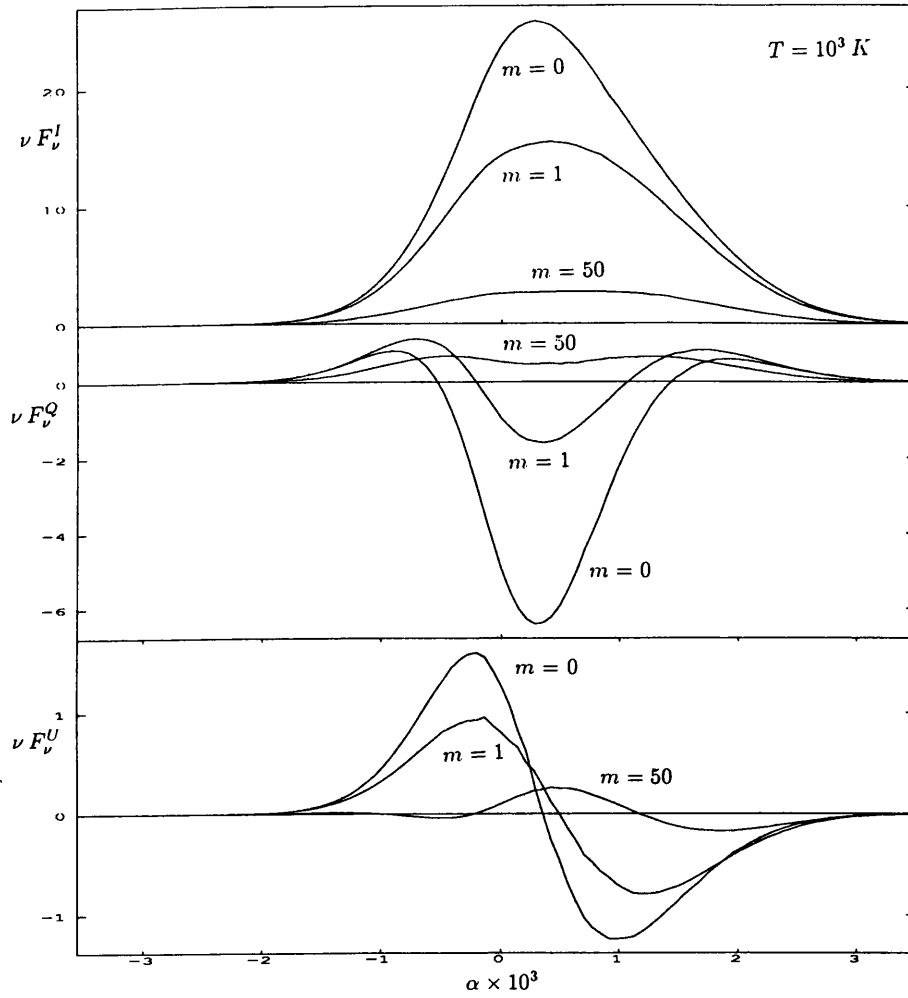


Fig. 5.5(b) As for Fig. 5.5(a) except for a temperature of  $T = 10^4 K$ .



**Fig. 5.6(a)** Resulting Stokes fluxes after scattering monochromatic stellar radiation in a rotating and expanding isothermal envelope,  $T = 10^3 K$ .

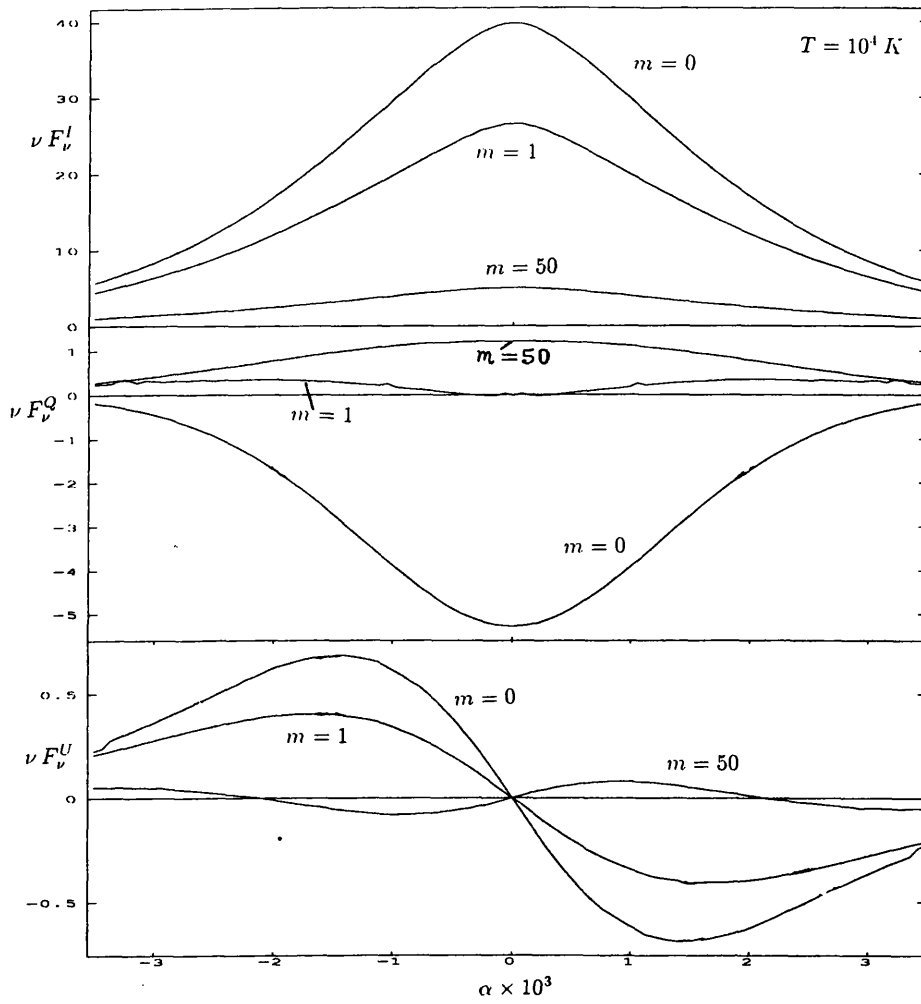


Fig. 5.6(b) As for Fig. 5.6(a) except for a temperature of  $T = 10^4 K$ .

## 5.4 Wavelength integrated Stokes fluxes

The inclination of the axisymmetric envelope considered above cannot be determined by the same method as in Chapters 2, 3 and 4 where the scattering region was a planar disc. Performing the wavelength integral over the entire scattered spectropolarimetric line profiles of Sects. 5.2 and 5.3 gives,

$$\frac{F^Q}{F^I} = \frac{\sin^2 i (1 - 3\gamma)}{\sin^2 i (1 - 3\gamma) + 2(1 + \gamma)}, \quad (5.13)$$

with  $F_\nu^U$  averaging to zero across the scattered line and  $\gamma$  is the shape factor defined in Eq. 1.33 viz,

$$\gamma = \frac{\int_{-1}^1 n(r, \mu) \mu^2 d\mu dr}{\int_{-1}^1 n(r, \mu) d\mu dr}. \quad (5.14)$$

As the distribution of electrons approaches plane,  $\gamma \rightarrow 0$ , thus enabling  $i$  to be determined uniquely. In practice  $\gamma$  is quite small even for moderately flattened envelopes. However, a general axisymmetric, non planar density profile of this chapter introduces this additional shape factor in the analysis such that the comments made by Brown & McLean (1977) following their theoretical investigation of continuum polarisation are valid here. Namely that measurements of the wavelength integrated scattered Stokes fluxes cannot tie down separately the geometry or inclination of the axisymmetric scattering region unless further assumptions can be made concerning  $\gamma$  or  $i$ . However, in the line case the further optical depth ambiguity present in the continuum case – cf Eqs. 1.31 and 1.32 – can be removed.

## 5.5 Future work

The work presented above concludes the analysis of spectropolarimetric line profiles formed by scattering of unpolarised stellar line radiation in a moving circumstellar envelope. This model is obviously a considerable simplification, but it does give a great deal of insight into the role of scattering and Doppler wavelength redistribution in the production of spectropolarimetric line profiles. In the stellar systems which have so far been analysed using high wavelength resolution spectropolarimetry (Be and Wolf Rayet stars – Section 2.1) the model becomes more complicated due to sources of continuum and line opacity and emission from the *envelope* itself (e.g. Poeckert & Marlborough. 1978). The remainder of this chapter outlines the future theoretical work to be undertaken in order to develop a more comprehensive understanding of spectropolarimetric line profile variations.

### 5.5.1 The general single scattering equation for monochromatic radiation

In the theoretical analysis presented in this thesis the unpolarised line emission was assumed to originate from a point stellar source – an assumption which allowed the effects of *stellar* rotation or expansion to be ignored. When forming the general single scattering equation the velocity and physical size of the source should thus be incorporated. Following a similar analysis to Sections

4.6 and 5.3 the general equation for the scattered Stokes fluxes is,

$$\mathbf{F}_\nu(\alpha) = \frac{3\sigma_T}{16\pi} I_0 \left[ \frac{m_e c^2}{4\pi k T} \right]^{\frac{1}{2}} \int_V \int_{\Omega_*} \frac{\exp \left[ \frac{-m_e c^2 (1 - (1 + \alpha) D_*)^2}{4kT(1 - \cos \chi)} \right]}{\sqrt{1 - \cos \chi}} D_* n(\mathbf{r}) \mathbf{P} d\Omega_* dV, \quad (5.15)$$

where  $n(\mathbf{r})$  is the electron number density at vector position  $\mathbf{r}$  in the scattering region,  $\Omega_*$  is the solid angle the source subtends at the scattering electron and  $V$  is the scattering volume (allowing for occultation effects also). The elemental solid angle ( $d\Omega_*$ ) and volume element ( $dV$ ) are as defined in Sect. 1.4.1 and Fig. 1.4. As in previous chapters  $\alpha$  is the dimensionless wavelength shift from line centre,  $I_0$  is the specific intensity of the monochromatic source at  $\lambda_0$  and the scattering angle,  $\Theta$ , is given by  $\cos \Theta = \hat{\mathbf{k}}_* \cdot \hat{\mathbf{k}}$ . The  $D_*$  parameter is given by,

$$D_* = \left( \frac{1 - \beta_* \cdot \hat{\mathbf{k}}_*}{1 - \beta \cdot \hat{\mathbf{k}}} \right), \quad (5.16)$$

and determines the Doppler wavelength redistribution due to the bulk motions of the source and scattering electrons with  $\beta_* \cdot \hat{\mathbf{k}}_*$  the radial velocity of the electron with respect to a point on the source (thus allowing for source motion), while  $\beta \cdot \hat{\mathbf{k}}$  is the radial velocity of the scattering electron with respect to the observer.

The integral over  $\Omega_*$  in Eq. 5.15 allows for line emission originating from any point and even within the scattering region itself – as occurs in the envelopes of Wolf Rayet stars for example. The point source approximation employed in this thesis is clearly an extreme case of Eq. 5.15 while line emission originating at large radial distances and scattering off electrons close to the stellar surface is another extreme. Analysis of the spectropolarimetric line profiles produced by this other extreme case (and intermediate cases) will provide further diagnostic techniques for probing the envelope velocity and density structure, but may also provide a means of determining where different line forming regions occur within the extended stellar atmosphere.

### 5.5.2 Line opacity and the extension to optically thick circumstellar envelopes

Poekert & Marlborough's model for  $\gamma$  Cassiopeiae (1978) and the qualitative work of McLean (1979) attributed the polarimetric variations within spectral lines to different spatial integrations of scattered stellar radiation in an extended atmosphere containing line opacity sources and undergoing mass motions (Sect. 2.2.3). This may be incorporated into an optically thin single scattering approximation by including the attenuation factor  $\exp -\tau_1(\lambda)$  prior to scattering of the *continuum* stellar radiation and the factor  $\exp -\tau_2(\lambda)$  which attenuates the scattered radiation as it traverses the envelope. The optical depths  $\tau_1(\lambda)$  and  $\tau_2(\lambda)$  are,

$$\tau_1(\lambda) = \int n_A \sigma_A(\lambda_A) ds, \quad \tau_2(\lambda) = \int n_A \sigma_A(\lambda_A) ds, \quad (5.17)$$

where the limits on the  $s$  integrals are from the source to the scattering electron for  $\tau_1$  and from the scattering electron to the observer (in practice the edge of the scattering envelope) for  $\tau_2$ .  $n_A$

is the number density of line absorbing atoms and  $\sigma_A(\lambda_A)$  is the line absorbing cross section of the atom at wavelength  $\lambda_A$  in the atoms rest frame which is related to the observed wavelength by the Doppler equation as before. As a first approximation the absorption cross section may be approximated by a delta function such that only stellar continuum wavelengths which are Doppler shifted to  $\lambda_0$ , say, are absorbed. This delta function approximation should simplify the mathematics in a similar way to the monochromatic approximation of Chapters 2, 3 and 4.

As the optical depth of the envelope increases the above approximation will no longer be valid due to the increased importance of re-emission of absorbed radiation and a radiative transfer approach must be adopted. A possible solution lies in the *Sobolev-P Method* developed by Jeffrey (1989). This technique utilises the conventional Sobolev (1960) escape probability formalism for a moving atmosphere and has been extended to include the transfer of polarised radiation – hence the *P*. Jeffrey’s analysis concentrated on the emergent polarimetric profiles of resonance lines from supernovae where the Sobolev approximation of the bulk velocity of the atmosphere being much greater than the thermal velocity of the atoms holds. As was outlined in Chapter 4 the electron thermal velocity in Be star envelopes is comparable to the bulk component and even in the faster and hotter Wolf Rayet winds electron thermal velocities are greater than 10% of the terminal velocity of the wind –  $v_\infty \approx 1500 \text{ km.s}^{-1}$ . When applying the Sobolev-P method to the extended atmospheres of Be and Wolf Rayet stars the comparatively large thermal component of the scattering electron’s velocity must be included in the calculation as in Chapter 4.

Proceeding in this way and noting the effect of the various approximations will lead to a more complete theoretical understanding of the formation of spectropolarimetric line profiles.

### 5.5.3 Temporal variations of spectropolarimetric line profiles

A topic not considered so far on the subject of spectropolarimetric line profiles is that of temporal variability – see Chapter 6, though, for analysis of temporal variations in the continuum polarisation. Spectrometry of Be stars has revealed that line profiles (e.g the Balmer lines) exhibit spectral changes on various time scales (Hanuschik, 1993). Recent models have attributed these changes to non axisymmetric density variations within an extended atmosphere – e.g. non radial oscillations or density waves (Papaloizou, et al, 1992). The simplest parametric model which predicts the correct qualitative behaviour of the spectrometric line profiles is that of a localised non axisymmetric density enhancement within a rotating disc. This may be incorporated in the model presented in this thesis by allowing the electron number density to vary with azimuthal angle on the disc – i.e.  $n(r, \theta, \phi)$ . However, the line forming region considered by Hanuschik is the envelope itself and the emergent line profiles were computed by a radiative transfer code, so the non axisymmetric density should be incorporated in Eq. 5.15 when calculating the spectropolarimetric line profiles.

Due to the limitations placed on line spectropolarimetry, discussed in Chapter 2, there are at

most a few observations of spectropolarimetric line profiles in any one star and hence temporal variations of any polarimetric line profiles have not been detected. The advent of high resolution spectropolarimeters (see below) should alleviate these problems and allow a concentrated spectropolarimetric observing program to be implemented in an attempt to detect variations with time of line polarisation.

#### 5.5.4 Application to non stellar objects

While the single scattering analysis presented was applied to the net (wavelength dependent) polarisation arising from scattering in moving circumstellar envelopes the theory of wavelength redistribution through light scattering off moving particles (not necessarily electrons) could be applied to other situations also. Planetary nebulae, for example, are believed to be illuminated by a central source or sources and are seen almost entirely in scattered (and hence highly polarised) light. Spectropolarimetric line profile observations of such objects exhibit similar spectral shapes to the scattering of stellar lines in an expanding envelope as studied above. Indeed the observed polarimetric line profiles have been attributed to line radiation from a central illuminating source scattering off dust grains (which may possess different angular phase functions from the Rayleigh phase function) in a radially expanding nebulae (Axon, 1993). One advantage of studying nebulae, as opposed to Be and Wolf Rayet stars, is that they are often spatially resolvable and the scattered polarimetric line profiles from different regions within the nebula may be isolated for subsequent analysis. It is therefore anticipated that the density and velocity fields at localised points within the nebula may be inferred from such observations – in a similar fashion to the stellar systems studied in this thesis – without having to make assumptions about the global structure of the nebula. As with stellar observations line spectropolarimetry of nebulae is still in its infancy, but will provide a powerful tool for probing the structure of extended scattering regions.

Another obvious system which may involve line scattering off moving particles is the polarisation of astrophysical jets. However, the situation is more complicated than any of the aforementioned systems in that the jets are often thought to be constrained by strong magnetic fields which may give rise to synchrotron polarisation in addition to any scattered polarisation. This topic is discussed further in Chapter 7.

#### 5.5.5 Forthcoming observing campaigns

Prompted in part by the renewed interest in the theoretical study of line polarisation and by the advent of more sensitive polarimeters several spectropolarimetric observational programs are currently on going or being planned.

Despite some calibration and mission problems a lot of interesting science has arisen from the ASTRO-1 mission which measured polarisation in the ultraviolet. ASTRO-2 is currently scheduled

for November 1994 and will investigate further UV continuum and line polarisation. Although the spectral resolution is rather low to detect the polarimetric variations predicted above a few polarimetric data points may be obtained across UV resonance lines thus enabling the general trends of polarisation and position angle variations to be studied and compared with theory. With so many lines occurring in the UV spectra of Be stars higher resolution spectropolarimeters are clearly required to exploit the wealth of information these lines contain.

High wavelength resolution observations (anticipated to be better than  $0.2\text{\AA}$ ) across  $H_\alpha$  in bright Be stars and across the Helium  $4686\text{\AA}$  line in the Wolf Rayet star EZ Canis Majoris (to complement the observations of Schulte-Ladbeck et al, 1990) are currently being collected by Anderson (1993) with a modified ECHELLE spectrograph from a 2.5m telescope at Kitt Peak. Work is nearing completion on the Wisconsin-Indianapolis-Yale-NOAO (WIYN) telescope, also at Kitt Peak, which will be collecting spectropolarimetric data by 1995.

In addition to the ASTRO-2 mission, two other UV-Polarimetry space missions are planned. The Wide-Field Imaging Survey Polarimeter (WISP) will obtain the first wide-field polarimetric images in the UV, while the Far-Ultraviolet Spectropolarimeter (FUSP) will explore the wavelength range shortward of that of WUPPE. Although only at low spectral resolution, the polarimetric data from these instruments, as with WUPPE, is expected to produce many interesting scientific discoveries and provide the impetus for much further theoretical modelling of polarisation in the UV.

## 6. Derivation of episodic mass loss functions for hot stars from polarimetric and absorption line data

### Summary

Expressions are derived for the time dependent continuum polarisation of starlight after (single) Thomson scattering in an axisymmetric envelope, and for the strength of an absorption line, in terms of integrals over the angular distribution and previous history of the stellar mass loss rate. Under the approximation of constant envelope expansion speed, and parametrising the mass loss angular distribution in terms of a time dependent equatorial concentration shape factor, it is shown that the resulting pair of integral equations has an explicit Fourier solution for the time dependence of the mass loss rate and shape, in terms of the polarisation and line strength 'light curves'. The method is illustrated for the simpler case of no 'shape' variations using both simulated data (Heavyside 'top hat' and oscillatory mass loss rates) and for real data. In the latter case, polarisation data on  $\omega$  Orionis were inverted for a series of values of the mass flow time (stellar radius/flow speed), which is a free parameter, and it was found that only flow times less than five days yield physically acceptable (non-negative) mass loss rates, because of the rapidity of data variations.

### 6.1 Introduction

The continuum polarisation of hot single stars (particularly Be stars) is commonly interpreted in terms of Thomson scattering of starlight in a flattened rotationally symmetric envelope produced by stellar mass loss through rotational, magnetic, pulsational or radiative driving forces. Time variability of the polarisation of such stars is well known to occur on a wide range of timescales and presumed to be related to variations in the rate and/or angular distribution of stellar mass loss. Starting from the observations of Hayes & Guinan (1984) and of Sonneborn et al (1987), Brown & Henrichs (1987) discussed how insight can be gained into the stellar mass loss variations. They emphasised that polarisation "light curves" alone cannot resolve the ambiguity between variations due to mass loss rate and those due to angular distribution (envelope shape). However, when absorption line variations are also observed (due to variations in optical depth along the line of sight to the star) these can be combined with variations in polarisation (due to changes in scattering optical depth along other directions from the star) to separate the changes in mass loss rate and geometry. The data on which Brown and Henrichs based their discussion were very limited, being undersampled relative to the observed timescale of variability (i.e. to either the timescale for changes in mass loss rate or for envelope outflow) but the description showed the potential value of more complete data of this type.

In this chapter the work of Brown & Henrichs is generalised, formulating the problem of

inference of mass loss distributions as an inverse problem (Craig & Brown, 1986) with the mass loss distribution in time and polar angle to be inferred from the observed polarimetric and absorption line strength variations. In the case of a fixed angular distribution, it is shown how the mass loss rate variations can be expressed analytically as an inversion of the continuum polarisation "light curve". When the angular distribution is also allowed to vary, it is shown that (under simplifying assumptions concerning the ionisation fraction of the element concerned) simultaneous data on absorption line strength variations permit analytic (Fourier) inference of the mass loss rate variations in both time and angle. Laplace and Integral Moment representations are also possible.

The numerical application of these analytic inversions to both simulated and real data is then considered. This is done by generating artificial data from input mass loss models and using these simulated "data" to see how well the input function can be recovered. Future work on this subject is discussed including the effect of noise in the data and the extent to which it is possible to recover different frequency components of the mass loss function. It is anticipated that, in common with all such inverse problems, the higher frequency components will be the most difficult to extract from noisy data since they are filtered by the integral kernel of the problem - in this case set by the timescale of mass outflow across a stellar radius.

## 6.2 Analytic formulation and solution

### 6.2.1 The forward problem

For an equatorially and axially symmetric envelope, at inclination  $i$  to the observer and of electron density  $n(r, \mu, t)$  at distance  $r$  and polar angle  $\theta = \cos^{-1} \mu$ , at time  $t$ , the net polarisation of light from an unpolarised star of radius  $R$  is (according to Brown & McLean 1977, with Cassinelli et al 1987 depolarisation factor added) - cf Chapter 1,

$$P(t) = \frac{3}{8} \sigma_T \sin^2 i \int_0^1 \int_R^\infty (1 - 3\mu^2) n(r, \mu, t) \sqrt{1 - \frac{R^2}{r^2}} dr d\mu, \quad (6.1)$$

where  $\sigma_T$  is the Thomson cross-section.

On the other hand the line of sight column density of resonance line absorbers of some ion  $A$ , which determines the absorption line strength, is (cf Brown & Henrichs, 1987, Eq. 3)

$$N_A(t) = A \int_R^\infty n(r, \cos i, t) q_A(r, \cos i, t) dr, \quad (6.2)$$

where  $A$  is the elemental abundance and  $q_A(r, \mu, t)$  is the ionisation fraction at  $(r, \mu, t)$ . In Eq. 6.2, strictly speaking an average should be taken across the face of the stellar disk, taken to be finite in Eq. 6.1, but this correction is neglected in the present analysis. It is seen that in this formalism the temporal variations in the polarisation arise through changes in the magnitude or shape of the envelope electron density while the absorption line strength variations are attributed to changes in the density and/or the ionisation fraction. As  $q_A$  changes with time the polarisation will also vary,

but this will be undetected since the envelopes of the hot stars under consideration are assumed to consist almost entirely of ionised Hydrogen so additional free electrons due to  $q_A$  variations of other less abundant elements will have little effect on the polarisation.

$n(r, \mu, t)$  can be expressed in terms of the stellar mass loss rate at an earlier (mass flow) time via the mass continuity equation provided the velocity field of the flow is known or can be assumed. Here all mass outflow is taken to be in the radial direction from the stellar centre, and the simplifying assumption is made that the flow speed,  $v$ , is everywhere a constant  $v_0$ . In practice  $v$  will increase rapidly just above the stellar surface - cf Sect. 2.4.2 - so this effectively assumes the acceleration zone to be thin enough as to make only a small contribution to  $P$  and  $N_A$ . Then the mass loss rate,  $\dot{M}_\mu$ , per unit  $\mu$  range from the stellar surface,  $r = R$ , at time  $t$  is related to  $n$  by,

$$2 \pi r^2 n(r, \mu, t) m_p v_0 = \dot{M}_\mu \left( \mu, t - \frac{r - R}{v_0} \right), \quad (6.3)$$

where  $m_p$  is the proton mass, so that Eqs. 6.1 and 6.2 become,

$$P(t) = \frac{3}{16\pi} \frac{\sigma_T}{m_p} \frac{\sin^2 i}{v_0} \int_0^1 \int_R^\infty (1 - 3\mu^2) \dot{M}_\mu \left( \mu, t - \frac{r - R}{v_0} \right) \sqrt{1 - \frac{R^2}{r^2}} \frac{dr d\mu}{r^2}, \quad (6.4)$$

$$N_A(t) = \frac{A}{2 \pi m_p v_0} \int_R^\infty \dot{M}_\mu \left( \cos i, t - \frac{r - R}{v_0} \right) q_A(r, \cos i, t) \frac{dr}{r^2}. \quad (6.5)$$

These equations are thus far quite general and the problem is that of inferring  $\dot{M}(\mu, t)$  from  $P(t)$  and  $N_A(t)$ . The problem is evidently underdetermined unless  $q_A(r, \mu, t)$  is known or assumed. Inclusion of substantial variations in  $q_A$  will certainly make the problem analytically intractable and here the only cases treated are those where  $q_A$  can be taken to have a near constant value,  $\bar{q}_A$ , over the spatial and temporal domains which contribute dominantly to  $P$  and  $N_A$ .

The mass loss rate is now expressed as,

$$\dot{M}_\mu(\mu, t) = S(\mu, t) \dot{M}_0(t), \quad (6.6)$$

where  $\dot{M}_0(t)$  is the equatorial mass loss rate per unit  $\mu$  and  $S$  is an envelope shape function.

Anticipating the limited extent to which envelope shape variations are ever likely to be inferable from real data - cf Section 6.3 - it is assumed that  $S(\mu, t)$  can be adequately described by the convenient parametric form,

$$S(\mu, t) = 1 - a(t) |\mu|^\alpha, \quad (6.7)$$

where the constant index  $\alpha$  measures the rate at which  $\dot{M}_\mu$  declines away from the equator and  $a(t)$  is a time dependent measure of the global envelope oblateness with  $(1 - a)$  equal to the ratio of polar to equatorial mass loss rates. ( $a$  must be less than 1, with  $a < 0$  corresponding to prolate envelopes, assuming  $\alpha > 0$ .)

With assumptions 6.6 and 6.7, Eqs. 6.4 and 6.5 become, on integrating over  $\mu$  in Eq. 6.4,

$$P(t) = \frac{3\alpha}{8\pi(\alpha+1)(\alpha+3)} \frac{\sigma_T}{m_p} \frac{\sin^2 i}{v_0} \int_R^\infty \dot{M}_0(t') a(t') \sqrt{1 - \frac{R^2}{r^2}} \frac{dr}{r^2}, \quad (6.8)$$

$$N_A(t) = \frac{A\bar{q}_A}{2\pi m_p v_0} \int_R^\infty \dot{M}_0(t') (1 - a(t') \cos^\alpha i) \frac{dr}{r^2}, \quad (6.9)$$

where  $t' = t - (r - R)/v$ .

Inspection of Eqs. 6.8 and 6.9 shows that the problem has now been reduced to inversion of two data sets  $P(t)$  and  $N_A(t)$  to find the two unknown functions  $\dot{M}_0(t')$  and  $a(t')$ . Solutions should therefore be possible for prescribed values of the parameters  $v_0$ ,  $R$ ,  $i$  and  $\alpha$ . If any of these are unknown, solutions can be sought over plausible parameter ranges and those parameters and solutions taken as acceptable when the resulting  $\dot{M}_0(t')$ ,  $a(t')$  are physically meaningful (i.e.  $\dot{M}_0 > 0$  and  $a < 1$  respectively).

To reduce the problem to its underlying dimensionless mathematical form, and, to reveal the dimensional variables which characterise the physics, Eqs 6.8 and 6.9 are cast into dimensionless form by means of the dimensionless variables,

$$x = \frac{r}{R} - 1, \quad (6.10)$$

$$\tau = \frac{t}{\frac{R}{v_0}}, \quad (6.11)$$

$$m(\tau') = \frac{\dot{M}_0(t') R \sigma_T}{m_p v_0 R^2}, \quad (6.12)$$

$$F(\tau) = P(t) / \frac{3\alpha \sin^2 i}{8\pi(\alpha+1)(\alpha+3)}, \quad (6.13)$$

$$G(\tau) = N_A(t) / \frac{A\bar{q}_A}{2\pi\sigma_T}, \quad (6.14)$$

in terms of which Eqs. 6.8 and 6.9 become,

$$F(\tau) = \int_0^\infty m(\tau') a(\tau') \frac{\sqrt{x(x+2)}}{(x+1)^3} dx, \quad (6.15)$$

$$G(\tau) = \int_0^\infty m(\tau') (1 - a(\tau') \cos^\alpha i) \frac{dx}{(x+1)^2}, \quad (6.16)$$

where the dimensionless retarded time  $\tau'$  is given by,

$$\tau' = t' / \frac{R}{v_0} = \tau - x. \quad (6.17)$$

Alternatively, Eqs. 6.15 and 6.16 can be expressed in terms of integrals of the mass loss history over the time  $\tau'$  elapsed till the present  $\tau$ , viz,

$$F(\tau) = \int_{-\infty}^\tau \{m(\tau') a(\tau')\} \frac{\sqrt{(\tau - \tau')(\tau - \tau' + 2)}}{(\tau - \tau' + 1)^3} d\tau', \quad (6.18)$$

$$G(\tau) = \int_{-\infty}^{\tau} \{m(\tau') [1 - a(\tau') \cos^{\alpha} i]\} \frac{d\tau'}{(\tau - \tau' + 1)^2} . \quad (6.19)$$

### 6.2.2 Inverse Fourier solution

Equations 6.15 and 6.16, or equivalently 6.18 and 6.19, are integral equations for the two functions contained in the { } terms of the integrands, viz,

$$f(\tau') = m(\tau') a(\tau') . \quad (6.20)$$

$$g(\tau') = m(\tau') [1 - a(\tau') \cos^{\alpha} i] , \quad (6.21)$$

and it is clear that if solutions can be found for  $f(\tau')$ ,  $g(\tau')$  from data on  $F(\tau)$ ,  $G(\tau)$  then  $m(\tau')$ ,  $a(\tau')$  are determined for any  $i$  value adopted, viz,

$$m(\tau') = g(\tau') + f(\tau') \cos^{\alpha} i . \quad (6.22)$$

$$a(\tau') = \left( \cos^{\alpha} i + \frac{g(\tau')}{f(\tau')} \right)^{-1} . \quad (6.23)$$

In addition the integral equations for  $f$  and  $g$  are of the same generic convolution type, and can be written in the form,

$$\phi(\tau) = \int_0^{\infty} \psi(\tau - x) \lambda(x) dx = \int_{-\infty}^{\tau} \psi(\tau') \lambda(\tau - \tau') d\tau' , \quad (6.24)$$

where the  $\lambda$ 's corresponding to the equations for  $f$  and  $g$  are defined as,

$$\lambda_f(x) = \frac{\sqrt{x(x+2)}}{(x+1)^3} , \quad \lambda_g(x) = (x+1)^{-2} \quad x \geq 0 , \quad (6.25a)$$

$$\lambda_f(x) = 0 \quad , \quad \lambda_g(x) = 0 \quad x < 0 . \quad (6.25b)$$

Full solution of Eq. 6.24 for  $\psi(\tau')$  for any time  $\tau' < \tau_0$  would require data on  $\phi(\tau)$  for all  $\tau < \tau_0$  which is in practice impossible and, for solution from data on some finite interval, it is necessary to make some assumption on the behaviour of the data  $\phi$ , or of the unknown function  $\psi$ , formally for all time prior to the start of observations. (Physically this is because the initial data value could arise in an infinity of different ways - eg a large mass loss just before  $\tau = 0$  or a slow mass loss over a long period before  $\tau = 0$ , these two situations influencing the data evolution at  $\tau > 0$  in different ways.) In the absence of any prior knowledge of  $f$  at  $\tau < 0$ , the most reasonable assumption seems to be that  $\psi(\tau')$  (i.e. both  $\dot{M}$  and  $a$ ) were constant on  $\tau' < 0$  or, equivalently, that the  $\phi$ 's (ie both  $P$  and  $N_A$ ) were constant. Because of the  $x^{-2}$  asymptotic behaviour of the  $\lambda$ 's, this in practice only requires that  $\dot{M}$  and  $a$  have been constant over a substantial number of

flow times,  $\tau_f = R/v_0$ , prior to the time dependent  $P$ ,  $N_A$  episodic outburst being analysed. In the case where  $P$  and  $N_A$  are actually zero at the start of observation, this assumption will be exactly true. In cases where this is not the case, the assumption is equivalent to replacing  $\phi(\tau)$  by  $\phi(\tau) - \phi(0)$  (i.e.  $P(t)$  by  $P(t) - P(0)$  and  $N_A(t)$  by  $N_A(t) - N_A(0)$  and solving for  $\dot{M}(t)$  and  $a(t)$  corresponding to the episodic contributions only). Henceforth it is assumed that the data has been processed to give this meaning for  $\phi(\tau)$  (i.e. for  $P(t)$ ,  $N_A(t)$ ).

The first form of Eq. 6.24 is now considered and the unknown functions  $\psi$  are expressed as Inverse Fourier Transforms according to,

$$\psi(\tau') = \int_{-\infty}^{\infty} \Psi(\nu) e^{2\pi i \nu \tau'} d\nu, \quad (6.26)$$

which, on substitution in Eq. 6.24 yields,

$$\phi(\tau) = \int_{-\infty}^{\infty} \Psi(\nu) \Lambda(\nu) e^{2\pi i \nu \tau} d\nu, \quad (6.27)$$

where  $\Lambda(\nu)$  is the Fourier Transform of  $\lambda(x)$  given by,

$$\Lambda(\nu) = \int_{-\infty}^{\infty} \lambda(x) e^{-2\pi i \nu x} dx. \quad (6.28)$$

Equation 6.27 shows  $\phi(\tau)$  to be the Inverse Fourier Transform of  $\Psi\Lambda$  so that if  $\Phi(\nu)$  is the Fourier Transform of the data function  $\phi$ ,

$$\phi(\tau) = \int_{-\infty}^{\infty} \Phi(\nu) e^{2\pi i \nu \tau} d\nu, \quad (6.29)$$

then,

$$\Psi(\nu) \Lambda(\nu) = \Phi(\nu). \quad (6.30)$$

Consequently the Fourier solution of Eq. 6.24 is,

$$\psi(\tau') = \mathcal{F}^{-1} \left\{ \frac{\Phi(\nu)}{\Lambda(\nu)}; \tau' \right\} = \mathcal{F}^{-1} \left\{ \frac{\mathcal{F}\{\phi(\tau); \nu\}}{\mathcal{F}\{\lambda(x); \nu\}}; \tau' \right\}, \quad (6.31)$$

where  $\mathcal{F}$ ,  $\mathcal{F}^{-1}$  denote the direct and inverse Fourier Transforms. Laplace and Integral Moment solutions are also possible - see Sect. 6.4.

## 6.3 Numerical results

### 6.3.1 Discretisation procedure

In the inversion of polarisation data only the Fourier Transform of the function  $\lambda_f(x)$ , defined by Eq. 6.25, is required. This cannot be done analytically, so the transform is computed by a *Fast Fourier Transform* (FFT) routine.  $\Lambda(\nu)$ , the Fourier Transform of  $\lambda_f(x)$ , may be approximated by representing  $\lambda_f(x)$  over a large enough interval to allow the dominant frequency components to be obtained and choosing a small enough step size to resolve any features in the curve. By choosing

the step size to be  $\Delta$  and calculating  $\lambda_j(x_j)$  for  $x_j = j\Delta$  ( $j$  in the range 0 to  $N-1$ ), then the FFT algorithm may be applied to these points. Now, if  $\lambda_f(x)$  is represented over the range  $C$  of  $x$ ,  $\Lambda(\nu)$  may be approximated by,

$$\Lambda(\nu) \approx \frac{C}{N} \sum_{j=0}^{N-1} \lambda_j e^{-2\pi i \nu j C/N}, \quad (6.32a)$$

$$\Lambda_k \approx \frac{C}{N} \sum_{j=0}^{N-1} \lambda_j e^{-2\pi i j k/N}, \quad (6.32b)$$

where  $\lambda_j = \lambda_f(jC/N)$ ,  $\Lambda_k = \Lambda(k/C)$ ,  $C = (N-1)\Delta$ , and  $k$  is in the range 0 to  $N-1$ .

A typical FFT routine calculates,

$$Z_k = \frac{1}{\sqrt{N}} \sum_{j=0}^{N-1} \lambda_j e^{-2\pi i j k/N}, \quad (6.33)$$

so  $\Lambda(\nu)$  is approximated by,

$$\Lambda(\nu) \approx \Lambda_k = \frac{C}{\sqrt{N}} Z_k. \quad (6.34)$$

Now, the polarisation data is given at points  $p(x_{pl})$  where  $x_{pl} = l\Delta_P$  ( $l$  in the range 0 to  $N_P-1$ ), with  $N_P$  the number of data points. The approximation to the Fourier Transform of this data is then given by,

$$P(\nu_P) \approx \frac{C_P}{N_P} \sum_{l=0}^{N_P-1} p_l e^{-2\pi i \nu_P l C_P/N_P}, \quad (6.35)$$

$$P_m \approx \frac{C_P}{N_P} \sum_{l=0}^{N_P-1} p_l e^{-2\pi i l m/N_P}, \quad (6.36)$$

where  $p_l = p(x_{pl})$ ,  $P_m = P(m/C_P)$ ,  $C_P = (N_P-1)\Delta_P$ , and  $m$  is in the range 0 to  $N_P-1$ .

In the inversion  $P_m/\Lambda_m$  is required. Now,  $P$  is calculated at frequencies  $m/C_P$  ( $m$  in the range 0 to  $N_P-1$ ), while  $\Lambda$  is calculated at frequencies  $k/C$  ( $k$  in the range 0 to  $N-1$ ). The values of  $\Lambda$  are required at the same frequencies as those at which  $P$  is given to form the ratio  $P/\Lambda$ . Given the values  $\Lambda(k/C)$  ( $k$  in the range 0 to  $N-1$ ), an interpolation routine is used to give  $\Lambda(m/C_P)$  ( $m$  in the range 0 to  $N_P-1$ ), thus enabling  $P_m/\Lambda_m$  to be formed.

### 6.3.2 Illustrative results

Here the basic method will be illustrated by considering the case of polarisation data  $P(t)$  only, and solving Eq. 6.8 alone. This will yield the product  $m(\tau') a(\tau')$  (Eq. 6.15) which will correspond to the relative variations in  $\dot{M}_0(t')$  for constant shape  $a(t')$ , for any assumed values of the parameters  $R$ ,  $R/v_0$ , appearing in Eq. 6.12.

Figures 6.1(a) and 6.2(a) show the results obtained for simulated  $F(t)$  (*i.e.*  $P(t)$ ) data, obtained from Eqs. 6.8 and 6.13 for forms of  $\dot{M}_0(t)$  which are, respectively, top hat, and an oscillatory function, viz,

$$\dot{M}_0(t) = \dot{M}_0, \quad 0 \leq t \leq T \quad ; \quad 0, \quad t > T, \quad (6.37)$$

$$\dot{M}_0(t) = \dot{M}_0 \left[ 1 + \sin \left( \frac{6\pi}{T} t - \frac{\pi}{2} \right) \right], \quad 0 \leq t \leq T \quad ; \quad 0, \quad t > T, \quad (6.38)$$

where  $T = 10$ .

These figures show clearly the smoothing action of the flow time kernel function on  $P(t)$  as compared to  $\dot{M}_0(t)$ . Figures 6.1(b) and 6.2(b) show the original forms of 6.37 and 6.38 of  $\dot{M}_0(t)$  together with the forms recovered using the inversion method. It can be seen that the recoveries are quite good, but do show the effects of discretisation and truncation since no regularisation has been employed here. They also show the effect of ‘ringing’ in the recovery due to the effect of sharp edges and the finite interval used.

The same method has been applied to the polarimetric outburst data of Sonneborn et al (1987) on  $\omega$  Orionis. though their limited data on UV absorption line strength around the same period (Fig. 6.3) do indicate that the mass loss distribution does change shape as well as the rate (Sonneborn et al, Brown & Henrichs, 1987). Their data has been inverted (after some interpolation to yield uniform intervals) for several values of the flow time parameter  $\tau_f = R/v_0$ , with the results shown in Fig. 6.3(b). For very large values of  $v_0$ , the solution for the shape of  $\dot{M}_0(t)$  becomes independent of  $v_0$  (though the absolute  $\dot{M}$  values increase as  $v_0$  increases to maintain the density,  $n$ , demanded by the degree of polarisation). This is the continuous high speed ejection limit, described by Brown & Henrichs, where the flow time is much shorter than the time scale of  $\dot{M}$  variations and/or the data sampling rate, so that  $P(t)$  directly reflects  $\dot{M}_0(t)$ . As  $v_0$  is decreased, for a given  $R$ , the slower flow time increasingly smears  $P(t)$  compared to  $\dot{M}_0(t)$  and increasingly large and rapid changes in  $\dot{M}_0(t)$  are required to produce features in  $P(t)$ . For sufficiently small  $v_0$ , it becomes impossible to reproduce some of the changes in  $P(t)$  without obtaining unphysical negative values of  $\dot{M}_0(t)$  in the solution. For  $\omega$  Orionis this occurs at  $\tau_f \approx 5$  days, corresponding to a minimum mass flow speed  $v_0 \approx 14 \text{ km s}^{-1}$  for a stellar radius of  $R = 8.8 R_\odot$ , (suggested by Sonneborn et al). For a value of  $a = 1$ ,  $R = 8.8 R_\odot$ ,  $v_0 = 140 \text{ km.s}^{-1}$ ,  $i = 90^\circ$  and with  $\alpha$  of say 2, the peak in Fig. 6.3(b) corresponds to an actual mass loss rate,  $\dot{M}_{\text{TOT}}$ , of  $\approx 2.5 \cdot 10^{-7} M_\odot \cdot \text{yr}^{-1}$ , while taking the minimum speed, implied from unphysical solutions, the total mass loss rate is  $\approx 2.5 \cdot 10^{-8} M_\odot \cdot \text{yr}^{-1}$ , both values being within the range generally accepted for Be stars.

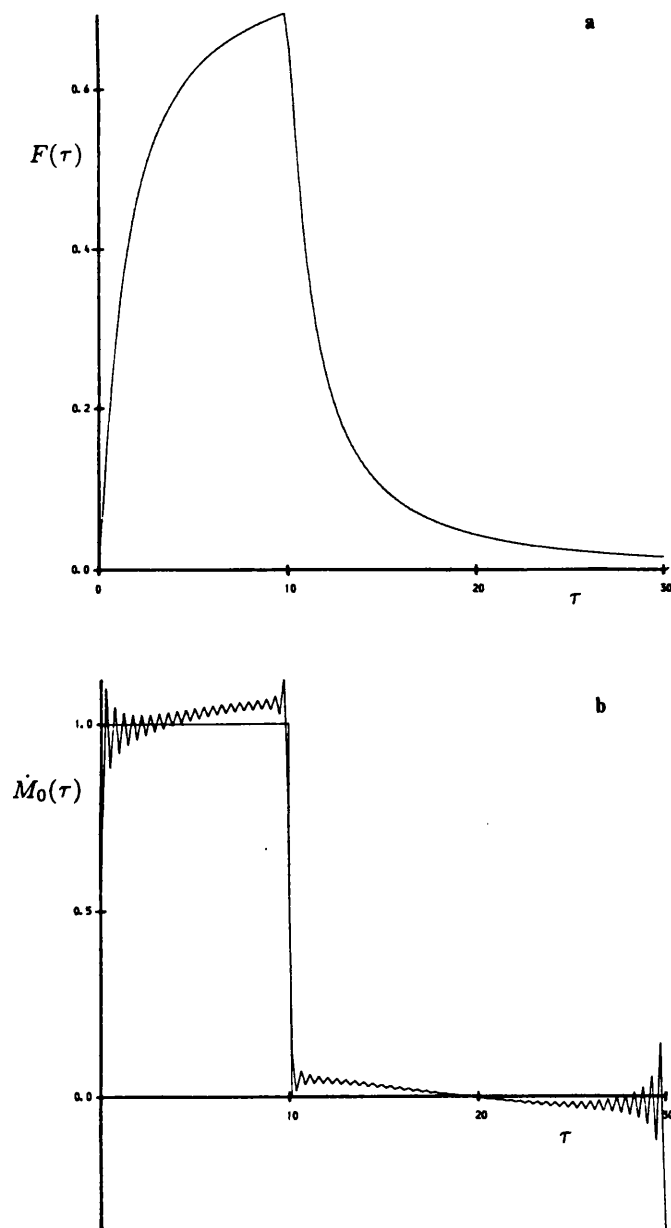


**Fig. 6.1** (a)  $F(\tau)$  calculated for the mass loss function given by Eq. 6.37. (b) Input mass loss function of Eq. 6.14 and its Fourier recovery from the finite interval simulated polarisation data presented in (a).

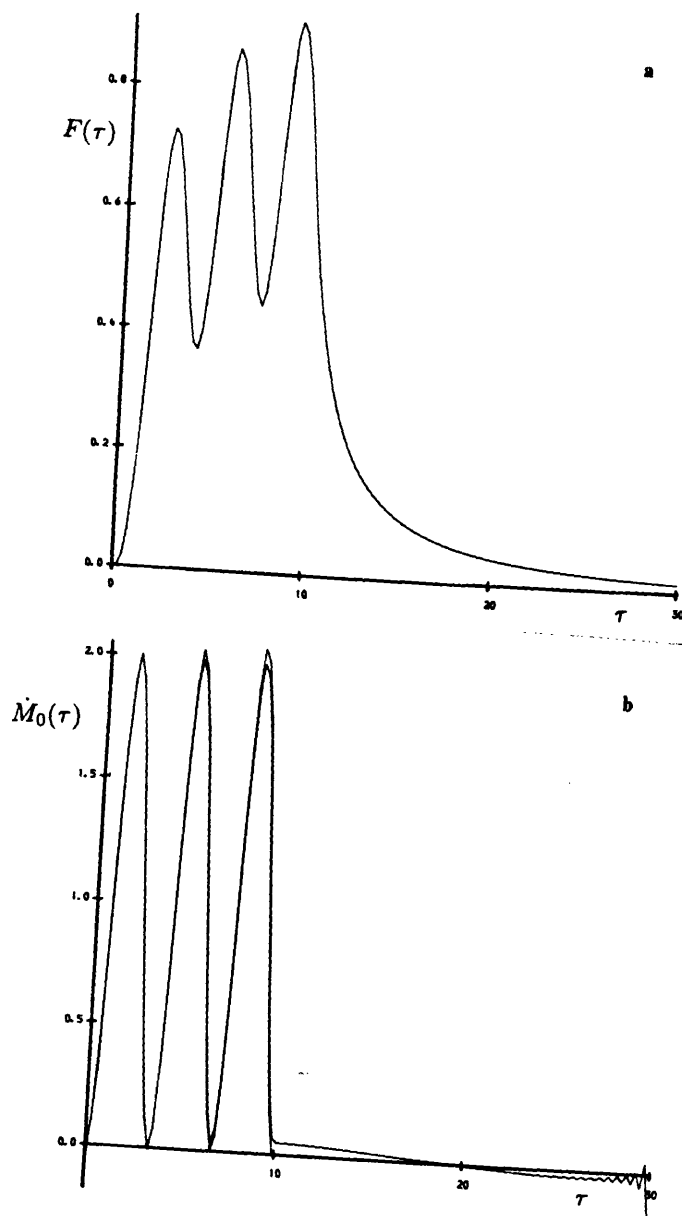
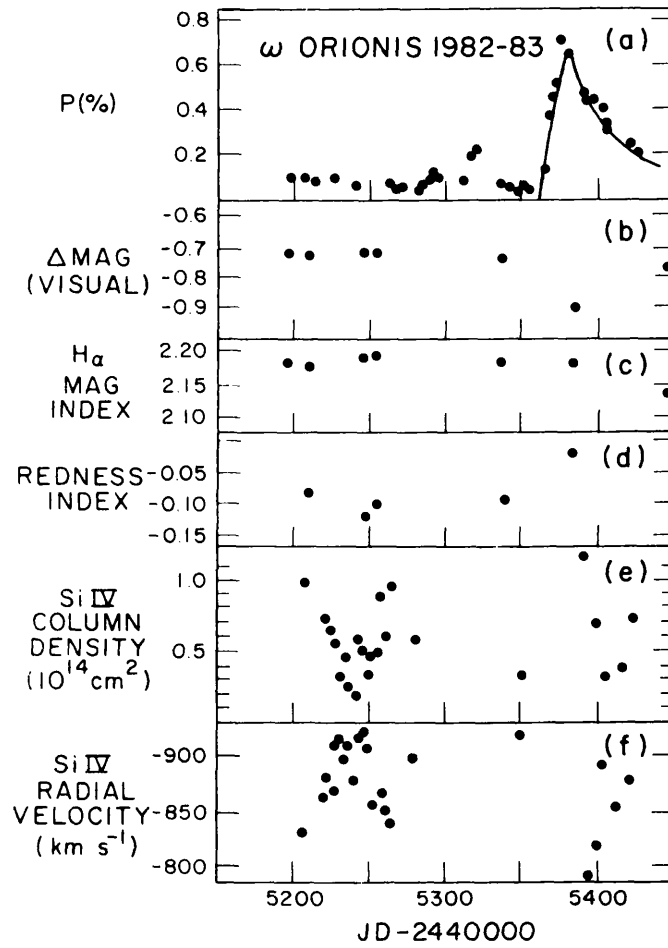


Fig. 6.2 As for Fig. 6.1, but for a mass loss function given by Eq. 6.38.



**Fig. 6.3** Polarisation and absorption line strength data for  $\omega$  Orionis from Brown and Henrichs, 1987

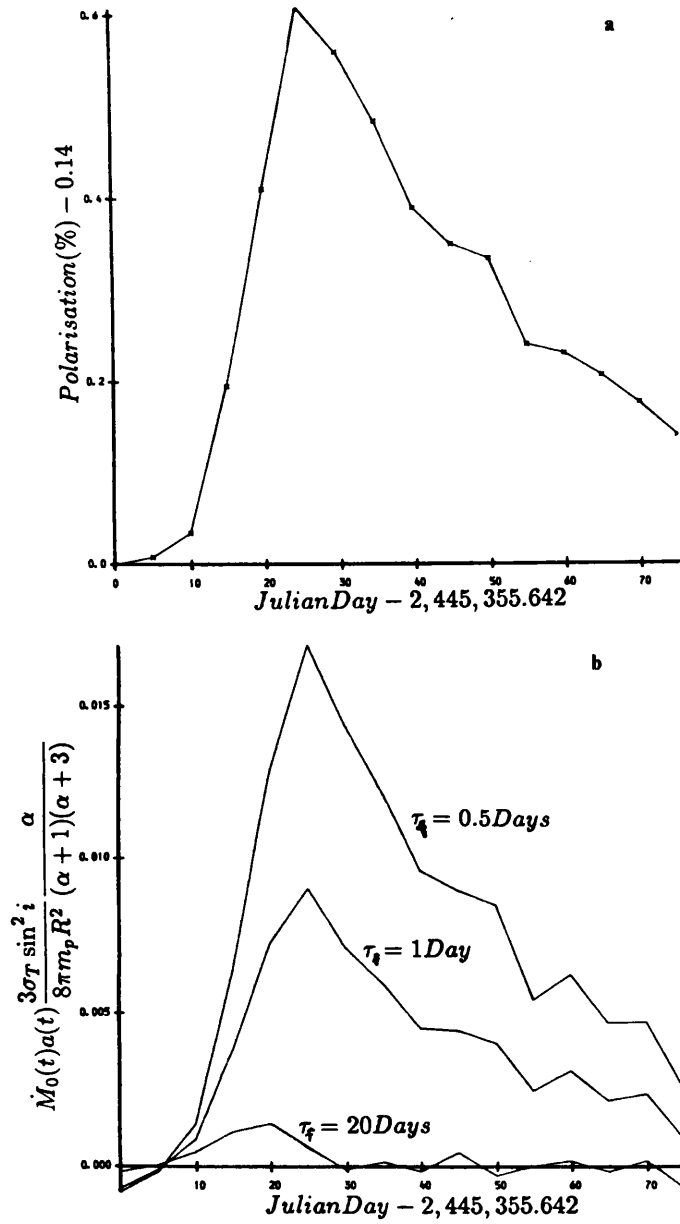


Fig. 6.4 (a) Sonneborn et al polarisation data for  $\omega$  Orionis shifted to zero on each axis. (b) Recovered mass loss function from inversion of Sonneborn et al data for flowtimes of 0.5, 1 and 20 days.

## 6.4 Other analytic solutions

### 6.4.1 Laplace solution

If Eq. 6.24 is considered in its second form, with  $\phi(\tau)$  again assumed to mean  $\phi(\tau) - \phi(0)$  for  $\tau > 0$  and 0 for  $\tau < 0$ . then,

$$\phi(\tau) = \int_0^{\infty} \psi(\tau') \lambda(\tau - \tau') d\tau', \quad (6.39)$$

which, on Laplace transformation yields,

$$\tilde{\Phi}(s) = \tilde{\Psi}(s) \tilde{\Lambda}(s), \quad (6.40)$$

where  $\tilde{\Phi}$  is the Laplace Transform of  $\phi$  given by,

$$\tilde{\Phi}(s) = \int_0^{\infty} \phi(\tau) e^{-s\tau} d\tau, \quad (6.41)$$

with solution,

$$\Psi(\tau') = \mathcal{L}^{-1} \left\{ \frac{\mathcal{L}\{\phi(\tau); s\}}{\mathcal{L}\{\lambda(x); s\}}; \tau' \right\}, \quad (6.42)$$

where  $\mathcal{L}, \mathcal{L}^{-1}$  are Laplace and Inverse Laplace Transforms. (Removal of the constant  $\phi(\tau)$  at  $\tau < 0$  has enabled expression of 6.24 in the form 6.39, and thus application of the convolution theorem.)

### 6.4.2 Integral moment solution

Because the kernel of 6.39 is a function of  $\tau - \tau'$ , an Integral Moment Solution is possible (Craig and Brown 1986) by means of a logarithmic change of variables  $\tau = \ln \xi$ ,  $\tau' = \ln \xi'$  so that,

$$X(\xi) = \int_{-\infty}^{\xi} Y(\xi') K \left( \frac{\xi}{\xi'} \right) d\xi', \quad (6.43)$$

where,

$$X(\xi) = \phi(\ln \xi), \quad (6.44)$$

$$Y(\xi) = \frac{\psi(\ln \xi')}{\xi'}, \quad (6.45)$$

and defining,

$$\langle X \rangle_j = \int_{-\infty}^{\infty} X(\xi) \xi^j d\xi, \quad (6.46)$$

then the similarly defined moments of  $Y(\xi')$  can be found in terms of  $X$ , viz,

$$\langle Y \rangle_j = \frac{\langle X \rangle_{j-1}}{K_{j-1}}, \quad (6.47)$$

where,

$$K_j = \int_1^{\infty} K(\eta) \eta^j d\eta. \quad (6.48)$$

These moments of  $X$  and  $Y$  correspond to 'moments' of the physical variables  $\phi(\tau)$ ,  $\psi(\tau)$  on an exponentially scaled time basis, which makes sense because (for example) the polarisation

changes, as mass ejected moves outward, at a rate which declines ever more slowly in time with increasing distance. In practice this solution will yield a 'mean' time, a temporal 'width' (variance) and a skewness in time etc. of those combinations of the mass loss functions  $m(t)$ ,  $a(t)$  defined in Eqs. 6.20 and 6.21, and on an exponential time basis.

### 6.5 The effects of noise in the data

The inversion method and the examples presented in this chapter illustrate the possibility of determining mass loss rate variations by analysing *exact* polarimetric and absorption line data. In practice the data and hence solution will be subject to noise and account must be taken of this also. The errors to be expected in the Fourier inversion may be estimated from the error analysis and discussion presented by Craig & Brown (1986, p48–51).

When taking the Fourier Transform of real data noise contamination manifests itself in high frequency components (which are required to reproduce any rapid variations present in the data). The "filtering out" of these high frequency components and the optimum procedure to be implemented is a non trivial problem in numerical analysis and there have been many papers on this subject in recent years (e.g. Thompson, et al, 1989). The simplest and most extreme technique is to simply neglect the contributions from all frequencies above a prescribed value in the Fourier Transform of the data. Other techniques include multiplying the Fourier Transform by a function which smoothly reduces the magnitude of the high frequency components to zero (the so called cosine or Gaussian "bell" techniques) and adaptive smoothing algorithms in which parameters are chosen via an iterative procedure so as to minimise the error in the final solution. Each of the aforementioned techniques influence the solution in different ways – see Craig & Brown, for example, for a discussion of these procedures.

### 6.6 An alternative inversion strategy

At present there is very limited line strength data available during the observed polarimetric outbursts presented above and so as to enable inversion of polarimetric data alone simplifying assumptions were made as to the shape of the stellar mass loss. However, if an equation for some other observable involving the mass loss rate could be determined then this could be combined with the equation for the time dependence of the polarisation and solved to yield the temporal variations in the rate and shape of stellar mass loss. A possible handle on the mass loss rate lies in the size of the polarisation Balmer "jump". Thomson scattering results in a flat polarisation spectrum, but absorption of stellar radiation due to Hydrogen continuum opacity ( $\sim \lambda^3$  with discontinuities across series limits) modifies this. The resultant polarisation from a Thomson scattering envelope in which Hydrogen is the dominant source of opacity decreases with increasing wavelength shortward of any series limits with a sudden increase (the jump) on crossing the limit (see Fig. 1.5). This effect is evident in data collected collected at Pine Bluff Observatory, Wisconsin (Bjorkman, 1993) around

the Balmer edge ( $\sim 3600\text{\AA}$ ). If the observed polarimetric outbursts are indeed attributable to the injection of ionised Hydrogen into the stellar envelope (with the envelope temperature effecting the ionisation level) then the size of the polarisation Balmer jump would be expected to vary with time during these outbursts as more Hydrogen able to absorb to different levels is ejected into the envelope. This problem may not possess an analytic solution as was the case when the polarimetric and line strength variations were analysed together, but a numerical solution may be obtained for comparison with the Fourier solution.

## 7. Polarisation from relativistic electron scattering

### Summary

The mathematical framework required to treat the problem of scattering radiation off relativistic electrons in a concise manner – four-vector calculus – is briefly outlined. Following on from this a preliminary investigation is conducted to determine the polarisation of radiation scattered off relativistic electrons for the simplest case of a narrow, constant velocity jet and an unpolarised source. It is shown that if scattering is the only source of the jet's polarisation then the velocity and angle which the jet makes to the line of sight may be determined from analysis of the polarisation and Doppler shift of spectral features in the source which are scattered in the jet. A discussion is then given as to the effects of contamination of the scattered radiation by synchrotron radiation from the jet.

### 7.1 Introduction

Recent models have investigated the role of electron-positron ( $e^\pm$ ) plasmas in astrophysical jets (Dermer, 1992, Ghisleni et al, 1992). These models have focussed primarily on the intensity of radiation (first Stokes parameter) emitted by the jets, produced by either the synchrotron mechanism or (inverse) Compton scattering of photons from a central source off the  $e^\pm$  pairs in the jet. It is well known that synchrotron radiation can exhibit high levels of linear polarisation, but to date little consideration has been given to the polarisation produced by scattering.

In an  $e^\pm$  plasma both the electrons and the positrons contribute equally to photon scattering, and hence to the polarisation of the scattered radiation. In such a plasma it is possible to accelerate the charged particles to highly relativistic speeds, which makes a relativistic treatment of the scattering imperative.

In this chapter the equations for the scattering cross-sections are formulated using previous analysis involving four-vector calculus. The formulation allows one to determine the cross-sections in any frame – e.g. the Klein-Nishina cross-section is calculated in the electron's rest frame. However, in this analysis the observer's frame is considered and the polarisation is calculated for the most relevant example, in the context of relativistic jets, where the electron's motion is along the direction of propagation of the incident radiation (i.e. the photons "catch-up" on the electron).

A relativistic spinor formulation of the Stokes parameters and the application to Compton scattering was presented by De Young (1966). While the method employed below may not be as elegant as De Young's analysis it yields the same results and the use of polarisation four-vectors in the analysis provides the basis for a pictorial representation of what can be a rather complex

problem in relativistic scattering theory.

## 7.2 Four-vector calculus

Due to certain properties the calculus of four-vectors (and more generally tensor calculus) provides a very elegant framework for the theoretical investigation of relativistic kinematics. This section presents a brief introduction to four-vectors and some of their properties.

### 7.2.1 Definition of a four-vector

As its name would suggest a four-vector consists of four components – one “time” and three “spatial” components. These components do not necessarily have the dimensions of time and space, but they do obey the same Lorentz transformation rules as a displacement vector in spacetime, hence the nomenclature. In general a four-vector may be represented as,

$$a^\mu = (a^0, a^1, a^2, a^3) = (a^0, \mathbf{a}), \quad (7.1)$$

where  $a^0$  is the time component and the spatial components have been written as the Euclidean vector  $\mathbf{a} = (a^1, a^2, a^3)$  in the second representation of Eq. 7.1. The Greek suffix,  $\mu$ , (or any other Greek letter) indicates that  $a$  has four components and is standard notation. In this notation the displacement vector in spacetime (or the four-radius vector),  $x^\mu$ , has as its components  $x^0 = ct$ , where  $t$  is the time, and  $(x^1, x^2, x^3)$  is the three dimensional displacement vector. One of the most common four-vectors in relativistic kinematics which shall be used in the formulation below, is the momentum four-vector,  $p^\mu$ , with components,

$$p^\mu = (p^0, p^1, p^2, p^3) = (E/c, \mathbf{p}), \quad (7.2)$$

where  $E = \gamma m_0 c^2$  is the total energy of the particle,  $m_0$  is the particle rest mass,  $\gamma = 1/\sqrt{1 - \beta^2}$  and  $\beta c$  is the particle velocity.  $\mathbf{p} = (p^1, p^2, p^3) = \gamma m_0 c \boldsymbol{\beta}$  is the particle's component momentum along the directions  $(x^1, x^2, x^3)$ . As stated above these components transform as a time ( $E/c$ ) and a spatial vector ( $\mathbf{p}$ ). For a photon, which has zero mass, the 4-momentum,  $k^\mu$ , is,

$$k^\mu = \frac{h\nu}{c} (1, \hat{\mathbf{k}}), \quad (7.3)$$

where  $\hat{\mathbf{k}}$  is a unit vector in the direction of propagation of the photon. Equation 7.3 arises since for a photon  $E = h\nu$  and  $\mathbf{p} = E/c \hat{\mathbf{k}}$ , where  $h$  is Planck's constant and  $\nu$  is the photon frequency.

### 7.2.2 Some properties of four-vectors

Using the metrical tensor, whose components are defined below, it is straightforward to transform between the contravariant and covariant forms of any four-vector, viz,

$$a_\mu = g_{\mu\nu} a^\nu, \quad (7.4)$$

where a repeated index implies a summation over that index and the metrical tensor has components  $g_{00} = 1$ ,  $g_{11} = g_{22} = g_{33} = -1$  and all other components are zero. The components of the metrical tensor satisfy the condition,

$$g^{\mu\alpha} g_{\alpha\nu} = \delta_{\nu}^{\mu} . \quad (7.5)$$

Using these properties the scalar (or dot) product of two four-vectors is,

$$a_{\mu} b^{\mu} = a_0 b^0 + a_1 b^1 + a_2 b^2 + a_3 b^3 = a_0 b_0 - a_1 b_1 - a_2 b_2 - a_3 b_3 = a_0 b_0 - \mathbf{a} \cdot \mathbf{b} . \quad (7.6)$$

For notational convenience the Greek suffices on the four-vectors are often suppressed allowing Eq. 7.6 to be written in the form,

$$a \cdot b = a_{\mu} b^{\mu} . \quad (7.7)$$

A property of great relevance is that the scalar product of two four-vectors, Eq. 7.6, is itself a Lorentz invariant (i.e. has the same value in *any* inertial reference frame).

The classical law for the conservation of momentum has the following analagous four-vector form, namely,

$$\sum_{i=1}^n p_i = \sum_{i=1}^n p'_i , \quad (7.8)$$

where the unprimed and primed four-momenta refer to the values of the energy and momentum before and after any interaction of the  $n$  particles. Here the Greek suffices have again been suppressed for notational convenience.

### 7.2.3 Polarisation four-vectors

In quantum theory particles may be represented by "wave functions" and for a photon the wave function is a four-vector of the form,

$$A^{\mu} \sim e^{\mu} \exp -i k_{\nu} x^{\nu} , \quad (7.9)$$

where  $A^{\mu}$  is the four-potential,  $e^{\mu}$  satisfies the condition,

$$e_{\mu} e^{\mu} = -1 , \quad (7.10)$$

and the photon four-momentum (cf Eq. 7.3) satisfies

$$k_{\mu} k^{\mu} = 0 . \quad (7.11)$$

The above may be written more concisely by suppressing the four-dimensional vector indices, viz,

$$A \sim e \exp -i k \cdot x \quad e \cdot e = -1 , \quad (7.12)$$

where  $k \cdot x = h\nu/c(t - \hat{\mathbf{k}} \cdot \hat{\mathbf{x}})$  and  $e^{\mu}$  or more simply,  $e$ , is the unit polarisation four-vector.  $A^{\mu}$  is not observable, but the observables are the electric and magnetic fields which are components of the antisymmetric electromagnetic field tensor formed thus,

$$F_{\mu\nu} = \partial_{\mu} A_{\nu} - \partial_{\nu} A_{\mu} , \quad (7.13)$$

where  $\partial_\mu$  is the partial four-derivative  $\partial/\partial x^\mu$ . From Eq. 7.13 it is seen that  $A_\mu$  can undergo the transformation,

$$A_\mu \rightarrow A_\mu + \partial_\mu \chi, \quad (7.14)$$

where  $\chi$  is an arbitrary function of the coordinates, without changing its physical significance in any way. This property is known as *Gauge Invariance*. The choice of the *Lorentz Gauge*,  $\partial_\mu A^\mu = 0$ , implies  $\epsilon_\mu k^\mu = 0$ . In this gauge all physical results will be invariant under the transformation,

$$e^\mu \rightarrow e^\mu + \alpha k^\mu, \quad (7.15)$$

where  $\alpha$  is an arbitrary constant. From Eq. 7.15 it is clear that it is always possible to choose a gauge in which  $e^0 = 0$  then  $\mathbf{e} \cdot \hat{\mathbf{k}} = 0$  - i.e. the spatial components of the polarisation four-vector are perpendicular to the direction of photon propagation. This is known as the *transverse gauge* and is utilised throughout the remainder of this chapter.

The theory outlined above, while by no means complete, is the minimum required for the problem of Compton scattered polarisation considered below.

### 7.3 Compton scattering theory

The quantum theory of scattering cross sections requires the calculation of various matrix elements which can be quite tedious (e.g. Jauch & Rohrlich, 1976). A full theoretical investigation of these matrices is beyond the scope of this thesis and only the final results, which may be found in most quantum theory texts, are presented here.

The differential cross section per unit solid angle for Compton scattering a photon from an initial to final polarisation state is (Jauch & Rohrlich, 1976, Chapter 11),

$$\frac{d\sigma}{d\Omega} = \frac{3\sigma_T}{16\pi} \frac{X}{\gamma^2(1-\beta\cos\alpha)^2} \left(\frac{\nu'}{\nu}\right)^2, \quad (7.16)$$

with,

$$\frac{\nu'}{\nu} = \frac{1-\beta\cos\alpha}{1-\beta\cos\alpha' + \frac{h\nu}{\gamma m_e c^2}(1-\cos\Theta)}. \quad (7.17)$$

In these equations  $\sigma_T$  is the Thomson cross-section and  $m_e$  is the electron rest mass.  $\alpha$  and  $\alpha'$  are the angles between the incident electron and the incident and outgoing photon,  $\Theta$  is the angle between the incident and outgoing photons (the scattering angle from previous chapters) and  $\nu$  and  $\nu'$  are the incident and scattered photon frequencies. In what follows the Thomson limit of Compton scattering is assumed to hold ( $h\nu \ll \gamma m_0 c^2$ ), so that the third term in the denominator of Eq. 7.17 may be ignored.

The quantity  $X$  which specifies the initial and final polarisation states of the photon is defined in terms of four-vector products (and is therefore a Lorentz invariant) thus,

$$X = \frac{1}{2} \left( \frac{\kappa}{\kappa'} + \frac{\kappa'}{\kappa} \right) - 1 + 2 \left( \mathbf{e} \cdot \mathbf{e}' + \frac{\mathbf{e} \cdot \mathbf{p} \mathbf{e}' \cdot \mathbf{p}'}{\kappa} - \frac{\mathbf{e} \cdot \mathbf{p}' \mathbf{e}' \cdot \mathbf{p}}{\kappa'} \right)^2. \quad (7.18)$$

The Lorentz invariant scalars  $\kappa$  and  $\kappa'$  are,

$$\kappa = -p \cdot k, \quad \kappa' = -p \cdot k', \quad (7.19)$$

where  $p$  and  $p'$ ,  $k$  and  $k'$  are the initial and final four-momenta of the electron and photon and  $e$  and  $e'$  are the initial and final photon polarisation four-vectors. The scalars  $\kappa$  and  $\kappa'$  are,

$$\kappa = -h\nu\gamma m_e(1 - \beta \cos \alpha), \quad \kappa' = -h\nu'\gamma m_e(1 - \beta \cos \alpha'). \quad (7.20)$$

In the Thomson limit defined above the ratio of these quantities is  $\kappa/\kappa' = 1$ , which considerably simplifies the calculations below. When the polarisation state of the scattered photon is not observed  $X$  should be replaced by  $\bar{X}$  which is the average of the initial and sum over the final polarisation directions.

$X$  has now to be calculated for scattering from each initial polarisation state into some final state. The  $X$  for any particular final polarisation state is the average over the  $X$ 's for the scattering of all initial states into that particular one. Attention is now focussed on the simplest and most relevant case in the context of astrophysical jets, where the incident photons are unpolarised and incident on the electron from behind, Fig. 7.1.

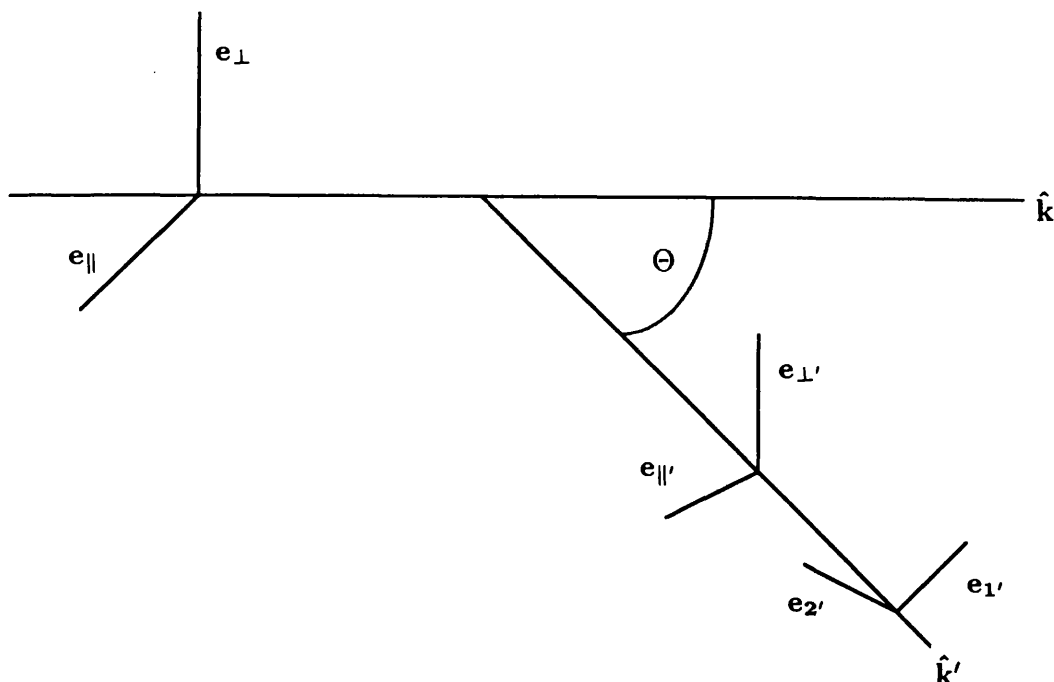


Fig. 7.1 Unpolarised radiation scattered from direction  $\hat{k}$  to  $\hat{k}'$ . The spatial components of the incident and scattered polarisation four-vectors are also shown

#### 7.4 Unpolarised point source illuminating a rectilinear jet

Incident unpolarised radiation may be represented by the combination of the polarisation four-vectors  $e_{\perp}$  and  $e_{\parallel}$  whose spatial components are shown in Fig. 7.1. Since the polarisation vectors are transverse to the direction of propagation the transverse gauge has been chosen such that

$e_0 = e_4 = 0$ . Four scattered polarisation vectors are also shown  $e_{\perp'}$ ,  $e_{\parallel'}$ ,  $e_1'$  and  $e_2'$ . Calculation of the  $X$ 's for these final states will yield the total cross-section along with the cross-sections for the Stokes  $Q$  and  $U$  parameters of the scattered radiation which are defined as,

$$\begin{pmatrix} \frac{d\sigma_I}{d\Omega} \\ \frac{d\sigma_Q}{d\Omega} \\ \frac{d\sigma_U}{d\Omega} \end{pmatrix} = \begin{pmatrix} \frac{d\sigma_{\perp'}}{d\Omega} + \frac{d\sigma_{\parallel'}}{d\Omega} \\ \frac{d\sigma_{\perp'}}{d\Omega} - \frac{d\sigma_{\parallel'}}{d\Omega} \\ \frac{d\sigma_{1'}}{d\Omega} - \frac{d\sigma_{2'}}{d\Omega} \end{pmatrix} = \frac{3\sigma_T}{16\pi\gamma^2(1-\beta\cos\alpha)^2} \begin{pmatrix} X_{\perp'} + X_{\parallel'} \\ X_{\perp'} - X_{\parallel'} \\ X_{1'} - X_{2'} \end{pmatrix}, \quad (7.21)$$

where the  $X$ 's are,

$$\begin{pmatrix} X_{\perp'} \\ X_{\parallel'} \\ X_{1'} \\ X_{2'} \end{pmatrix} = \frac{1}{2} \begin{pmatrix} X_{\perp\perp'} + X_{\parallel\perp'} \\ X_{\perp\parallel'} + X_{\parallel\parallel'} \\ X_{\perp 1'} + X_{\parallel 1'} \\ X_{\perp 2'} + X_{\parallel 2'} \end{pmatrix}. \quad (7.22)$$

For the case depicted in Fig. 7.1 the four-momenta of the incident electron,  $p$ , and the incident,  $k$ , and scattered,  $k'$ , photons are,

$$p = \gamma m_0 c (1, 0, 0, \beta), \quad k = \frac{h\nu}{c} (1, 0, 0, 1), \quad k' = \frac{h\nu'}{c} (1, 0, \sin\Theta, \cos\Theta). \quad (7.23)$$

The polarisation four-vectors depicting the incident unpolarised photon are,

$$e_{\perp} = (0, 1, 0, 0), \quad e_{\parallel} = (0, 0, 1, 0), \quad (7.24)$$

while the scattered polarisation four-vectors are,

$$\begin{aligned} e_{\perp'} &= (0, 1, 0, 0), & e_{\parallel'} &= (0, 0, \cos\Theta, -\sin\Theta), \\ e_{1'} &= \frac{1}{\sqrt{2}} (0, 1, -\cos\Theta, \sin\Theta), & e_{2'} &= \frac{1}{\sqrt{2}} (0, 1, \cos\Theta, -\sin\Theta). \end{aligned} \quad (7.25)$$

Using the above in Eq. 7.18 leads to the following results,

$$X_{\perp\perp'} = 2, \quad X_{\parallel\perp'} = 0, \quad X_{\perp\parallel'} = 0, \quad X_{\parallel\parallel'} = 2 \left( \frac{\cos\Theta - \beta}{1 - \beta\cos\Theta} \right)^2, \quad (7.26)$$

$$X_{\perp 1'} = 1, \quad X_{\parallel 1'} = \left( \frac{\cos\Theta - \beta}{1 - \beta\cos\Theta} \right)^2, \quad X_{\perp 2'} = 1, \quad X_{\parallel 2'} = \left( \frac{\cos\Theta - \beta}{1 - \beta\cos\Theta} \right)^2, \quad (7.27)$$

thus giving,

$$\begin{pmatrix} \frac{d\sigma_I}{d\Omega} \\ \frac{d\sigma_Q}{d\Omega} \\ \frac{d\sigma_U}{d\Omega} \end{pmatrix} = \frac{3\sigma_T}{16\pi\gamma^2(1-\beta\cos\alpha)^2} \begin{pmatrix} 1 + \left( \frac{\cos\Theta - \beta}{1 - \beta\cos\Theta} \right)^2 \\ 1 - \left( \frac{\cos\Theta - \beta}{1 - \beta\cos\Theta} \right)^2 \\ 0 \end{pmatrix}. \quad (7.28)$$

The degree of linear polarisation of the scattered photon in this case is simply,

$$P = \frac{1 - \left( \frac{\cos\Theta - \beta}{1 - \beta\cos\Theta} \right)^2}{1 + \left( \frac{\cos\Theta - \beta}{1 - \beta\cos\Theta} \right)^2}, \quad (7.29)$$

while, from Eq. 7.17, the relative frequency shift is,

$$\frac{\nu'}{\nu} = \frac{1 - \beta}{1 - \beta \cos \Theta} \quad (7.30)$$

The polarisation and relative frequency shift of the scattered radiation are plotted, for various  $\beta$  values, as a function of scattering angle in Figs. 7.2 and 7.3. The simplest model of a relativistic jet is that of a point source (e.g. a quasar) and a rectilinear stream of particles ( $e^\pm$  pairs). Clearly this can be modelled by extending the above formalism from one scattering electron to a line of electrons moving at the same speed,  $\beta c$ . With this set-up the scattering angle is just the angle which the "jet" makes to the line of sight and inspection of Eq. 7.29 shows that the polarisation maximises at  $\cos \Theta = \beta$ , which is the so-called superluminal direction for relativistic jets (Rees, 1966). However, unlike superluminal motion, which has a simple geometrical explanation, the peaking of the polarisation of scattered radiation in this direction is a relativistic aberrational effect arising from the electron's motion with respect to the observer. Equation 7.29 may also be written in the form,

$$P = \frac{1 - \cos^2 \Theta'}{1 + \cos^2 \Theta'} \quad (7.31)$$

where  $\Theta'$  is the angle of aberration.

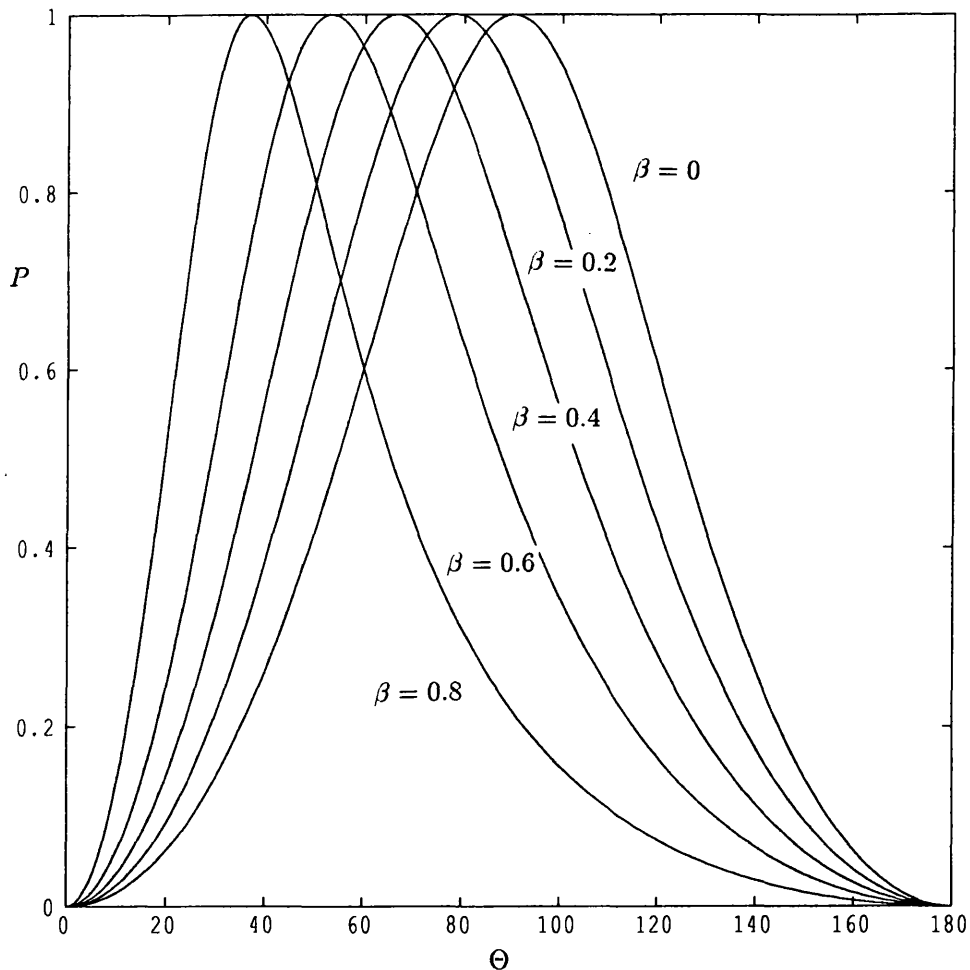


**Fig. 7.2** Degree of polarisation against scattering angle for various  $\beta$  values for the scattering geometry of Fig. 7.1.

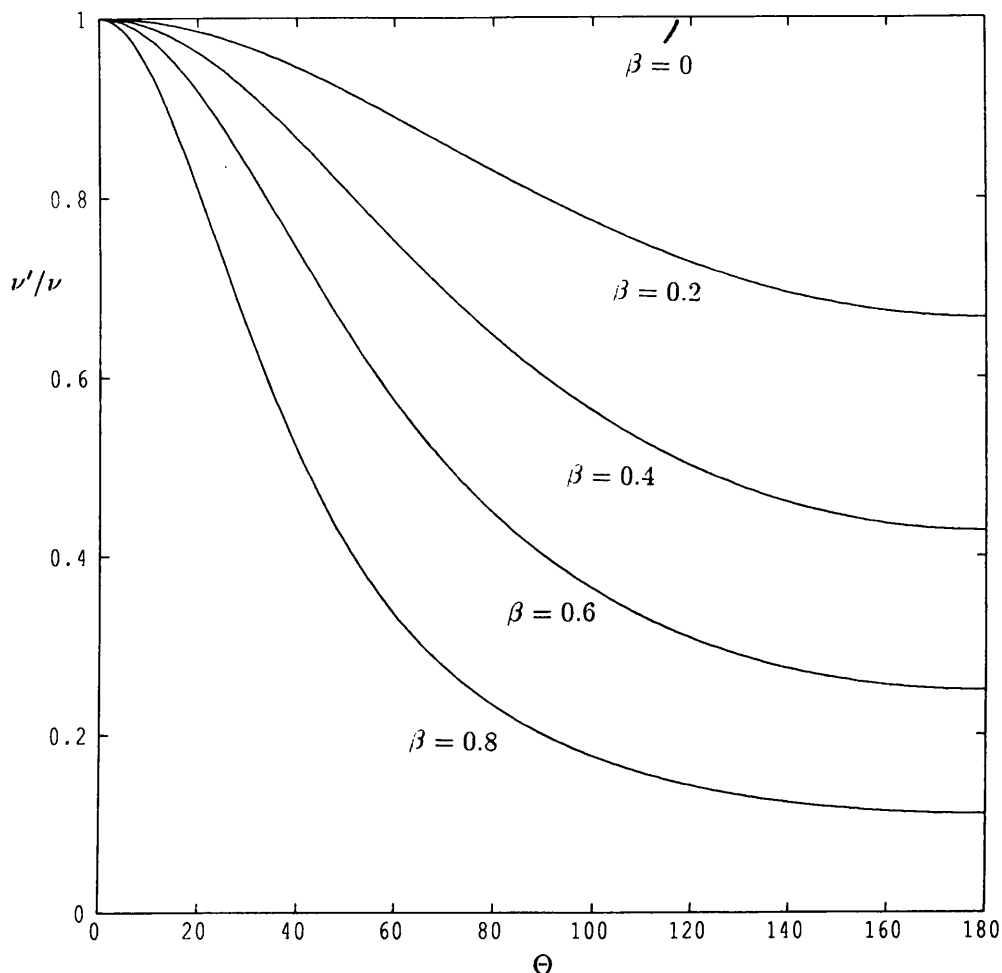


**Fig. 7.3** Ratio of scattered to incident photon frequency as a function of scattering angle for various  $\beta$  values for the scattering geometry of Fig. 7.1

#### 7.4 Application to relativistic jets

The above analysis can clearly be applied to the scattering of unpolarised radiation from a central source in an optically thin, narrow jet. In this case the frequency shift of the scattered radiation must also be considered (Eq. 7.17, Fig. 7.3). For high electron speeds and large scattering angles the scattered radiation will appear highly shifted to the red. The combination of the tiny scattering cross-section and the steep spectrum synchrotron radiation, frequently observed from such jets, will result in the scattered flux going largely undetected above the much stronger continuum present at the scattered frequency. All is not lost though, since for sources to be superluminal requires very high jet speeds and small angles to the line of sight (e.g. Cohen & Unwin, 1984), thus reducing the frequency shift of scattered radiation (i.e. superluminal sources will occur in the top left corner of Fig. 7.3).

A strong line from the source which is scattered in such a jet will appear (reduced by the appropriate scattering optical depth) at the relevant frequency in the intensity spectrum of the jet and will be highly polarised. Thus another feature of superluminal sources is that spectral features

of the central source will appear (highly polarised) in the jet's spectrum.

Analysis of such scattered features – their polarisation and frequency shift – allows the jet viewing angle and speed to be determined by solving Eqs. 7.29 and 7.30 for the unknowns  $\Theta$  and  $\beta$ . Clearly this is a very simple model of a jet and in more realistic situations account must be made of synchrotron radiation from the jet itself which may be highly polarised. The theoretical framework presented in Sect. 7.3 may be applied to scattering of polarised synchrotron photons within the jet – the synchrotron–self–Compton effect. Preliminary estimations of the levels of polarisation to be expected from this effect (Blandford & Rees, 1978) predicted that the polarisation of synchrotron–self–Compton photons would be reduced by  $\sim 50\%$  from their initial polarisation value. This effect must be analysed thoroughly with the above relativistic treatment to determine accurately the levels of polarisation to be expected from such jets in which synchrotron radiation and Compton/Thomson scattering both play a major role. However, the simple analytic treatment presented above demonstrates the diagnostic potential of jet polarisation in determining speeds and orientations – again information which is not available from spectrometry alone.

## References

- Almalki M., 1992, *Ph.D. Thesis*, University of Glasgow
- Axon D.J., 1993, private communication
- Anderson C.M., 1993, private communication
- Bjorkman K.S., Nordsieck K.H., Code A.D., Anderson C.M., Babler B.L., Clayton G.C., Maghales A.M., Meade M.R., Nook M.A., Schulte-Ladbeck R.E., Taylor M., Whitney B.A., 1991, *Astrophys. J.*, **383**, L67
- Bjorkman J.E., 1993, private communication
- Blandford R.D., Rees M.J., 1978, *Pittsburgh conference on BL Lac objects*, ed. A.M. Wolfe
- Brown J.C., McLean I.S., 1977, *Astron. Astrophys.*, **57**, 141
- Brown J.C., Henrichs H.F., 1987, *Astron. Astrophys.*, **57**, 141
- Brown J.P., Carlaw V.A., Cassinelli J.P., 1989, *Astrophys. J.*, **344**, 341
- Brown J.C., Fox G.K., 1989 *Astrophys. J.*, **347**, 468
- Cassinelli J.P., Haisch B.M., 1974, *Astrophys. J.*, **188**, 101
- Cassinelli J.P., Nordsieck K.H., Murison M.A., 1987, *Astrophys. J.*, **315**, 290
- Castor J.I., Abbott D.C., Klein R.I., 1975, *Astrophys. J.*, **195**, 157
- Chandrasekhar S., 1960, *Radiative Transfer*, Dover
- Clarke D., McLean I.S., 1973, *Planets stars and nebulae studied with photopolarimetry*, ed. T. Gehrels
- Clayton G.C., Anderson C.M., Maghales A.M., Code A.D., Nordsieck K.H., Meade M.R., Wolff M.J., Babler B.L., Bjorkman K.S., Schulte-Ladbeck R.E., Taylor M., Whitney B.A., 1992, *Astrophys. J.*, **385**, L53
- Cohen M.H., Unwin S.C., 1984, *VLBI and compact radio sources*, IAU Symp. 110
- Collins G.W., 1970, *Astrophys. J.*, **159**, 583
- Collins G.W., Cranmer S.R., 1992, *Mon. Not. Roy. Ast. Soc.*, **253**, 167
- Coyne G.V., 1976, *Be and shell stars*, IAU Symp 70
- Craig I.J.D., Brown J.C., 1984, *Inverse Problems in Astronomy*, Adam Hilger
- De Young D.S., 1966, *J. of Math. Phys.*, **7**, 1916
- Daniel J.Y., 1980, *Astron. Astrophys.*, **86**, 198
- Dirac P.A.M., 1925, *Mon. Not. Roy. Ast. Soc.*, **85**, 825
- Dolan J.F., 1984, *Astron. Astrophys.*, **138**, 1
- Fletcher L., 1993, *Ph.D. Thesis*, University of Glasgow
- Fox G.K., Brown J.C., 1991, *Astrophys. J.*, **375**, 300
- Fox G.K., 1991, *Astrophys. J.*, **379**, 663
- Griem H.R., 1960, *Astrophys. J.*, **132**, 883
- Hamilton D.R., 1947, *Astrophys. J.*, **106**, 457
- Hanuschik R., 1993, *Kinematics and dynamics of diffuse astrophysical media*, Kluwer

- Haisch B.M., Cassinelli J.P., 1976, *Astrophys. J.*, **208**, 253
- Hayes D.P., Guinan E.F., 1984, *Astrophys. J.*, **279**, 721
- Hénoux et al, 1990, *Astrophys. J. Suppl.*, **73**, 203
- Jackson J.D., 1962, *Classical Electrodynamics*, John Wiley & Sons
- Jauch J.M., Rohrlich F., 1976, *The theory of photons and electrons*, Springer Verlag
- Jeffrey D.J., 1989, *Astrophys. J. Suppl.*, **71**, 951
- Lefevre J., 1992, *Astron. Astrophys.*, **264**, 274
- Matheson D.S., Ford V.L., 1970, *Mem. Roy. Ast. Soc.*, **74**, 139
- McLean I.S., 1979 *Mon. Not. Roy. Ast. Soc.*, **186**, 265
- McLean I.S., Coyne G.C., Frecker J.E., Serkowski K., 1979, *Astrophys. J.*, **228**, 802
- Mihalas D.M., 1978, *Stellar Atmospheres*, Freeman
- Moffat A.F.J., Drissen L., Robert C., Lamontagne R., Coziol R., Mousseau N., Niemela V.S., Cerruti M.A., Seggewiss W., Van Weeren N., 1990, *Astrophys. J.*, **350**, 767
- Munch G., 1947, *Astrophys. J.*, **108**, 116
- Ohman Y., 1934, *Nature*, **134**, 534
- Ohman Y., 1946, *Astrophys. J.*, **104**, 460
- Papaloizou J.C., Savonije G.J., Henrichs H.F., *Astron. Astrophys.*, **265**, L45
- Poeckert R., 1975, *Astrophys. J.*, **196**, 777
- Poeckert R., Marlborough J.M., 1978, *Astrophys. J.*, **220**, 940
- Rees M.J., 1966, *Nature*, **211**, 468
- Romanik C.J., Leung C.M., 1981, *Astrophys. J.*, **246**, 935
- Rudy R.J., Kemp J.C., 1978, *Astrophys. J.*, **221**, 200
- Rybicki G.B., Lightman A.P., 1979, *Radiative Processes in Astrophysics*, John Wiley & Sons
- Schulte-Ladbeck R.E., Meade M.R., Hillier J.D., 1991, *Nonisotropic and variable outflows from stars*, ed. L. Drissen
- Sen K.K., Lee W.M., 1960 *P.A.S.J.*, **13**, 263
- Serkowski, K., 1973, *Planets stars and nebulae studied with photopolarimetry*, ed. T. Gehrels
- Shepherd D., 1993, private communication
- Sneddon I.N., 1972, *The Use of Integral Transforms*, McGraw-Hill
- Sonneborn G., Grady C.A., Wu Ch.-Ch., Hayes D.P., Guinan E.F., Barker P.K., Henrichs H.F., 1988, *Astrophys. J.*, **325**, 784
- Stokes G.G., 1852, *Trans. Camb. Philos. Soc.*, **9**, 399
- Thompson A.M., Kay J.W., Titterton D.M., *J. Statist. Comput. Simul.*, **33**, 199
- Van Blerkom J., Van Blerkom D., 1978, *Astrophys. J.*, **226**, 482
- Van de Hulst H.C., 1950, *Light Scattering off Small Particles*, Dover
- Whitney B.A., Code A.D., 1989, *B.A.A.S.*, **21**, 1114
- Whittet D.C.B., Martin P.G., Hough J.H., Rouse M.F., Bailey J.A., Axon D.J., 1991, preprint

## Appendix A

This appendix is included to define various terms and concepts which are used throughout the thesis. The definitions presented below have been collated from books on the subject of radiative transfer by Chandrasekhar and Mihalas.

### A.1 The specific intensity

As was stated in Section 1.1 the *specific intensity* completely specifies a radiation field except for its polarisation state. The specific intensity,  $I_\nu$ , is defined by the amount of radiative energy  $dE_\nu$  in a specified frequency interval (from  $\nu$  to  $\nu + d\nu$ ) which is transported across an element of area  $dA$  into solid angle  $d\Omega$  in a time  $dt$  according to,

$$dE_\nu = I_\nu dA \cos \theta d\nu d\Omega dt, \quad (\text{A.1})$$

where  $\theta$  is the angle between the direction of the incident beam of radiation and the normal to the surface  $dA$ .

### A.2 The flux

The *flux* is a quantity which defines the rate of radiant energy flow into all directions across a surface per unit area per unit frequency interval and is given by,

$$F_\nu = \int I_\nu \cos \theta d\Omega, \quad (\text{A.2})$$

where the integration is over all solid angles.

### A.3 Opacity – absorption and scattering coefficients

When a beam of radiation traverses a medium its specific intensity will be altered due to interaction of the radiation with matter. The *opacity* is a measure of the extent to which a material absorbs and scatters incident radiation. If the specific intensity,  $I_\nu$ , becomes  $I_\nu + dI_\nu$  after traversing a thickness  $ds$  in a medium of density  $\rho$  then the *mass absorption coefficient* or *opacity* of the material,  $\kappa_\nu$ , is defined by,

$$dI_\nu = -\kappa_\nu \rho I_\nu ds, \quad (\text{A.3})$$

This change in energy may not be entirely lost by the radiation field since it may reappear in other directions as *scattered* radiation. In general only part of this radiant energy will be scattered and the rest will have been transformed into other forms of energy (or even radiation of other frequencies) – i.e. this part of the radiant energy has been truly *absorbed*. It is therefore necessary to distinguish between *true absorption* and *scattering*.

When the medium contains many different species (absorbing or scattering particles) the total opacity is just the sum of the individual opacities, viz,

$$\kappa_\nu = \sum_i \kappa_\nu^i . \quad (\text{A.4})$$

In the case of scattering a material is characterised by a *mass scattering coefficient*,  $\kappa_\nu$ , if when a beam of radiation is incident on an element of mass of cross-sectional area  $dA$  and thickness  $ds$  the amount of energy scattered from it in a time  $dt$  in all directions is,

$$dE_\nu = \kappa_\nu \rho ds I_\nu dA \cos \theta d\nu d\Omega dt . \quad (\text{A.5})$$

Since the mass of the element is  $dm = \rho \cos \theta dA ds$  this may also be written as,

$$dE_\nu = \kappa_\nu I_\nu dm d\nu d\Omega dt . \quad (\text{A.6})$$

To give a full account of scattering the angular redistribution of the scattered radiation must also be described. This is achieved through the *angular phase function*,  $g(\hat{\mathbf{k}}, \hat{\mathbf{k}}')$ , such that,

$$\kappa_\nu I_\nu dm d\nu d\Omega dt g(\hat{\mathbf{k}}, \hat{\mathbf{k}}') \frac{d\Omega'}{4\pi} , \quad (\text{A.7})$$

is the amount of radiant energy scattered from an element of solid angle  $d\Omega$  about direction  $\hat{\mathbf{k}}$  into an element of solid angle  $d\Omega'$  around direction  $\hat{\mathbf{k}}'$  by an element of mass  $dm$  in time  $dt$ . The total energy lost from the incident beam due to scattering in all directions is then

$$\kappa_\nu I_\nu dm d\nu d\Omega dt \int g(\hat{\mathbf{k}}, \hat{\mathbf{k}}') \frac{d\Omega'}{4\pi} . \quad (\text{A.8})$$

When the phase function is *normalised to unity* thus,

$$\int g(\hat{\mathbf{k}}, \hat{\mathbf{k}}') \frac{d\Omega'}{4\pi} = 1 , \quad (\text{A.9})$$

then the above analysis represents the case of *perfect scattering* where all the incident radiant energy reappears as scattered energy at the same frequency. When the integral over the angular phase function in Eq. A.9 is not unity but is equal to a number,  $\omega$  say, which is less than one then the fraction  $\omega$  represents the fraction of the incident radiant energy which is scattered while  $(1 - \omega)$  is that fraction which has been transformed into other forms of energy (or radiation of other frequencies).

When there are both frequency and angular redistributions of the scattered radiation these two effects may be incorporated into a total redistribution function,  $R(\nu, \hat{\mathbf{k}}; \nu', \hat{\mathbf{k}}')$ , such that,

$$\kappa_\nu I_\nu dm d\nu d\Omega dt R(\nu, \hat{\mathbf{k}}; \nu', \hat{\mathbf{k}}') \frac{d\Omega'}{4\pi} d\nu' , \quad (\text{A.10})$$

represents the energy incident at frequency  $\nu$  from solid angle  $d\Omega$  around direction  $\hat{\mathbf{k}}$  which is scattered into solid angle  $d\Omega'$  around direction  $\hat{\mathbf{k}}'$  with frequency  $\nu'$ . In this case the analogous equation to A.9 is

$$\frac{1}{4\pi} \int \int R(\nu, \hat{\mathbf{k}}; \nu', \hat{\mathbf{k}}') d\nu d\Omega' = 1, \quad (\text{A.11})$$

with the physical interpretation that incident radiant energy of frequency  $\nu'$  is scattered in all directions to some frequency  $\nu$  and there is no transformation of radiant energy into other energy forms.

Another way of expressing the scattered energy is in terms of the scattering coefficient *per particle*, often referred to as the scattering cross section  $\sigma_\nu$ . This is defined such that the radiant energy scattered per particle is,

$$\sigma_\nu I_\nu d\nu d\Omega dt R(\nu, \hat{\mathbf{k}}; \nu', \hat{\mathbf{k}}') \frac{d\Omega'}{4\pi} d\nu'. \quad (\text{A.12})$$

From an element of mass  $dm$  the amount of scattered radiant energy will then be given by Eq. A.12 multiplied by  $N dm$  where  $N$  is the number of scatterers per unit mass. Comparing this with Eq. A.10  $\kappa_\nu$  may be expressed as,

$$\kappa_\nu = N \sigma_\nu = \frac{n \sigma_\nu}{\rho}, \quad (\text{A.13})$$

where  $n$  is the number of scattering particles per unit volume (number density) and  $\rho$  is the mass density of the scattering volume.

#### A.4 Optical depth

As a photon traverses a medium it will travel a certain distance before being absorbed or scattered and the average distance it travels prior to such an "event" is called its *mean free path*. This average quantity,  $l_\nu$ , may be defined in terms of the density and opacity of the medium thus,

$$l_\nu = \rho \kappa_\nu = n \sigma_\nu. \quad (\text{A.14})$$

The *optical depth*,  $\tau_\nu$ , between two points in a medium is the number of photon mean free paths between the two points thus,

$$\tau_\nu = \int_a^b \rho \kappa_\nu ds = \int_a^b n \sigma_\nu ds. \quad (\text{A.15})$$

Whether a medium is optically thick or thin depends on the value of  $\tau_\nu$  and a standard rule of thumb is that a medium is considered to be optically thin for  $\tau_\nu$  less than unity. In this thesis an optically thin electron scattering atmosphere is taken to be one in which the results of a "single scattering" analysis deviate little from those of a full blown radiative transfer or Monte Carlo analysis.

### A.5 The emission coefficient

The *emission coefficient*,  $j_{\nu'}$ , is defined in such a way that an element of mass  $dm$  emits into a solid angle  $d\Omega'$  in the frequency range  $\nu'$  to  $\nu' + d\nu'$  in the time  $dt$  the amount of radiant energy given by,

$$j_{\nu'} dm d\Omega' d\nu' dt . \quad (\text{A.16})$$

In a medium which scatters radiation there will be a contribution to the emission coefficient due to radiation being scattered from all directions,  $\hat{\mathbf{k}}$ , and all frequencies,  $\nu$ , into the solid angle  $d\Omega'$  around  $\hat{\mathbf{k}}'$  with frequency  $\nu'$ . Thus from Eq. A.10 the contribution to the emission coefficient due to scattering alone is,

$$j_{\nu'}^s(\hat{\mathbf{k}}') = \frac{1}{4\pi} \int \int \kappa_{\nu} I_{\nu}(\hat{\mathbf{k}}) R(\hat{\mathbf{k}}', \nu'; \hat{\mathbf{k}}, \nu) d\Omega d\nu , \quad (\text{A.17})$$

### A.6 The equation of radiative transfer

In a medium characterised by a mass absorption coefficient  $\kappa_{\nu}$  and an emission coefficient  $j_{\nu}$  the difference in radiant energy crossing normally two faces of area  $dA$  separated by  $ds$  in a time  $dt$  is given by (cf Eq. A.1),

$$\frac{dI_{\nu}}{ds} ds dA d\nu d\Omega dt . \quad (\text{A.18})$$

This difference arises due to differences between the amounts of emission and absorption in the frequency interval and solid angle concerned. The amount absorbed, by Eq. A.5, is

$$\kappa_{\nu} \rho ds I_{\nu} dA d\nu d\Omega dt . \quad (\text{A.19})$$

while the amount emitted is,

$$j_{\nu} \rho ds dA d\nu d\Omega dt . \quad (\text{A.20})$$

Therefore the difference in A.18 is equal to the energy emitted (A.20) minus the energy absorbed (A.19), thus yielding the equation of radiative transfer,

$$\frac{dI_{\nu}}{ds} = \rho j_{\nu} - \rho \kappa_{\nu} I_{\nu} , \quad (\text{A.21})$$

The equation of radiative transfer presented above describes the transfer and interaction of the *total intensity* of radiation within a medium. As was illustrated in Chapter 1 any radiation field can be split into intensity components (the Stokes parameters) and it is therefore possible to write an equation of transfer for each intensity component of the radiation field analogous to Eq. A.21. In a scattering/absorbing atmosphere such an equation will require a redistribution function for each Stokes parameter and a convenient way of writing this is in vector/matrix notation, viz,

$$\frac{d\mathbf{I}_{\nu}}{ds} = \rho \mathbf{j}_{\nu} - \rho \kappa_{\nu} \mathbf{I}_{\nu} , \quad (\text{A.22})$$

where  $\mathbf{I}_\nu$  is a vector whose four components are the un-normalised Stokes parameters. The vector emission coefficient due to scattering is,

$$\mathbf{j}_\nu = \frac{1}{4\pi} \int_{\nu_*} \int_{\Omega_*} \kappa_{\nu'} \mathbf{R}(\nu', \hat{\mathbf{k}}'; \nu, \hat{\mathbf{k}}) \mathbf{I}_{\nu'} d\Omega' d\nu'. \quad (\text{A.23})$$

The optically thin single (Thomson) scattering analysis presented in this thesis neglects absorption within the circumstellar envelope and attributes *all* envelope emission to scattering. These assumptions reduce the Stokes vector equation of transfer to,

$$\frac{d\mathbf{I}_\nu}{ds} = \rho \mathbf{j}_\nu. \quad (\text{A.24})$$

